An Investigation into Stent Expansion using Numerical and Experimental Techniques

by

Deborah Toner, BEng

A thesis submitted to Dublin City University in partial fulfilment of the requirement for the degree of

Masters in Engineering

Supervisor
Dr. Caitriona Lally, BEng, MEng, PhD

School of Mechanical and Manufacturing Engineering
Dublin City University

September 2009

DECLARATION

I hereby certify that this material, which I now submit for assessment on the programme of study leading to the award of Masters in Engineering is entirely my own work, that I have exercised reasonable care to ensure that the work is original, and does not to the best of my knowledge breach any law of copyright, and has not been taken from the work of others save and to the extent that such work has been cited and acknowledged within the text of my work.

Signed: ---------- ID No: 52747685

Deborah Mary Toner

Date: 23rd September 2009

ACKNOWLEDGEMENTS

I would like to thank first and foremost, my supervisor, Dr. Caitríona Lally, for her endless support, encouragement and guidance throughout this research study. I could not have asked for a better mentor. Amongst many things, I am extremely grateful for the opportunities provided to me to present at well established conferences throughout my postgraduate days.

I would also like to thank John and my parents for all the love, support and understanding that they have shown throughout my journey. John, your patience knows no end, I am eternally grateful. Thank you also to my four amazing sisters for their sincere encouragement and constant supply of wise words.

To my two Italian friends, Vittoria and Alberto, 'mille grazie' for all the kind words of encouragement, all the laughs, and all the good times we shared together throughout our postgraduate years. No office will be the same without you.

Many thanks to Finbar Dolan in Medtronic for the supply of Driver stents, without which this research study would not have been possible.

Extended thanks to Liam Domican and Cian Merne who provided me with endless technical support and made possible the manufacture of my *in-vitro* rig.

Thanks also to Keith Hickey for looking after all my IT needs, which were too many to mention.

An investigation into stent expansion using numerical and experimental techniques

Deborah Toner

Abstract

Extensive finite element analyses have been carried out by researchers to investigate the difference in the mechanical loading induced in vessels stented with various different stent designs and the influence of this loading on restenosis outcome. This study investigates the experimental validation of these numerical stent expansions using compliant mock arteries. The development of this *in-vitro* validation test has the prospect of providing a fully validated preclinical testing tool which can be used to optimise stent designs.

Mock arteries were developed as straight cylindrical vessels using a specially designed rig such that they had an inner lumen diameter of 3 mm and a thickness of 0.5 mm, thus representing a typical porcine coronary artery geometry. These mock arteries were manufactured from compliant Sylgard® elastomer 184 (Dow Corning). This material was chosen mainly due to its inherent variable elastic properties which are determined by its curing process and ratio of elastomer to curing agent. Extensive testing was carried out on samples of porcine coronary arteries and differing ratios of Sylgard® to identify a close match in mechanical properties to those of porcine coronary arteries. Driver stents (Medtronic AVE) were expanded both freely and inside these mock arteries and the subsequent deformation recorded using a video extensometer.

The Driver stent was numerically modelled with a strut thickness of 0.09 mm and an overall length of 9 mm such that each modular element had a length of 1 mm. The material for the stent was described using an elasto-plastic material model whereby the linear elasticity was defined using values for MP35N cobalt chromium alloy: Young's Modulus of 232 GPa, Poisson's Ratio of 0.26. A piecewise linear function was used to represent the non-linear plasticity of the material through a von Mises plasticity model with isotropic hardening. Due to symmetry, only one-quarter of the geometry was modelled in the circumferential direction. The mock artery was represented as a hyperelastic material, the constitutive equation determined by fitting to the uniaxial tension tests of Sylgard® elastomeric material. A uniform pressure was applied to the internal surface of each stent to represent a balloon expansion.

This study identified a suitable material for use as a blood vessel substitute such that experimental stent expansions could be carried out within the mock artery and the results used to evaluate the accuracy of the numerical methods. Finite element analyses were carried out to examine two separate methods for stent expansion such that the most accurate and effective method could be determined. Results show that the numerical methods used in simulating the free expansion, and expansion inside a mock artery of the Driver stent, can accurately describe the *in-vitro* stent expansion. Both experimental and numerical models were found to achieve similar amounts of foreshortening, longitudinal recoil and radial recoil.

TABLE OF CONTENTS

NOMENCLATURE

Roman Letters

a_{ij}	Material constants
E	Green-Lagrangian strain tensor
L	Length
R	Radius
S	Component of the second Piola-Kirchoff stress tensor
W	Strain energy

Greek Letters

I_1, I_2, I_3	Stretch invariants
λ_1, λ_2, λ_3	Principal stretches
σ	von Mises stress
σ_1, σ_2, σ_3	Principal stresses
$\dot{\varepsilon}^{pl}$	Plastic strain rate tensor
$\dot{\varepsilon}_{eqv}$	Equivalent plastic strain

LIST OF FIGURES

LIST OF TABLES

CHAPTER 1

INTRODUCTION

1.1 Cardiovascular Disease

Cardiovascular disease (CVD) covers a wide range of diseases affecting the heart and the blood vessels, including coronary artery disease, cerebrovascular disease, congenital heart disease, heart attack, heart failure, high blood pressure and stroke. Cardiovascular disease is the single largest killer worldwide and also in the United States, with an average of 1 American death due to CVD every 37 seconds [1]. According to the World Health Organisation (WHO), an estimated 17.5 million people died from cardiovascular disease in 2005, representing a staggering 30% of all global deaths, see Figure 1.1 [2]. The World Health Organisation also predicts that this will rise to 20 million people by 2010 if the current trend continues [2].

Not only is cardiovascular disease a major killer in today's society, but it also places a huge economic burden on both developed and developing countries, with cardiovascular disease costing the European Union €169 billion in 2003 [3]. The estimated direct and indirect cost of CVD in the United States for 2008 is $448.5 billion which is approximately €354 billion [1]. As the population ages, the economic impact of CVD on the US health care system continues to grow.

Ireland is also subject to this leading killer, with approximately 10,000 Irish people dying each year from some form of cardiovascular disease. This accounts for 36% of all deaths, thus establishing cardiovascular disease as the most common cause of death [4]. Coronary heart disease (CHD) accounts for approximately half of these deaths with one quarter due to stroke.

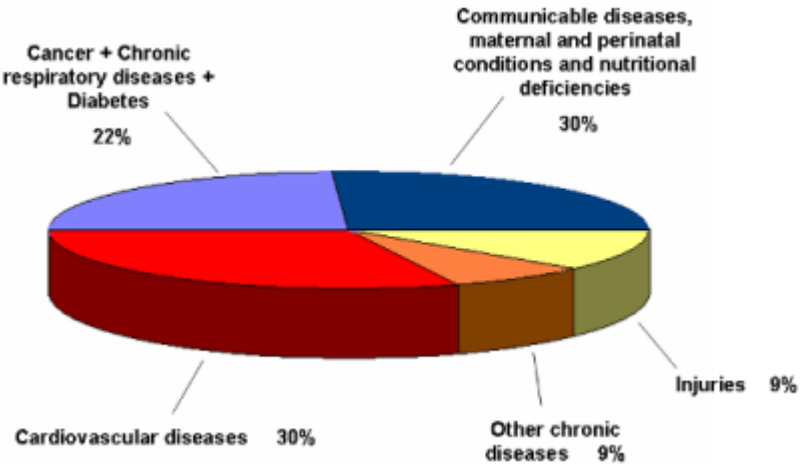

Figure 1.1: Chart illustrating cardiovascular diseases as representing 30% of all global deaths (adapted from WHO) [2]

A number of both diagnostic and therapeutic procedures are available today which can be used to detect and treat cardiovascular diseases. Over the past number of years, the development of improved diagnostic equipment has enabled the early diagnosis of CVD and more successful interventional procedures. Extensive research being carried out in this area has led to a better understanding of the effect of mechanical intervention on the biological function of arteries, thus improving patient care and the treatment of CVD.

Coronary angiography, in particular, is performed to enable the visualization of the coronary arteries such that the location and severity of the blockage can be determined. CVD can be treated using medical treatments, surgical treatments or interventional cardiology. Medical treatment can range from the consumption of a diet low in saturated fats and cholesterol, to the administration of pharmacological agents. Surgical procedures, such as coronary artery bypass grafting (CABG) are performed to surgically restore blood flow to the heart. Surgical procedures however, have many associated complications and risks and lead to longer hospital stays when compared to nonsurgical revascularization techniques. Many nonsurgical treatments are available for CVD, such as percutaneous transluminal angioplasty, laser revascularization techniques, and stenting procedures, all of which lead to the restoration of blood flow to the heart.

1.2 Coronary Heart Disease

Coronary heart disease (CHD) and stroke are the two main contributing diseases to cardiovascular disease and are caused by blockages in the arteries which prevent blood from flowing to the heart or brain. Coronary heart disease contributes to almost half of all CVD deaths while stroke contributes to almost one third. In CHD the coronary arteries become narrowed making it difficult for blood to flow to the heart and in some cases leading to myocardial infarction. This narrowing of the arteries is caused by atherosclerosis, coronary artery spasm, or a clot in a coronary artery. Atherosclerosis can be described by a thickening of the artery walls due to a build up of cholesterol forming an atherosclerotic plaque [5], see Figure 1.2. Coronary artery disease is the most common cause of CHD and the leading cause of death worldwide [6]. Coronary artery disease can be treated by bypass surgery, percutaneous transluminal angioplasty also known as balloon angioplasty, and angioplasty with the implantation of coronary stents.

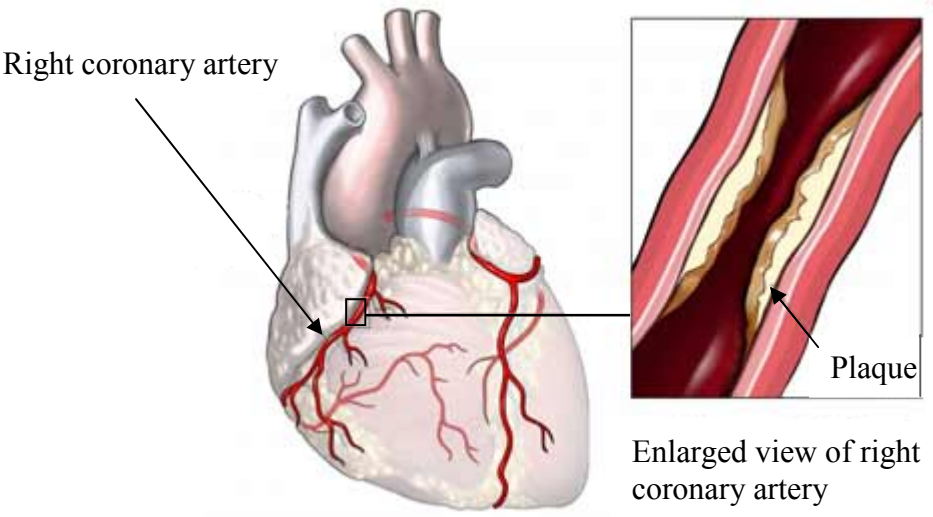

Figure 1.2: Illustration of atherosclerotic plaque in right coronary artery (adapted from www.mountsinai.org) [7]

1.3 Revascularisation Procedures

As coronary artery disease progresses, the plaque build-up can lead to almost complete obstruction of the coronary artery lumen, thus restricting blood flow to the myocardium and in severe cases leading to myocardial infarction (heart attack). If the disease is detected in its early stages, the effects can be improved by lifestyle changes, e.g. improvements in diet and exercise, cessation of smoking and reduction of stress. Depending on the severity of the disease, life-saving vascular procedures such as balloon angioplasty, stenting, bypass grafts and stent grafts may be required.

Depending on the location and severity of the blockage, the surgeon may decide to carry out a coronary artery bypass graft procedure, one of the most common operations performed in the United States, with more than 500,000 procedures performed each year [8]. Coronary artery bypass graft surgery is quite an invasive procedure whereby a healthy blood vessel is removed from one area of the body and placed around the damaged or blocked vessel, thus redirecting the blood flow through the healthy artery, see Figure 1.3.

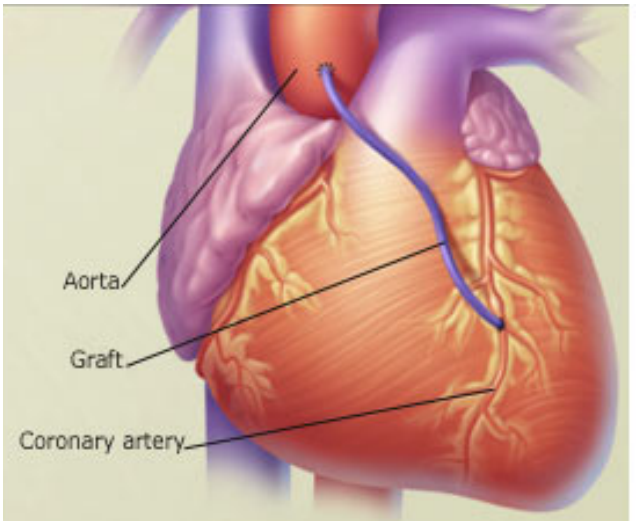

Figure 1.3: Illustration of coronary artery bypass graft (adapted from WebMD) [8]

This procedure can sometimes be carried out through minimally invasive surgery in certain cases where the affected area is accessible. This has major benefits over open heart surgery such as less scarring, shorter hospital stay and recovery times, less bleeding and less potential for infection.

The ability to open blocked blood vessels via percutaneous coronary interventions (PCI) such as balloon angioplasty has revolutionized the treatment of coronary artery disease, where percutaneous means through the skin. Two common minimally invasive surgical procedures for the treatment of coronary artery disease include Percutaneous Transluminal Coronary Angioplasty (PTCA) and Coronary Stenting (CS). Both PTCA and stenting are catheter based interventional procedures, both intending to restore blood flow to the heart.

PTCA was introduced into clinical practice in 1977 by Andreas Gruentzig and has become progressively established. PTCA involves passing a low profile deflated balloon through the arterial system (usually through an incision in the femoral artery) to the stenosed coronary artery. Once in place, the balloon is then inflated to a pressure of approximately 9 atm causing the balloon to expand to its predetermined diameter, and thereby expanding the narrowed vessel by pushing the plaque out against the artery wall. In such a way, the inner lumen is increased and blood flow to the heart muscle is restored, see Figure 1.4.

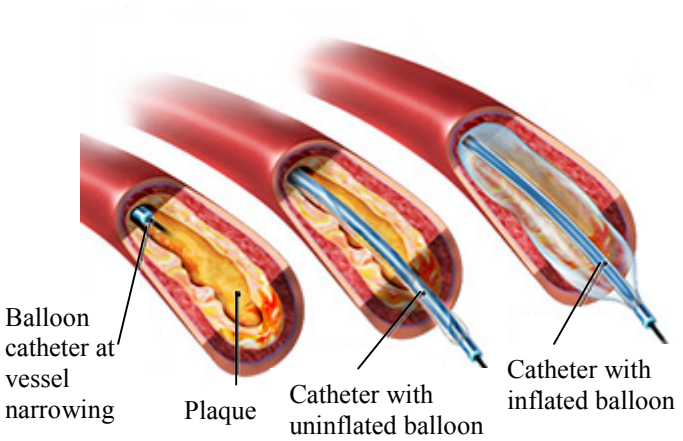

Figure 1.4: Illustration of PTCA procedure (adapted from www.orlandocvi.com) [9]

Although this procedure seems quite uncomplicated in comparison to bypass surgery, 30% to 50% of patients experience restenosis thus necessitating a repeat procedure or bypass surgery [10]. This renarrowing of the artery can come simply from elastic recoil of the tissue following balloon removal or as a result of damage imposed on the arterial wall due to the high pressures imposed during the angioplasty procedure. In order to reduce this problem of restenosis, a bare metal or drug eluting stent is sometimes mounted on the end of the balloon tipped catheter and used to hold the artery open permanently. These small, expandable wire cylinders are meshlike, thus allowing for the cells lining the arterial wall to grow through the stent, permitting normal biological behavior to continue. Once the stent is in place the balloon is deflated and removed from the patient. In the case of evaluating the optimal design for a metal stent the goal is to design a stent with the appropriate radial stiffness that would be required to hold the artery open without damaging the arterial wall.

Initially it was reported that drug eluting stents had 0% restenosis, however, results from clinical trials have reported a restenosis rate of up to 9% [11], see Figure 1.5. This was demonstrated in the SIRIUS clinical trial, which compared a sirolimus-eluting stent with a standard uncoated stent [12]. The risk of subacute thrombosis remains a concern following stent placement of both bare metal and drug-eluting stents. Trials have shown that PTCA and stenting are equally as effective as coronary bypass surgery with the exception that symptoms recur more often following PTCA and stenting and a repeat revascularization is required in 20-30% of patients. Volzke *et al.* investigated the long term prognosis after balloon angioplasty (PTCA), coronary stenting (CS), and coronary artery bypass grafting (CABG), and reported advantages of CS over PTCA with regard to major adverse cardiac events (MACE) [13].

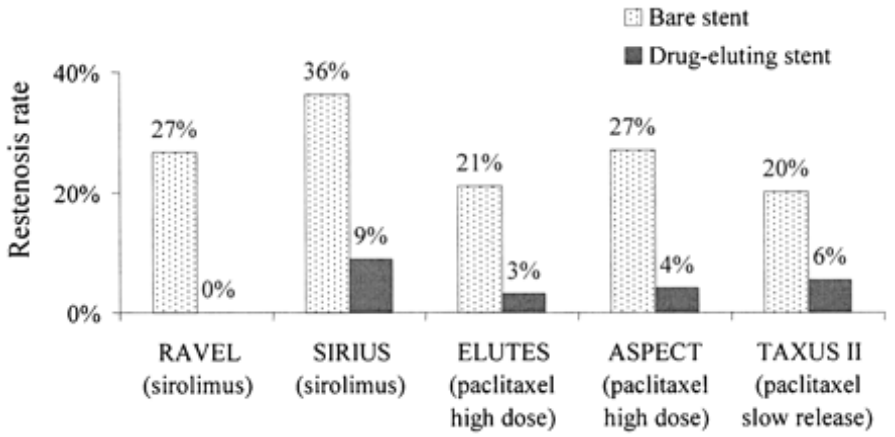

Figure 1.5: Graph showing angiographic restenosis in drug-eluting stents [11]

In order to realistically predict the successful outcome of these vascular devices, accurate data are required to describe the mechanical behavior of the stenosed coronary arteries upon stent expansion. Numerical modelling is a tool which is used extensively today to design, optimise, and preclinically test these devices [14]. Computational methods using nonlinear finite element analysis have evolved as a means of modelling arterial behavior and the impact of this behavior on stent design. This eliminates the need for rapid prototyping which does not provide any quantitative information on the functional mechanical performance of an actual device *in vivo*. These numerical models rely heavily on accurate experimental data that describe the mechanical properties of the arterial tree enabling more accurate biological reactions to medical devices such as balloons and stents to be predicted [14].

1.4 Aims & Objectives of the Study

The main objective of this study was to investigate the validity of the numerical methods used to simulate a Driver stent expansion inside a mock artery using experimental techniques. An experimental rig was used to evaluate certain stent parameters during Driver stent expansion and these parameters were then compared to the numerical models. Alongside clinical studies, many numerical studies are carried out using finite element methods to investigate and compare different stent designs and in some cases to evaluate their propensity to cause in-stent restenosis. This has been carried out by including the arterial wall in finite element simulations and analysing the stresses induced in the arterial wall upon stent expansion. These finite element analyses have been crucial in strengthening

results obtained from clinical studies. For this reason it is important to evaluate the accuracy of the numerical methods used. This study aimed to contribute to this goal by evaluating different numerical methods used to simulate both the free expansion of the Driver stent and expansion of this stent inside a mock artery.

To achieve this goal, the following actions were carried out:

1. Extensive tensile testing was carried out on both porcine coronary arteries and numerous samples of Sylgard® elastomeric material with varying elastic properties. By doing so, a suitable match in mechanical properties of Sylgard® to that of porcine coronary arteries could be determined.
2. Once a suitable blood vessel analogue was determined, a rig was designed and developed to repeatedly produce mock arteries with geometries representative of porcine coronary arteries.
3. A numerical model of the Medtronic Driver stent was created in ANSYS and its expansion simulated using the finite element code MSC Marc Mentat. The stent was expanded both freely and inside a representative Sylgard® mock artery using two different methods of expansion. The uniaxial tensile properties resulting from the Sylgard® material were used to describe the Mooney-Rivlin constitutive model in the numerical simulation.
4. Actual Driver stent expansions were carried out with and without the presence of a Sylgard® mock artery and the expansion analysed experimentally.
5. Both the numerical models and the in-vitro experimental models were evaluated for recoil (both radial and longitudinal), foreshortening and dogboning, such that the results could be compared to see how the numerical simulations represented the in-vitro experimental simulations.

Overall, this study aims to provide useful experimental techniques which can be used in the validation of numerical simulations which in turn can be used to provide realistic and valuable information to aid the optimisation of coronary stents.

CHAPTER 2

LITERATURE REVIEW

2.1 Structure and Composition of the Arterial Wall

Before identifying a suitable blood vessel analogue, it is important to understand the structure and mechanical properties of the vessel being replicated. The arterial wall is a complex structure which has multiple physiological functions. There are three types of arteries, namely, elastic, muscular, and arterioles [5]. The large central arteries are the most elastic, with a gradual increase in stiffness out towards the peripheral arteries. The aorta and carotid arteries are examples of elastic arteries. Elastic arteries experience the greatest pressures as they are closest to the heart. These arteries contain more elastin than smooth muscle content in the media. Examples of muscular arteries include the femoral and tibial arteries in the leg and the coronary arteries.

The arterial wall is mainly composed of elastin, collagen, and cells (endothelial cells, smooth muscle cells, and fibroblasts). Elastin fibres are taut tubular fibres and exhibit a low stiffness of 0.6 MPa in comparison to the thick, tortuous collagen fibres which have a high stiffness of 1×10^3 MPa [15]. Elastin fibers also exhibit a lower ultimate tensile strength of 3 MPa in comparison to collagen which has an ultimate tensile strength of 50-100 MPa [15]. The involuntary smooth muscle cells are responsible for the active properties of the blood vessel wall and have an extremely low stiffness of 0.01MPa [16]. Due to the higher stiffness and strength of collagen fibres, they are responsible for maintaining the structural integrity of the vessel wall. Elastin fibers are highly elastic and can

stretch up to 60% and still remain elastic [16]. This enables the vessel to expand and recoil during pulsatile flow [17]. Elastin fibers are known to bear the lower physiological loads caused by the pulsing of the heart [16].

The arterial wall consists of three layers:

1) The tunica intima
2) The tunica media, and
3) The tunica adventitia.

The structure of an artery wall can be seen in Figure 2.1.

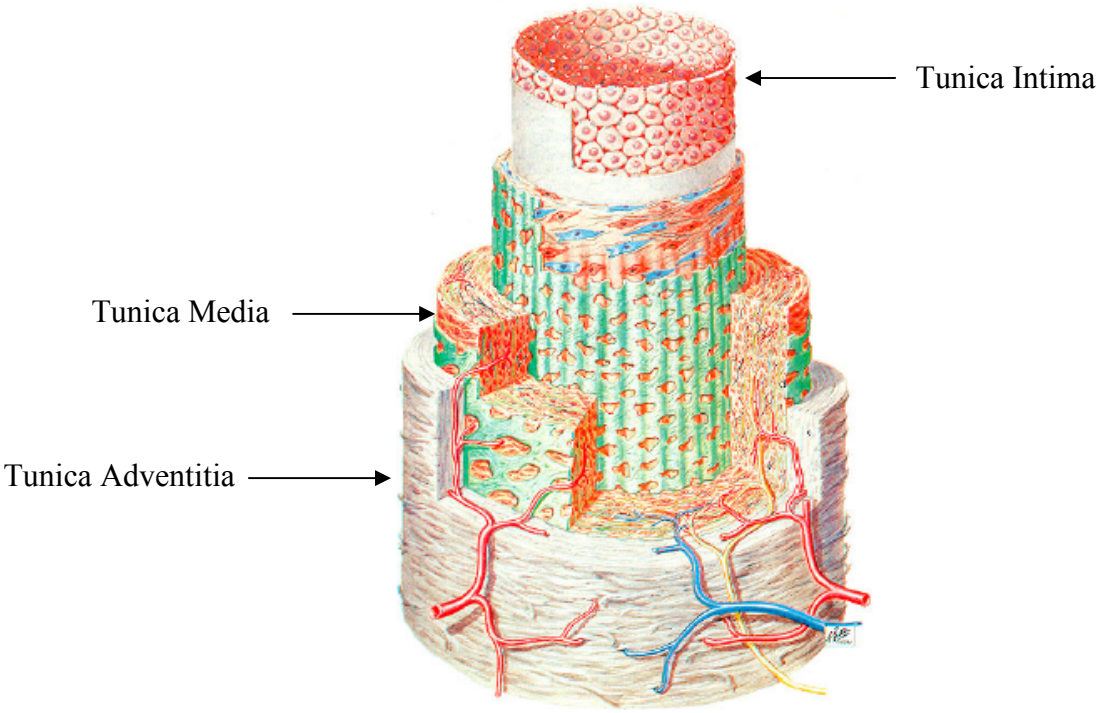

Figure 2.1: Illustration of structure of arterial wall (adapted from [18])

Each arterial layer presents specific material properties to assume a particular role in the vascular system.

2.1.1 The Tunica Intima

The tunica intima is the inside layer of the arterial wall (as seen in figure 2.1) and is composed of a smooth, nearly frictionless layer of endothelial cells. A study carried out by Dunn *et al*. quantified friction between a polished glass pin and a single layer of arterial endothelial cells to be between 0.03 and 0.06 [19]. For this reason many researchers carrying out finite element analyses of stent expansions have assumed frictionless contact between the inner surface of the artery and the expanding balloon [20].

A layer of elastic tissue called the internal elastic lamina separates the tunica intima from the tunica media. The endothelium constitutes a selective barrier between the blood [19] and the artery wall such that it prevents thrombosis and bacteria in the blood from entering the wall. This is critical in the case of stenting whereby the stent comes into direct contact with the intima upon deployment.

2.1.2 The Tunica Media

The tunica media is the middle layer of the arterial wall and is usually the thickest layer. This layer consists of 33% smooth muscle cells, 24% elastin, 37% collagen, and 6% ground substance [16]. The smooth muscle cells are arranged circumferentially around the vessel. The composition of these components represents a continuous fibrous helix [19] with the artery wall becoming stiffer as it reaches the outer layer [21]. Sheets of elastin separate the media from the intima and adventitia. The main function of this layer is to provide the muscle contraction, and elastic stretch and recoil of the artery, which also play an important role in the design optimisation of coronary stents.

2.1.3 The Tunica Adventitia

The tunica adventitia is the outermost layer of the arterial wall and is composed mainly of collagen fibers, i.e. 78%, and is thus responsible for carrying the highest

loads and maintaining the structural integrity of the vessel [16]. The adventitial layer constitutes approximately 10% of the coronary vessel wall.

The overall mechanical properties of the arterial wall are determined by how different compositions of collagen and elastin are connected to one another. The amount of elastin, collagen, and smooth muscle cells vary throughout the vascular tree, thus varying the mechanical properties throughout the vascular tree also. It has been found that the amount of collagen and smooth muscle increase while the amount of elastin decreases at more distal locations in the body, i.e. as you move further away with distance from the heart [22]. The general rule is that when the elastin ratio is higher than the collagen ratio, the elastic modulus decreases and the distensibility increases and vice versa [23].

A study carried out by Saikrishna *et al.* reported a range in the inner diameter of coronary arteries for a Caucasian population of 1.06±0.26mm to 2.38±0.47mm [24]. The thickness of atherosclerotic coronary arteries has been reported to range from 0.56mm to 1.26mm, depending on the location of the coronary arteries [25].

2.2 The Mechanical Properties of Arterial Tissue

2.2.1 Nonlinearity

This is one of the most important properties of the artery wall and is key to the elastic stability of highly distensible arteries, protecting them against aneurysms and "blowout" [26]. Uniaxial tensile tests on vascular tissue reveal highly non-linear stress-strain behavior, with higher distensibility in the low stretch region and progressively lower distensibility in the high stretch region. This effect is known as the "strain stiffening effect", i.e. the tissue becomes stiffer the more it is stretched. This non-linearity is mainly due to the presence of the elastin and collagen fibers and the fact that the collagen fibers are initially loose before any loading is applied. For this reason the initial part of the curve has a low stiffness, as the elastin stretches and the wavy collagen begins to straighten out. As more strain is applied to the vessel, the modulus of elasticity increases, as the collagen

fibers reach their limits of elongation [16]. It can be seen clearly from the graph illustrated in Figure 2.2 that the behaviour of the tissue is highly non-linear. Since Young's Modulus is defined as the slope of the elastic curve, it can be seen that the stiffness of the tissue actually increases as it is being stretched and is not constant.

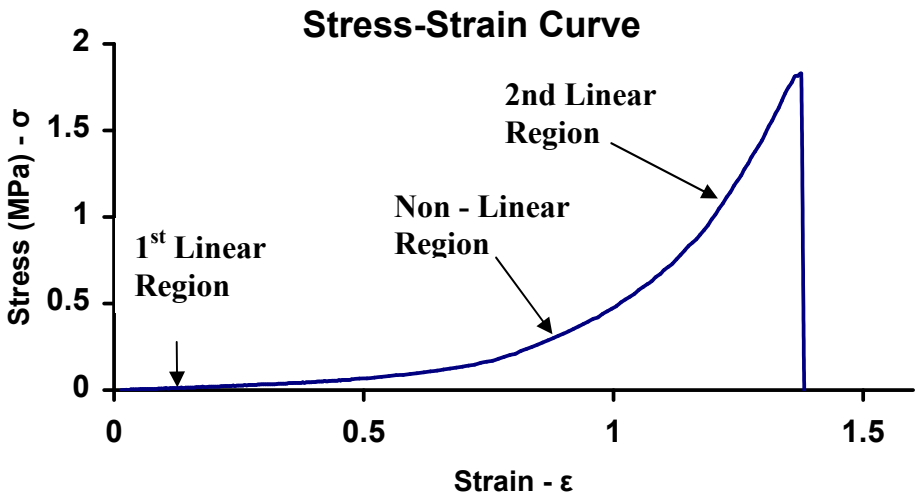

Figure 2.2: Characteristic Stress-Strain curve

Alan C. Burton [26] proved this theory by examining the separate roles of elastin and collagen which were removed from human iliac arteries. The collagen fibers were isolated from the tissue using crude formic acid and the elastin was isolated using crude trypsin. By removing the collagen fibers and thus looking at the elastin fibers alone, they were seen to obey Hooke's Law over a wide range. A similar observation was made for the collagen fibers except for the start of the curve which was somewhat non-linear [26].

2.2.2 Inhomogeneity

As previously mentioned arteries are composed of several different constituents and are therefore highly inhomogeneous. The quantities of collagen, elastin, and smooth muscle cells also vary throughout the vascular tree. In this way the mechanical properties of arterial tissue are dependent on the location of the tissue in the vascular tree. For example the collagen:elastin ratio increases as you move down towards the distal end of the vascular tree [16].

2.2.3 Anisotropy

Anisotropy is the ability of the tissue to behave differently in different directions, i.e. the Young's Modulus is larger in the axial and circumferential directions than in the radial direction [27]. Deformations of the artery wall material are predominantly radial and circumferential in nature, however they are also subject to a longitudinal tethering force [28]. This longitudinal loading has been found to be due to the uniform attachment of the arterial wall to the surrounding perivascular tissues [28].

2.2.4 Viscoelasticity

Viscoelasticity can be defined as the time-dependent material behavior where the stress response of that material depends on both the strain applied and the strain rate at which it was applied. Viscoelasticity is the ability of the tissue to exhibit both solid-like and fluid-like behaviour. The solid behaviour of the tissue refers to its ability to exhibit a certain resistance to deformation like an elastic body. The fluid like behaviour of the tissue refers to its ability to 'flow' due to a constant force [16].

It has been found from previous studies that biological soft tissues are mechanically quite insensitive to strain rate. It was found that the stress-extension ratio curves among three order differences in tensile speed showed no significant differences [22].

2.2.5 Incompressibility

The vessel wall is nearly incompressible. It can still be squeezed or extended in one or two directions. In this way, when the artery is deformed in one direction, an opposite deformation will take place in the other directions in such a way that the volume of the tissue remains constant. Carew *et al.* (1968) carried out extensive tests along the aortic tree, pulmonary artery, and the common carotid artery and concluded that arteries may be considered incompressible [29].

2.3 Sylgard® 184 Silicone Elastomer

Sylgard® 184 elastomer, also known as polydimethylsiloxane (PDMS) was chosen to construct mock arteries which were used in this study to provide information on the expansion characteristics of the Driver stent. Sylgard® 184 is a registered trademark of Dow Corning Corporation and is generally used in electronic applications to provide environmental protection [30]. This material was chosen mainly due to its variable elastic properties determined by the curing process and the ratio of elastomer to curing agent, its transparent nature, and its biocompatibility. The Sylgard® material was supplied as a two part kit consisting of two liquid components, i.e. a base and a curing agent. By mixing the two components, silicone can be formed and the stiffness of the silicone is dependent on the ratio of base to curing agent used.

This Sylgard® material has been used in the construction of mock aorta models which were used to analyse pulsatile flow through the mock aortic vessels by Peattie *et al.* [31] and Yip *et al.* [32]. A study carried out by Olbrich and Murray [33] to evaluate a technique for obtaining the mechanical properties of coronary arteries using mock arteries, used the silicone rubber material SILASTIC®. This material is also a product of Dow Corning and consists of a two part base and curing agent mix. A 10:1 mix was used to construct the mock arteries which is comparable to the Sylgard® mix used in this study.

2.4 Numerical Modelling of the Arterial Wall

Finite element analysis is widely used to study not only the stresses induced in the arterial wall due to stent-artery interactions, but also the possible relationship between these stresses and cardiovascular disease. Salzar *et al.* [34] investigated the possible correlation between regions of elevated wall stress and the development of atherosclerotic lesions in the carotid artery bifurcation, whereby the arterial wall was modeled as an isotropic material. In this study a highly localized stress concentration of approximately 9 to 14 times the proximal

circumferential wall stress was seen to occur at the point of bifurcation in the representative finite element models. As the carotid bifurcation is known to be susceptible to atherosclerosis it was possible to correlate these elevated wall stresses shown in the numerical models with this condition. Prendergast *et al.* [35] developed a three dimensional, single layer model of a healthy artery to measure the propensity of a stent deployment to cause restenosis. In this study, the prolapse or draping of the arterial tissue between the stent struts was used as the determinant to predict the restenosis rates for four commercially available stents.

The constitutive model used to describe the behavior of the arterial wall, or as in this study, the mock arterial wall, is an important consideration in the finite element analyses of stent artery interactions. Due to the extensive use of finite element analysis techniques in the preclinical testing of stents, it is important to represent a realistic situation. A constitutive equation is a phenomenological mathematical model used to describe the relationship between stress and deformation. Constitutive equations used to describe arterial tissue consist of unknown constants that need to be fit with experimental data obtained through testing of the material being described. Arterial tissue undergoes strains that qualify as large deformations, and are generally described as elastic non-linear materials. Holzapfel *et al.* [19] proposed a combination of exponential and polynomial type strain energy functions which described the anisotropic behavior of arterial tissue.

Holzapfel *et al.* amongst many other researchers have developed constitutive material models which can be used to describe the elastic, non-linear stress strain behavior of arterial tissue [19, 36, 37]. The hyperelastic behavior of an artery is generally quantified in terms of a strain energy density function, W, where W is defined in terms of suitable strain components. By differentiating W with respect to a strain component the corresponding stress component, S, can be determined as follows:

$$S = \frac{\partial W}{\partial E} \qquad \text{[Eqn. 1]}$$

Where E is the Green-Lagrangian strain tensor, S is the corresponding stress component, and W is the strain energy density function.

The strain energy density function, W, for an isotropic, hyperelastic material can be described using a polynomial or exponential constitutive model. The Mooney-Rivlin hyperelastic model is a polynomial equation which is widely used to describe the mechanical behavior of incompressible, isotropic, hyperelastic materials and is given by the following equation [38]:

$$W(I_1,I_2,I_3,) = \sum_{i,j=0}^{\infty} a_{ij}(I_1-3)^m(I_2-3)^n(I_3-3)^0, a_{00}=0 \qquad \text{[Eqn. 2]}$$

Where a_{ij} are material constants, and m and n are exponents which determine the order of the model. The stretch invariants for the material are defined through the principal stretches ($\lambda_1, \lambda_2, \lambda_3$) of the material as:

$$I_1 = \lambda_1^2 + \lambda_2^2 + \lambda_3^2 \qquad \text{[Eqn. 3a]}$$

$$I_2 = \lambda_1^2\lambda_2^2 + \lambda_1^2\lambda_3^2 + \lambda_2^2\lambda_3^2 \qquad \text{[Eqn. 3b]}$$

$$I_3 = \lambda_1^2\lambda_2^2\lambda_3^2 \qquad \text{[Eqn. 3c]}$$

Many researchers, including Lally *et al*. [39] have used different forms of the Mooney-Rivlin constitutive model in their simulations to model the artery wall in order to determine realistic vessel stresses upon stent deployment.

Although many constitutive models of arterial tissue assume isotropy, it is a well known fact that the arterial wall is anisotropic given the three-layered nature of the artery wall. Holzapfel and Ogden [19] proposed a combination of exponential and polynomial type strain energy functions which described the anisotropic nature of arteries. This was achieved by dividing the strain energy function into the addition of the isotropic strain energy function and an anisotropic strain

energy function. As this constitutive model is not available for use in commercially available software and also due to the fact that the degree of anisotropy is highly patient specific it was not deemed necessary for the purpose of this study. An isotropic model which includes the main features of arterial tissue such as its non-linear stress stiffening behaviour and its incompressibility is sufficient.

2.5 Coronary Stenting and Restenosis

Coronary stenting was introduced into clinical practice in 1987, just ten years following the introduction of percutaneous angioplasty. Stent performance depends on both the material properties and the physical attributes of the stent. The ideal stent material will contain the following characteristics:

1. Good biocompatibility – To ensure no adverse reaction occurs when the stent is implanted in the body.
2. Fatigue resistant – Fatigue failure can occur in stents due to the cyclic stresses created by the blood flow
3. Good radiopacity – To enable the visibility of the stent under standard X-ray and MRI
4. Sufficient radial strength – Low yield strength is required to allow for sufficient stent expansion and high tensile properties are required after expansion to achieve sufficient radial strength to maintain patency.
5. Low recoil – both radial and longitudinal
6. Good axial and radial flexibility – To enable navigation through the tortuous vessel.
7. Good deliverability – To enable access to smaller vessels.
8. Low profile – Higher tensile properties enable the use of thinner stent struts and therefore an overall lower profile. This also improves the flexibility and deliverability of the stent.

Studies have shown the benefits of coronary stenting over balloon angioplasty, such as an improved rate of procedural success, a lower rate of angiographically

detected restenosis and a less frequent need for revascularistaion of the original coronary lesion [40]. The need to re-intervene on the treated vessel was shown to be reduced from 23.3% to 13.5% at seven months in the BENESTENT (Belgian Netherlands STENT) trial [41].

Restenosis, which is the re-narrowing of the artery lumen, still remains problematic with percutaneous coronary intervention today. As previously mentioned, the rate of restenosis is lower for stenting in comparison to balloon angioplasty, with restenosis rates of 25% and 40%, respectively [39, 40]. The factors which lead to restenosis post balloon angioplasty include acute vessel recoil, thrombus formation, chronic constrictive remodelling of the artery and neointimal growth [42]. In-stent restenosis is predominantly caused by the onset of neointimal formation, which is a result of the injury caused to the vessel wall upon stent expansion. The breakthrough of drug-eluting stents however, has enabled the local delivery of anti-proliferative drugs to the site of injury, thus suppressing the formation of neointimal hyperplasia. Sousa *et al.* have reported the reduction in target lesion revascularization (TLR) and major adverse cardiac events (MACE) from 21.3% to 5.8% and from 26.7% to 12.0% respectively, when using a drug-eluting stent [43].

Laroche *et al.* [44] carried out a finite element analysis to try and predict and thus compare the friction in balloon angioplasty and stent implantation. The results demonstrated differences between balloon angioplasty and stent implantation mechanics whereby the friction work on the endothelium in stent implantation is lower than that in balloon angioplasty. This was found to be due to the fact that the presence of the stent actually constrained the balloon to a slower and more symmetrical deployment than when the balloon is deployed alone. This suggests that the stent might be playing a protective role against friction damage to the endothelium and this may be attributed to the lower restenosis rates found with stent implantation.

2.6 Finite Element Analysis of Stenting

Finite element analysis provides a relatively cost effective and extremely beneficial research tool to optimize the mechanical properties of stents when physical test methods are not an option. Numerical modelling of stents has been widely used to not only investigate the influence of stent design on the stent and artery, but also to provide a complementary analysis to experimental studies. In the current study, the experimental analysis of the Driver stent has been compared to that of the numerical analysis to provide an insight into the applicability of the numerical methods used. Many researchers have used the finite element method to investigate the mechanical behavior of coronary stents and to evaluate such stent characteristics as recoil, foreshortening and dogboning [45, 46, 47]. Others have investigated the influence of the expansion mechanism on the artery wall and in some cases on stenosed vessels [14, 39, 48, 49]. Further finite element analysis has been carried out to model the behaviour of nitinol self expanding stents and investigate the self expansion mechanism and the subsequent interactions with the vessel wall [50, 51, 52].

Dumoulin and Cochelin [53] were one of the first researchers to investigate numerically the expansion mechanism and long-term behavior of a balloon-expandable stent. The stent was modeled in the commercial code ABAQUS, whereby the elasto-plastic behavior of the 316L stainless steel stent was modelled. The balloon expansion was simulated as a uniform radial pressure applied to the inner surface of the stent. The stent expansion behavior was characterized by foreshortening, radial recoil, longitudinal recoil, and the weakness of the structure for different diameters of stent expansion. The results showed that upon expansion the major equivalent plastic strains were localized in the corners while the major stresses are located in the middle of the cell junctions. The stent endurance study indicated that the stent could withstand an infinite number of cardiac cycles. The results on expansion and recoil also highlighted that beyond the design and mechanical properties of the stent, the deployment pressure was also another factor to be taken into consideration.

Chua *et al.* [54] used the commercially available packages LS-DYNA (for solution) and ANSYS (for the pre- and post- processing) to investigate the finite element simulation of stent expansion. In their study, the stent was expanded freely by applying a uniform internal surface load whereby the rate of the applied load was increased in the second simulation. Results showed that by increasing the speed of the application of pressure to the stent resulted in a larger displacement. It was also found that a faster speed of pressure application resulted in greater foreshortening of the stent. A further study was carried out by Chua *et al.* [55] which incorporated the influence of a balloon into the finite element analyses. In this study, a surface to surface contact algorithm was adopted to deal with the nonlinear contact problem and the balloon was modeled using a hyperelastic material model. A further and most recent study carried out by Chua *et al.* [56] involved the three-dimensional stent-balloon expansion inside a stenosed artery model. The results showed that the maximum surface contact stress was elevated where the plaque and stent come into contact, resulting in greater degrees of plaque protrusion between the stent struts. One of the major limitations to the study is the representation of the non-linear arterial tissue as a linear isotropic material. This assumption would affect the stent expansion mechanism and the resulting stress distribution in the arterial wall.

Migliavacca *et al.* [57] also simulated the deployment of an intravascular stent into stenotic coronary arteries using the commercial code ABAQUS to perform the large deformation analysis. The stent modeled was representative of the Palmaz-Schatz stent whereby the 316LN stainless steel material was described through a von Mises-Hill plasticity model with kinematic hardening. The artery wall and plaque were modeled using hyperelastic constitutive equations which described the non-linear stress strain behavior of these materials. The results showed the stress to be concentrated in the contact areas between the plaque and the stent. It was also found that the stiffer the plaque, the higher the pressure required to reach the same expanded inner diameter. This type of study provides valuable information in understanding the vessel response to stent deployment.

Recent studies of numerical stent expansions have also included the artery and plaque in the analyses. Lally *et al.* investigated the mechanical behavior of two

different stent designs, the S7 stent and the NIR stent, on the biomechanical interaction between each stent and the artery during stent expansion [39]. It was found that the more flexible S7 stent design would cause lower arterial stresses to an atherosclerotic vessel with a localized stenotic lesion when compared to the NIR. This result was also found to correlate with the findings of clinical studies whereby the S7 has been found to be less likely to cause restenosis when compared to the NIR stent design.

As numerical models are always approximations of the physical reality, it is of utmost importance to validate the numerical results using experiments. Walke *et al.* [46] carried out both an experimental and numerical analysis of the GENESIS™ vascular stent which confirmed the effectiveness of the numerical methods used. The stent was expanded experimentally inside a polyethylene pipe whereby the balloon pressure was increased incrementally and the subsequent stent diameters recorded. The stent was also modeled numerically whereby the expansion pressure was uniformly applied to the inner surface of the stent in small increments. The results showed a good correlation between experimental and numerical results for the expanding stent diameter at incremental pressures.

Another study which compared the numerical stent expansion results to real time experimental results was carried out by Migliavacca *et al.* [45]. In this study the Cordis BX Velocity stent was freely expanded both numerically and experimentally. The numerical expansion consisted of a large deformation analysis using the ABAQUS commercial code, whereby a uniform linearly increasing radial pressure was applied to the inner surface of the Cordis BX Velocity stent until it reached a value of 1.2 MPa. Similarly, an actual Cordis BX Velocity stent was expanded to a maximum pressure of 1.2 MPa. In both expansions the diameter of the stent was recorded at various pressures. The results showed a similar initial expansion for the numerical and experimental pressure-diameter curves. However, at high pressures, large discrepancies exist between the numerical and experimental results which may be attributable to the absence of a balloon in the numerical model. Another interesting finding was the similarity in the stress field between the experimental and numerical models once the stents

achieved their expanded nominal diameters but not for the same inflation pressure.

Barragan *et al.* [58] carried out a purely experimental comparative analysis on stents whereby twenty-two coronary stents were expanded (i) freely and (ii) with an external radial pressure in the form of a transparent polyurethane tube. The elastic recoil was measured over time for all stents tested such that the values could be compared. Elastic recoil was found to range from 2% to 18% and was found to be dependent on the design of the stent with a significant reduction between the mean recoil for tubular stents as compared with coil stents. No significant difference was noted between the results for the elastic recoil recorded with and without the tube present. This indicates that elastic recoil measured without stress is an adequate approach for some stents. This type of study could enable clinicians to predict the final behavior of a stent in an artery.

2.7 Summary

It can be concluded from this literature review, that the extensive research carried out to investigate and evaluate the performance of different stent designs on various stenosed arteries is crucial to the development and improvement of these medical devices. Complex finite element models simulating the interaction between stents and the arterial wall have gained importance in the prediction and calculation of the stresses generated in the arterial wall after a stenting procedure. These finite element analyses have also been used by researchers as a tool to understand the long term loading of the stent involving millions of cardiac cycles, a test which would be extremely difficult to duplicate in a test lab. This has in turn provided a valuable insight into the propensity of the various stent designs and arterial anatomies to cause in-stent restenosis. Numerous clinical studies have also proven that stent design has an impact on the level of restenosis following stenting. With more and more new stent designs emerging on the market today, there is an increasing need for research and development in this area.

In light of this research it has been noted that suitable and reliable experimental methods must be devised such that they can be used to validate the numerical methods used by researchers. The current study determines a suitable experimental stent expansion rig and thus investigates the validity of numerical models of a Driver stent expansion in its free state and also inside a mock artery. Two different numerical expansion methods are investigated and compared to the realistic experimental expansion such that a reliable and reproducible method of numerical stent expansion can be determined.

CHAPTER 3

MATERIALS AND METHODS

3.1 Introduction

The purpose of this study is to examine stent behaviour and to determine if this behaviour can be represented numerically using finite element methods. This was achieved by expanding Driver stents (Medtronic AVE) inside Sylgard® elastomeric mock arteries and evaluating the behaviour of the stent with regard to recoil (both radial and longitudinal), foreshortening and dogboning. The aforementioned stent parameters are evaluated by stent manufacturers, to ensure minimal effects are noted, as such behaviour can incur damage to the artery wall upon deployment of the stent. Finite element models of the Driver stent were developed and the stents were deployed in vessel geometries representing that of the Sylgard® elastomeric mock arteries.

To create mock arteries representing porcine coronary arteries, tissue testing was first carried out on porcine coronary arteries excised from pig hearts. Extensive tensile testing of the coronary arteries was carried out in both the longitudinal and circumferential directions such that the tissue behaviour could be fully characterised. Tensile testing was also carried out on various ratios of Sylgard® material such that a suitable match in properties to that of porcine arteries could be determined. A rig was designed and developed to manufacture the mock arteries to represent the typical dimensions of a porcine coronary artery. Driver

stents were deployed inside these mock arteries and the behaviour of the stent and artery analysed.

The numerical simulations were generated by inputting the mock artery and stent geometries, the material properties for the chosen mock artery and the stent, and the appropriate loading and boundary conditions to represent the physical stent expansion inside the mock artery. The finite element model of the Driver stent was developed in the finite element software package ANSYS (Canonsburg, PA, USA) and subsequently transferred into Marc/Mentat (MscSoftware, Santa Ana, CA, USA) where the analysis was carried out. The properties of MP35N cobalt chromium alloy were assigned to the stent material. The material behaviour of the Sylgard® mock artery was obtained from the tensile testing carried out. The finite element analyses were carried out to compare the results obtained for recoil, foreshortening and dogboning, to those obtained in the experimental models and to determine whether the numerical methods used could accurately represent this behaviour.

3.2 Uniaxial Tensile Testing & Material Characterisation

3.2.1 Determination of Sylgard® Material Properties to Represent Porcine Coronary Arterial Tissue

3.2.1.1 Porcine Coronary Arterial Tissue Preparation & Testing

Extensive uniaxial tensile testing was carried out on porcine coronary tissue. Porcine coronary tissue was chosen for testing due to the limited availability of human arterial tissue. Porcine arterial tissue has many similarities to that of humans in terms of cardiovascular anatomy and physiology, including a comparable heart to body size ratio [59]. For this reason the results should give a relatively accurate indication of the mechanical properties of human coronary arteries.

The two main branches of the coronary artery, i.e. the right coronary artery (RCA) and the left coronary artery (LCA), were carefully excised from freshly harvested porcine hearts obtained from an abattoir, see Figures 3.1 and 3.2.

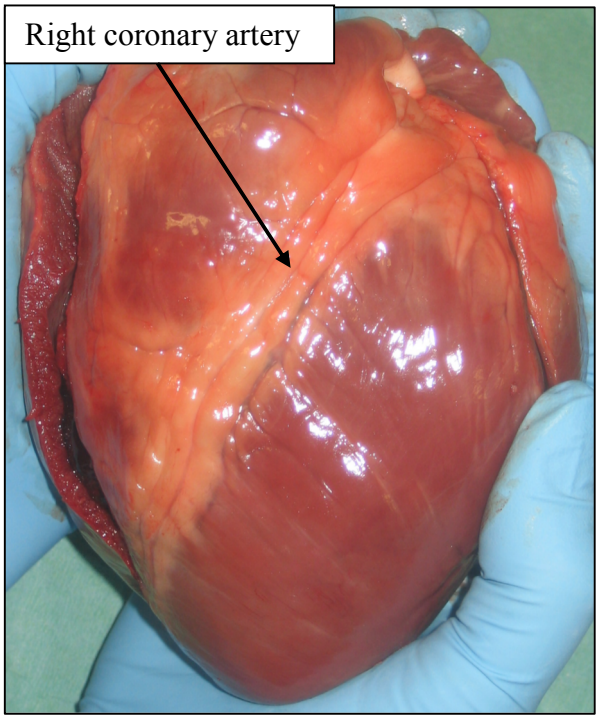

Figure 3.1: Image of heart showing right coronary artery

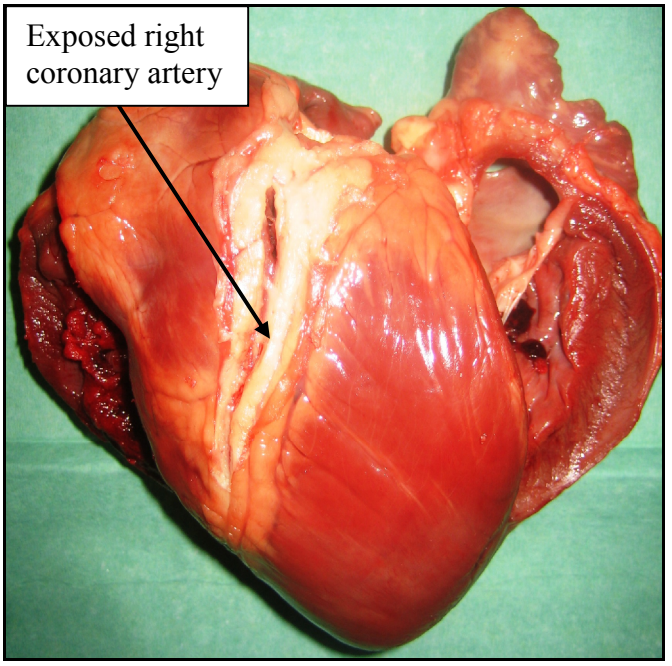

Figure 3.2: Image of heart showing exposed right coronary artery

All of the tissue obtained from the abattoir was taken from Landrace pigs weighing approximately 90 kg. All loose connective tissue was removed from the excised arteries and the arteries prepared for testing. Specially designed cutting tools were used to cut both ring-shaped and dogbone-shaped samples from the prepared arteries, see Figures 3.3 (a & b) and 3.4 (a & b).

At each specimen site, an additional piece of tissue running adjacent to the gauge length was cut to allow for the thickness of each specimen to be measured appropriately. To measure the tissue thickness, each sample was mounted on a glass slide and the measurements taken using a microscope fitted with a digital reticule. The thickness of each tissue sample was recorded at three different locations to allow for an average to be calculated. Each sample was tested within 48 hours of harvesting.

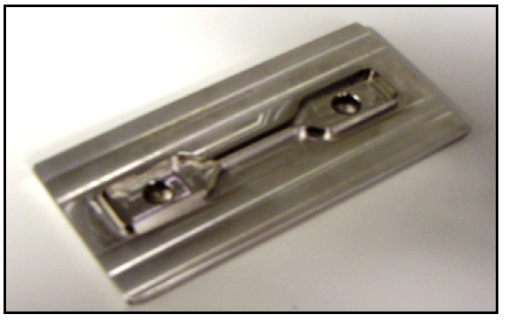

Figure 3.3 (a): Cutting device for dogbone shaped samples

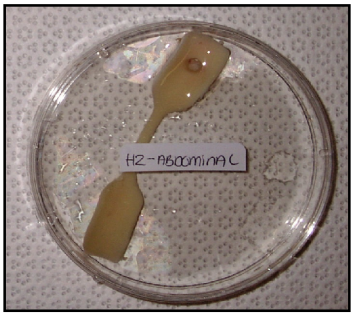

Figure 3.3 (b): Dogbone-shaped sample

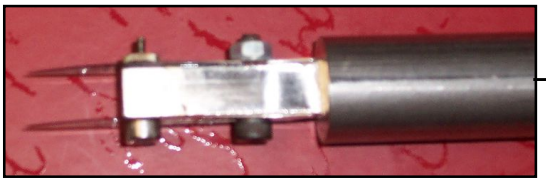

Figure 3.4 (a): Cutting device for ring shaped samples

Figure 3.4 (b): Ring-shaped sample

Uniaxial tensile testing was carried out on the tissue samples in both the longitudinal (using dogbone-shaped samples) and circumferential (using ring-shaped samples) directions using a 20 N load cell attached to a Zwick Z050 tensile testing machine.

The specimen data entered was as follows:

For longitudinal dogbone-shaped samples:

- Width – 2 mm
- Gauge Length – 12 mm approximately

For circumferential ring-shaped samples:

- Width = 2 mm
- Gauge Length – varied

The thickness of each specimen varied considerably from an average of 0.508 mm to 1.037 mm. For this reason the thickness was not entered into the test setup. Test limits were set to ensure that the test stopped when the test specimen failed. The data was logged at a sampling rate of 10/second thus ensuring a large amount of data for each test.

In both tests, a strain rate of 60% min^{-1} was used at all times and all specimens were continuously irrigated with 0.9% saline throughout testing. This strain rate was calculated by carrying out a stent expansion inside a Sylgard® mock artery and measuring the time and initial and final diameters of the vessel using a video extensometer such that the circumferential strain rate could be calculated as follows:

- Initial circumferential length of the vessel, C_i = 9.42 mm (D_i = 3mm),
- Final circumferential length of the vessel after balloon inflation, C_f = 10.99 mm (D_f = 3.5 mm),

  Where the circumference C = πD and D is the diameter of the vessel.
- Time taken to expand balloon = 17 seconds

To find the circumferential strain, ε_c:

$$\varepsilon_c = \frac{\Delta C}{C_i} = \frac{1.57}{9.42} = 0.17 \qquad \text{[Eqn. 4]}$$

Therefore, the arterial wall strains in the circumferential direction by 17%/17 seconds, and thus 60%/60 seconds. The same strain rate was used to test the dogbone-shaped samples in the longitudinal direction to eliminate any strain rate effect and ensure consistency.

Once the equipment was set up, the test specimens were secured carefully using custom built cylindrical holders for the ring-shaped specimens and pneumatic grips for the dogbone-shaped specimens, see Figure 3.5 (a) and (b) below. Rectangular pieces of aluminium oxide emery paper were used to hold the dogbone-shaped test pieces securely in place throughout the test. The ring-shaped samples were held in place using dowel pins measuring 0.76mm in diameter, which were inserted through holes in the upper and lower fixtures. See Figure 3.5 (a) for reference.

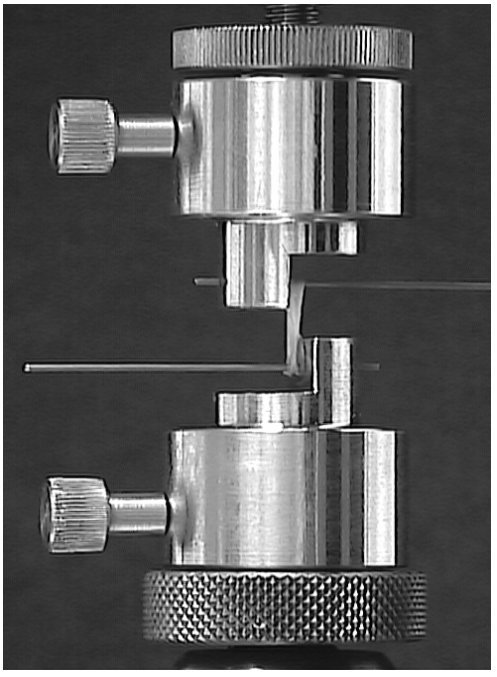

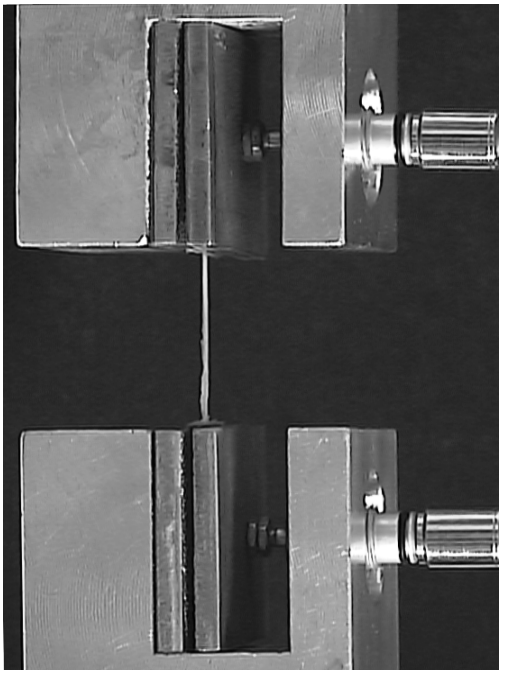

Figure 3.5 (a) Fixture to hold ring-shaped samples in place throughout tensile test. **(b)** Grips to hold dogbone-shaped samples in place throughout tensile test.

For all tensile testing carried out, the stress was determined by dividing the instantaneous load by the original cross sectional area. The strain was determined by dividing the instantaneous length by the original length, whereby the original length was taken as the gauge length at a preload of 0.05 N.

3.2.1.2 Investigating Preload

For the circumferential ring-shaped samples three different preloads were investigated to ensure that the correct preload was being used such that the tissue was always in slight tension at the beginning of each tensile test. This was not required to be carried out for the dogbone-shaped samples as the gauge length was fixed at 12 mm as per the design of the cutting device. As the gauge length for the ring-shaped samples could not be controlled it was important to find a suitable preload to be used for all samples such that the tissue was in slight tension prior to testing, otherwise the strain recorded at the beginning of the test would be representative of the straightening out of the material rather than the deformation whereby a strain is being applied to the tissue. The preloads investigated were 0.01 N, 0.05 N, and 0.1 N respectively. Three ring-shaped samples were taken from three separate right coronary arteries, resulting in nine samples in total. Each ring-shaped sample was cut to a width of 2 mm using a custom made cutter comprised of two scalpel blades set 2 mm apart and loaded on a handle. Specially designed fixtures were mounted on a Zwick Z050 tensile testing machine, which were used to hold the ring-shaped samples in place throughout the tensile test (refer to Figure 3.5 (a) above). The inner diameter of each sample was measured using a microscope prior to testing, such that the gauge length for each individual sample could be calculated using the following formula:

$$Gauge\ Length\ (GL) = \frac{\pi D_{inner} - 2r}{2} \qquad \text{[Eqn. 5]}$$

Where D_{inner} is the inside diameter of the ring-shaped sample, and r is equal to 0.38mm (the radius of the pin holding the sample in place throughout the tensile test).

The calculated gauge length was then compared to the actual gauge length used during the tensile test. The preload which represented the closest value for gauge length to that of the calculated gauge length was used for all subsequent tensile tests using both ring shaped and dogbone shaped samples. It was found that a preload of 0.01 N resulted in high strains which were due to the straightening out of the tissues rather than the inherent mechanical properties. An increase in preload resulted in a general increase in stiffness of the material. A preload of 0.05 N was found to represent most accurately the deformation of the tissue. For this reason, a preload of 0.05 N was used for all subsequent testing.

3.2.1.3 Investigating RCA versus LCA

An investigation was carried out to ascertain whether any significant differences in mechanical properties existed between the right and left main coronary arteries. To carry out this investigation, seven right coronary arteries and seven left coronary arteries were carefully excised from porcine hearts. One dogbone-shaped sample and one ring shaped sample were cut, as described in section 3.2.1.1 above, from each coronary artery and the thickness of each sample measured prior to tensile testing.

3.2.1.4 Investigating Anisotropy

To investigate anisotropy, which is the ability of the tissue to behave differently in different directions, fourteen porcine coronary arteries were excised. One dogbone-shaped sample and one ring shaped sample were cut from each of the first seven coronary arteries, as described in section 3.2.1.1 above. For the remaining seven coronary arteries, seven dogbone-shaped samples were cut along the length of the arteries and five dogbone-shaped samples were cut along the circumference of the artery. As the length of material is more constrained in the

circumferential direction, it was only possible to cut five such samples from the seven coronary arteries.

3.2.1.5 Sylgard® Preparation & Testing

Sylgard® 184 silicone elastomer, base and curing agent, was chosen to construct the mock arteries which were used in the in-vitro stent expansion simulations. This elastomeric material was supplied as a two part kit comprised of two liquid components, namely the base and curing agent. This material was chosen mainly due to its variable elastic properties whereby the stiffness of the material can be increased by increasing the concentration of the curing agent. The elastomeric material was also chosen due to its transparency which enabled the visualisation of the stent inside the mock artery during stent deployment.

As Sylgard® 184 is an isotropic material it was only necessary to test this material in one direction. For this reason dogbone-shaped samples alone were tensile tested. A lengthy process was carried out to create the dogbone-shaped Sylgard® samples for testing such that a suitable match in mechanical properties to that of porcine coronary arteries could be identified. Four different batches of Sylgard® were mixed whereby the ratio of base to curing agent was altered for each batch. Four different weight ratios of base to curing agent were tested as follows: 10:1, 11:1, 14:1 and 16:1. To begin making the Sylgard® material, the liquid base component was carefully poured into a white beaker and weighed. A pipette was then used to add the exact amount of curing agent to make up the desired ratio.

Once the correct amount of curing agent was applied to the base the two liquid components were mixed thoroughly with a smooth action to minimise the introduction of excess air. To remove all air bubbles from the mixture, the beaker containing the mix was placed in a Nalgene vacuum desiccator which was attached to a vacuum pump, see Figure 3.6.

Figure 3.6: Nalgene dessicator attached to vacuum pump

Once all of the bubbles were removed from the mixture, the liquid was carefully poured into custom-made 80 mm x 150 mm stainless steel moulds which were 2 mm deep. A top plate was securely fastened onto the lower mould containing the mix, and the mould was placed in an oven at 100°C for 1 hour to allow the mixture to cure. On removal of the mould from the oven, the mould was allowed sufficient time to cool down before the 2 mm thick Sylgard® sheet was removed from the mould. Dogbone-shaped samples were cut from the sheet of elastomer using the same cutting device as was used to cut the porcine coronary arteries. Three dogbone-shaped samples were cut and tested for each of the four different ratios of Sylgard® elastomeric material, i.e. 10:1, 11:1, 14:1 and 16:1 respectively. A strain rate of 60% min^{-1} was used to test all Sylgard® samples with a preload of 0.05 N to represent the test conditions used to tensile test the porcine coronary tissue samples. In such a way, the resulting stress strain curves could be compared to those of the porcine coronary arteries.

3.3 Construction of Sylgard® Mock Arteries

The Sylgard® material was prepared as described in section 3.2.1.5 above. As previously mentioned the correct amounts of base to curing agent were mixed to achieve a 10:1 ratio. Following stirring of the two liquid components the beaker containing the mix was placed in a vacuum desiccator until all air bubbles were removed. A rig was designed to construct mock arteries using compliant Sylgard® 184 elastomer with a base to curing agent ratio of 10:1. The construction rig was designed such that realistic coronary artery geometries could

be manufactured consistently and with no artefacts or damage to the Sylgard® tubes. The mock artery mould was constructed by inserting a stainless steel mandrel inside a Teflon (TFE) shell such that both cylinders were concentric. The Sylgard® mix was then drawn into the mould and cured. Following curing, the TFE shell was peeled away and the Sylgard® tube was removed from the mandrel. The mock arteries were developed as straight cylindrical vessels with an inner lumen diameter of 3 mm and a thickness of 0.5 mm, thus representing typical idealised porcine coronary artery geometry.

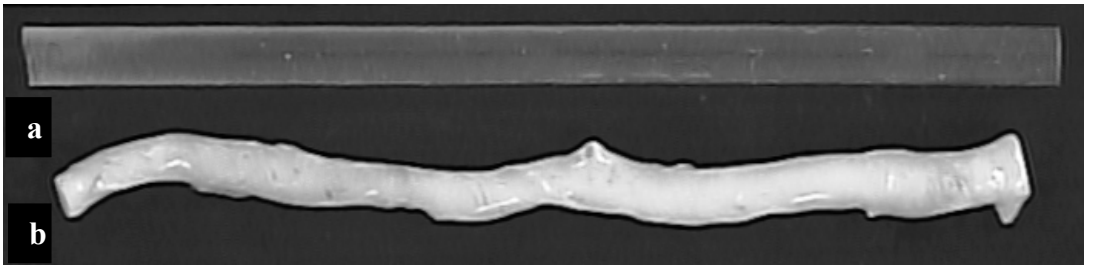

Figure 3.7: (a) Sylgard® tube and (b) Porcine coronary artery

The construction rig consisted of two stainless steel end spacers within which a polished stainless steel inner mandrel was placed. The stainless steel mandrel measured 3 mm in diameter and 120 mm in length. Both end spacers were tapered and slots were cut on the smallest ends to allow for transfer of fluid through these predefined channels at either end of the mandrel. To manufacture the TFE shells, TFE shrink tubing was heated onto a 4 mm diameter polished stainless steel mandrel using a heat gun at 150°C. This 4 mm TFE cylindrical tubing was used to form the outer shell of the mould and was placed over the end spacers as shown in Figure 3.9 below. A non stick coating was sprayed onto the stainless steel mandrel prior to heat shrinking the TFE tubing. This made it easier to release the TFE heat shrink tubing once it had moulded to the diameter of the mandrel.

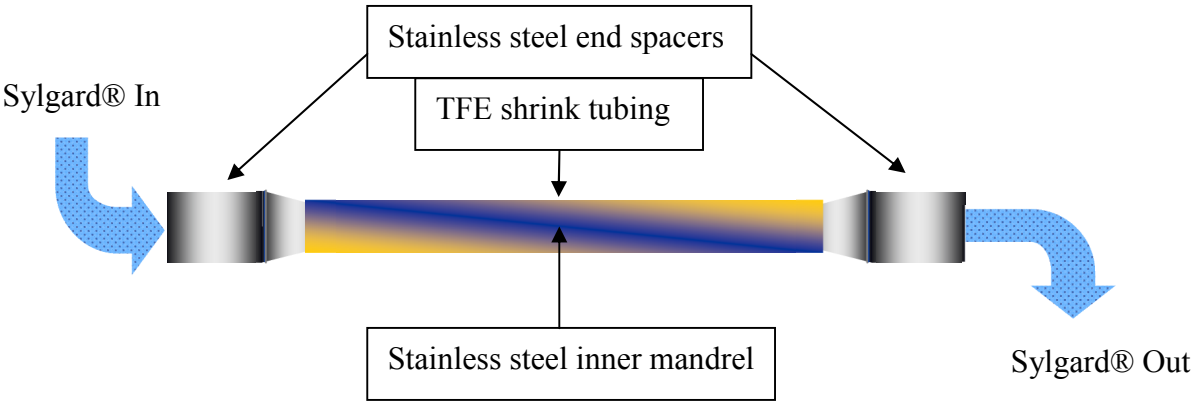

Figure 3.8: Diagram of assembled mock artery construction rig.

Once the stainless steel inner mandrel and TFE outer tubing were concentrically placed, both end spacers were locked onto a base plate such that the rig was securely fastened. Rigid plastic tubing was connected to the extreme ends of the end spacers, whereby the rightmost tubing was attached to a 760 mmHg vacuum pump and the leftmost tubing was placed in the reservoir of prepared Sylgard® liquid. In such a way the Sylgard® was drawn into the mould between the 3 mm inner mandrel and the outer TFE tubing which had an inner diameter of 4 mm. An air valve was fixed onto the tubing connecting the rig to the vacuum pump such that the vacuum pressure could be minimised to reduce the effect of air intrusion. The pressure was also adjusted to maintain a constant flow of elastomer into the mould. When the mould was full an aluminium cover was fastened on top of the base plate to ensure that the concentricity of the inner mandrel and the outer TFE tubing was maintained, see Figure 3.9.

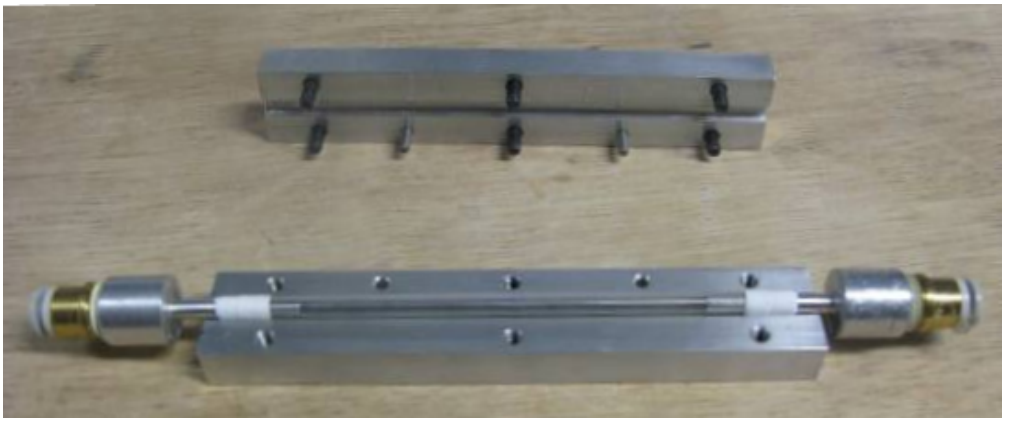

Figure 3.9: Sylgard® filled tube ready for curing.

The rig was then placed vertically in an oven at 150°C for 1 hour to allow the Sylgard® to cure. Once removed from the oven, the rig was left overnight in an upright position, to ensure the Sylgard® was fully cured and cooled before removing the mould. To remove the Sylgard® compliant tube from the mould, the end spacers were first removed and the TFE outer shell was gently peeled off. Acetone was then injected between the Sylgard® tube and the inner mandrel to allow for ease of removal.

3.4 Numerical Modelling of the Driver Stent Geometry

The Driver stent (Medtronic AVE) has a unique modular design which consists of a number of sinusoidal rings spanning the length of the stent, each ring containing 10 crowns and measuring 1 mm in length. The stent design used in the simulations was based on the 3.5 mm Driver stent which had a total length of 9 mm thus consisting of 9 rings, see Figure 3.10. Each sinusoidal ring is connected to the adjacent ring(s) at two evenly spaced weld points which are offset by 180 degrees around the circumference. Each set of weld points are further offset by 90 degrees to the subsequent adjacent set. For this reason it was only necessary to model a quarter of the Driver stent for the numerical simulations. The Driver stent has an ultra thin strut thickness of 0.09 mm and has a circular cross-sectional area measuring 0.006 mm^2.

In order to accurately model the stent geometry, images of the Medtronic Driver stent in its crimped and expanded positions were obtained using a scanning electron microscope (SEM). The images of the stent in its crimped position were subsequently digitised using Engauge Digitizer software in order to define accurately its geometric coordinates (see Figure 3.11 below).

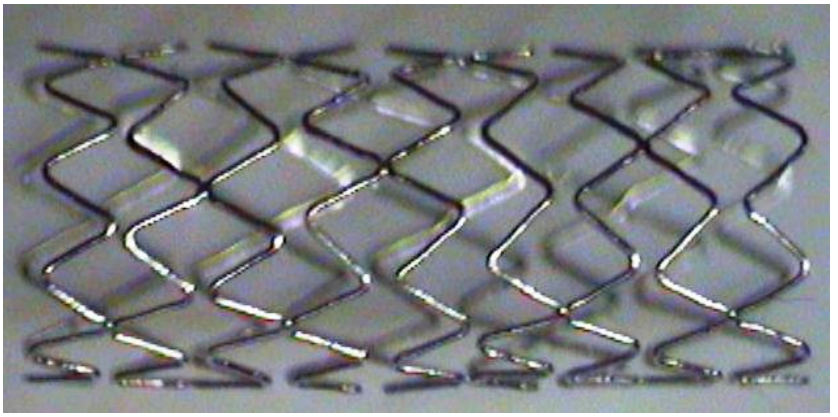

Figure 3.10: 3.5 mm (expanded inner diameter) x 9 mm (length) Driver stent.

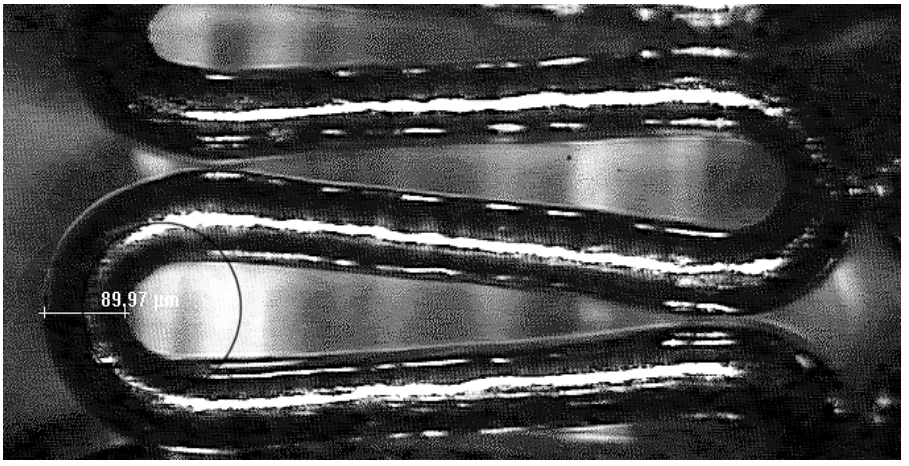

Figure 3.11: SEM image of section of Driver stent strut. A number of these images were taken and used to identify the geometry of the stent.

The coordinates obtained from the SEM images were then used to model the stent geometry in ANSYS with a strut thickness of 0.09 mm and an inner diameter of 0.91 mm. The stent was modelled with 10 sinusoidal rings in length, each ring measuring 1 mm in length, see Figure 3.12 below. The weld points joining the rings together were represented by a common node whereby one node from each strut at the weld points were merged to create one single node. The outer diameter of the stent in its initial unexpanded, crimped condition was 1.09 mm.

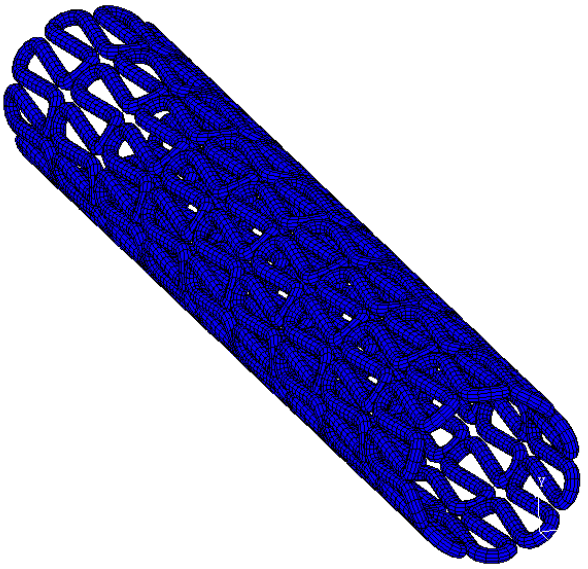

Figure 3.12: Discretised numerical model of unexpanded Driver stent

The stent geometry was initially modelled in the three-dimensional Cartesian coordinate system, representing the stent in an opened-out planar configuration. To generate the planar geometry of the stent, line profiles that represented the skeleton of the stent were created and a circular area measuring 0.09 mm in diameter was subsequently extruded along the line profiles to generate the stent volume.

The volumes of the Driver stent were then discretised using eight-noded isoparametric, three dimensional brick elements (type 7 elements in Marc Mentat). A mesh convergence study was carried out which specified an optimum mesh density of 21 elements through the thickness, resulting in a total of 19,700 elements with 26,252 corresponding nodes, see Appendix A. The integrity of the elements was checked for their shape to ensure that no distorted elements were generated. Adaptive meshing was used to ensure minimal penetration occurred when the stent came into contact with the artery by subdividing the elements on the artery which were contacted by the stent. This adaptive meshing and subsequent mesh refinement results in an improvement in the accuracy of the solution as well as reducing the computational time that would be required if the entire artery were to have a refined mesh.

The nodal coordinates of the meshed model were transferred from a Cartesian coordinate system into a cylindrical coordinate system, using a procedure reported by Lally *et al*. [39], whereby the planar configuration was wrapped to represent the cylindrical structure of the stents. The elements, nodes and their connectivity were then transferred into the finite element code MSC Marc Mentat and large deformation analyses were solved to simulate the expansion of the stent. Although ANSYS was used to model the stents' geometries, it was found that it was not suitable for solving the analyses which included contact between the stent and artery and the use of hyperelastic material models to define the mock arterial wall.

Three case studies were carried out to investigate the accuracy of the numerical Driver stent expansion in its free and loaded states, when compared to the in-vitro experimental stent expansion. In the first two case studies the stent performance was evaluated both numerically and experimentally, in terms of radial recoil, longitudinal recoil, foreshortening, and dogboning for free expansion and stent expansion inside a mock artery. The measured geometries and calculated parameters of interest during these analyses are summarised in Table 3.1. These values were taken from the actual and numerical stent structures when the stents were in their unexpanded, loaded and unloaded configurations.

Measured Outputs (mm)		
Stent before expansion		
R_{orig}	Original radius of the stent before expansion	
L_{orig}	Original length of the stent before expansion	
Stent after loading		
$R_{load\ proximal}$	Radius of stent at the proximal end of the stent just after balloon expansion	
$R_{load\ central}$	Radius of stent at the centre of the stent just after balloon expansion	
$R_{load\ distal}$	Radius of stent at the distal end of the stent just after balloon expansion	
L_{load}	Length of the stent at the end of loading when the balloon is fully pressurised	
Stent after unloading		
$R_{unload\ proximal}$	Radius of stent at the proximal end of the stent just after balloon deflation	
$R_{unload\ central}$	Radius of stent at the centre of the stent just after balloon deflation	
$R_{unload\ distal}$	Radius of stent at the distal end of the stent just after balloon deflation	
L_{unload}	Length of the stent at the end of unloading when the balloon is fully deflated	
Calculated Parameters (mm)		
Radial recoil	$\frac{R_{load\ central} - R_{unload\ central}}{R_{load\ central}}$	Radial recoil is expressed in terms of the relative reduction in the radius of the stent following deflation of the balloon.
Longitudinal recoil	$\frac{L_{load} - L_{unload}}{L_{load}}$	Radial recoil is expressed in terms of the relative reduction in the length of the stent following deflation of the balloon.
Foreshortening	$\frac{L_{orig} - L_{load}}{L_{orig}}$	Foreshortening is expressed in terms of the relative reduction in the length of the stent following inflation of the balloon to the required diameter. This can sometimes be expressed as a negative value whereby the stent actually lengthens.
Dogboning	$\frac{R_{load\ distal} - R_{load\ central}}{R_{load\ distal}}$	Dogboning is the flaring out of the ends of the stents upon inflation and is expressed in terms of the relative difference between the distal radius of the stent and the central radius of the stent.

Table 3.1: Description of the geometric data and calculated parameters taken during the numerical and experimental expansion of the Driver stents.

In both the first and second case studies the resulting radial displacement distribution, von Mises stress, σ, and total equivalent plastic strain, $\dot{\varepsilon}_{eqv}$, were evaluated for the expanded stent structures. The von Mises stress is defined using the following equation:

$$\sigma = \frac{[(\sigma_1 - \sigma_2)^2 + (\sigma_2 - \sigma_3)^2 + (\sigma_3 - \sigma_1)^2]^{1/2}}{\sqrt{2}} \qquad \text{[Eqn. 6]}$$

where, $\sigma_1, \sigma_2, \sigma_3$ are the principal stresses.

The total equivalent plastic strain is defined using the following equation:

$$\dot{\varepsilon}_{eqv} = \int_0^t \sqrt{\frac{2}{3}\dot{\varepsilon}^{pl} : \dot{\varepsilon}^{pl}}\, dt \qquad \text{[Eqn. 7]}$$

where, $\dot{\varepsilon}^{pl}$ is the plastic strain rate tensor.

In the second case study, which involved the stent expansion inside a mock coronary artery, a further validation was also carried out using strain analysis, which is described in detail in section 3.6.2 below. The final case study involved a purely numerical investigation into the effect of varying the elastic properties of mock arteries on the subsequent stress induced in the artery.

3.5 Case Study 1:

Assessment of Free Expansion of the Driver Stent

3.5.1 Numerical Expansion

In this analysis, the effect of increasing the surface area to which the pressure is applied was investigated such that the most realistic loading condition to simulate a balloon expansion could be identified. A uniform pressure of 1925 kPa was applied to the two inner element faces along the length of the stent, representing the stent with the smaller amount of selected pressure faces, i.e. $Driver_{spf}$ see Figure 3.13 (a). A uniform pressure of 1095 kPa was applied to the four inner element faces along the length of the stent, representing $Driver_{lpf}$ as a larger number of faces have been selected, see Figure 3.13 (b). In both cases the stent was loaded such that it achieved an inner diameter of 3.5 mm upon loading, hence the need for a larger pressure to expand $Driver_{spf}$. All design aspects of the two stents used in this analysis were the same, the only difference between the two models being the area onto which the pressure was applied.

(a) Small Pressure Faces ($Driver_{spf}$)

Pressure = 1925 kPa

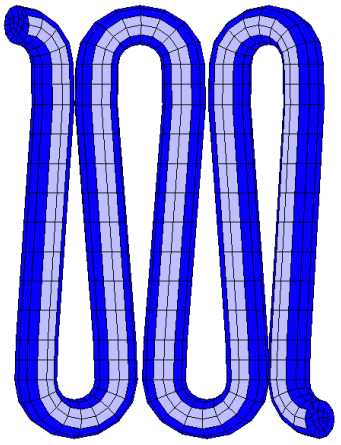

(b) Large Pressure Faces ($Driver_{lpf)}$

Pressure = 1095 kPa

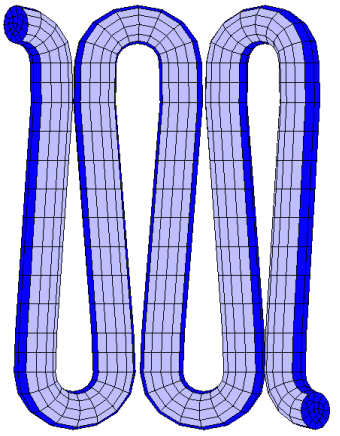

Figure 3.13: Simulation of balloon expansion on (a) small pressure faces versus (b) large pressure faces.

The expansion pressure was ramped up in 100 time increments resulting in a time step of 0.01 and was subsequently ramped down in 50 time increments and therefore half the time it took to load the stent. Too small of a time step would have resulted in too much pressure being applied in one increment over time and therefore would have led to deformation of the elements and non convergence of the simulation.

The effect of constraining the weld points from moving in the axial direction was also investigated to determine the most appropriate and realistic boundary conditions to simulate a balloon expansion. In the first simulation, only the central weld point on the stent was constrained from moving in the axial direction of the stent, thus representing $Driver_{unfixed.}$ In the second simulation, all weld points on the stent were constrained in the axial direction of the stent, thus representing $Driver_{fixed.}$ These axial constraints on the weld points were investigated as the presence of a balloon during an actual stent expansion may act as a physical constraint to these areas by means of frictional forces between the balloon and the stent. See Figure 3.14 below for indication of weld point locations (red arrows), and constrained nodes for both simulations. Both stents were freely expanded by applying a uniform pressure of 1095 kPa to the inner surface of the stent such that they achieved an inner diameter of approximately 3.5 mm each.

(a) $Driver_{unfixed}$

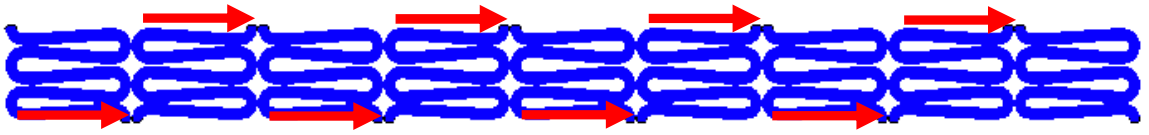

(b) $Driver_{fixed}$

Figure 3.14: Red arrows indicate weld points where stent was constrained to move in its axial direction for (a) $Driver_{unfixed}$ and (b) $Driver_{fixed}$.

In all stent simulations carried out as part of this case study cyclic symmetry boundary conditions were imposed on the nodes lying on the circumferential plane of symmetry of the stent. One node at the distal end of the stent was constrained to move in the circumferential direction to prevent any rigid body rotations. Both ends of the stent were free from any other constraints.

3.5.2 Experimental Expansion

Balloon expandable Driver stents measuring an inner diameter of 3.5 mm (upon expansion) and 9 mm in length were obtained from Medtronic, Parkmore Business Park, Galway. As part of this case study, six Driver stents were expanded using a handheld pressure pump which was attached to the proximal end of the stent delivery system. The stents were expanded using a balloon inflation pressure of 10 atm which corresponds to 1013.25 kPa. This resulted in an expanded inner diameter of approximately 3.5 mm as specified in the instructions for use. The distal end of the stent delivery system was placed in a holding fixture which held the stent in place during expansion and deflation. Once the stent was in place and the pressure pump attached, the balloon and subsequently the stent were expanded. A video extensometer was positioned just above the stent and images were captured every tenth of a second throughout the expansion and deflation process. Images of the stents in the unexpanded, and expanded orientations were selected for image analysis, see Figures 3.15 (a, b, and c) below.

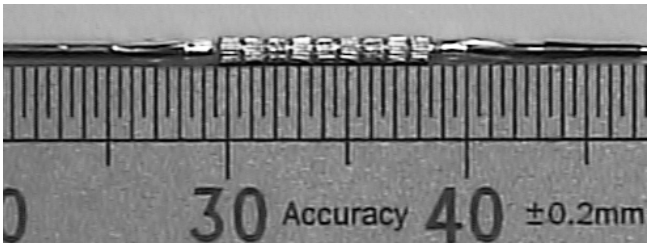

Figure 3.15(a):
Stent in unexpanded state

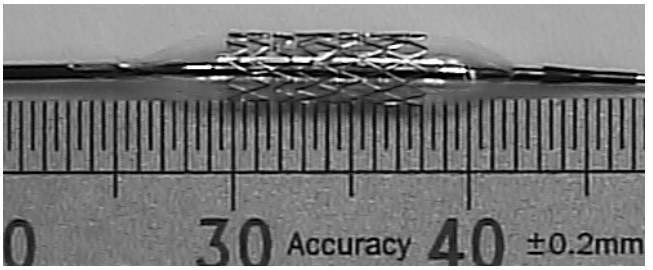

Figure 3.15(b):
Fully expanded stent with balloon fully expanded

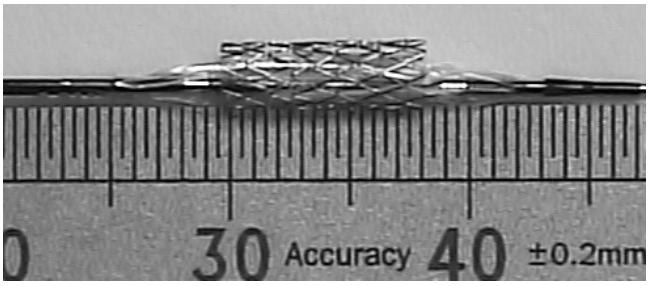

Figure 3.15(c):
Fully expanded stent with balloon fully deflated

The images were digitised using Engauge Digitizer software and the outer diameter of the stents at the proximal, central and distal locations were measured and the average calculated. The length of each stent was also measured at each of the three stages such that the 4 stent parameters, as described in Table 3.1, could be calculated.

3.6 Case Study 2:

Assessment of Driver Stent Expansion inside a Sylgard® Mock Artery

In this case study the Driver stent was expanded inside an idealised cylindrical vessel, both numerically and experimentally such that the most accurate numerical methods could be validated experimentally.

3.6.1 Numerical Expansion

Two separate analyses were carried out in this case study. In the first analysis, four numerical simulations were run whereby the mock artery was loaded by the Driver stent and the four stent parameters (foreshortening, radial and longitudinal recoil, and dogboning) were measured at unloading, when the pressure was fully removed. Two methods of numerical stent expansion were investigated:

1. 'Original' expansion, whereby the stent was expanded into the mock vessel and subsequently unloaded and

2. ‘Alternative’ expansion, which involved the initial free expansion of the stent and the subsequent unloading of an expanded vessel onto the expanded stent.

Although the ‘alternative’ expansion method does not represent a realistic stent expansion, this method was investigated to see whether certain stent parameters such as recoil and dogboning could be accurately determined using more simplified and less time consuming methods. As stent recoil and dogboning are only influenced by the unloading of the artery onto the stent it may be necessary to only simulate this interaction. In both methods the stent was expanded such that it achieved an internal diameter of 3.5 mm. In both methods of stent deployment, the pressure was applied to the inner surface of the stent as a uniform, linearly increasing pressure. The effect of constraining the weld points to prevent axial movement was also investigated in both methods of stent expansion. The pressures required to expand the stents using the original and alternative methods were 1600 kPa and 1095 kPa respectively. In the second analysis, to further validate the numerical methods used, the resulting strains induced in the mock artery for the most valid numerical simulation were compared to those of the actual strains recorded in the Sylgard® vessel.

Unlike the full numerical models used for the free expansion validation, only five repeating rings of the Driver stent were modelled for each simulation in this case study. This was performed to reduce computational time as the models also included a Sylgard® vessel which consisted of 80,000 elements and 105,191 nodes for the half model alone. Measures for longitudinal recoil and foreshortening, assuming the full length of the stent, i.e. nine links were recorded.

The mock coronary artery was modelled as a straight cylindrical vessel with an internal diameter of 3 mm, a uniform thickness of 0.5 mm and an overall length of 5.5 mm. Material properties obtained from the uniaxial tensile testing of Sylgard® elastomer with a 10:1 ratio of base to curing agent were assigned to the straight vessel. Ten elements were assigned through the thickness resulting in a total number of 80,000 elements for the artery, see Figure 3.16. Cyclic symmetry

boundary conditions were imposed on the circumferential plane of symmetry of both the stent and the mock artery. The nodes at the extreme ends of the vessel were constrained to move in the axial direction thus representing the longitudinal tethering using zero axial displacement conditions and the stent was constrained to prevent rigid body rotations. Frictionless contact was assigned between the stent and the artery. Adaptive meshing was also used to ensure minimal penetration occurred as the stent came into contact with the mock artery. To do so, local mesh adaptivity was assigned to the elements on the inner surface of the artery where the stent came into contact with the artery. As a result, these associated elements were subdivided by two in all three coordinate directions resulting in a substantial refinement of the mesh and hence an improvement in the accuracy of the solution.

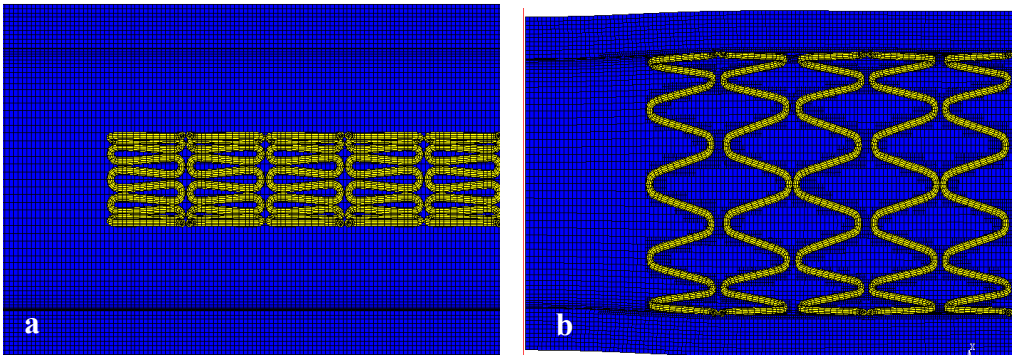

Figure 3.16: Discretised stent and mock artery in (a) unexpanded and (b) expanded positions.

3.6.2 Experimental Expansion

Sylgard® elastomeric mock arteries were constructed (as described in Section 3.3) such that they had an inner diameter of 3 mm and a uniform thickness of 0.5 mm thus representing the mock artery geometries created in the numerical models. The mock arteries were anchored at both ends to stainless steel cylindrical fixtures which could be displaced in the axial direction. The fixtures were tapered to a minimum diameter of 3 mm thus enabling the mock artery to be fixed securely at both ends. Once the mock artery was in place, a Driver stent was inserted through the centre of the cylindrical tube until the stent was positioned in the middle of the

tube. The transparent nature of the Sylgard® tubes enabled the visualisation of the stent inside the tubes. Once placed the stents were expanded using a balloon inflation pressure of 10 atm. A video extensometer was once again positioned just above the stent and images were captured every tenth of a second throughout the expansion and deflation process. Images of the stents in the unexpanded, and expanded configurations were selected for image analysis, see Figures 3.17 (a, b, and c) below.

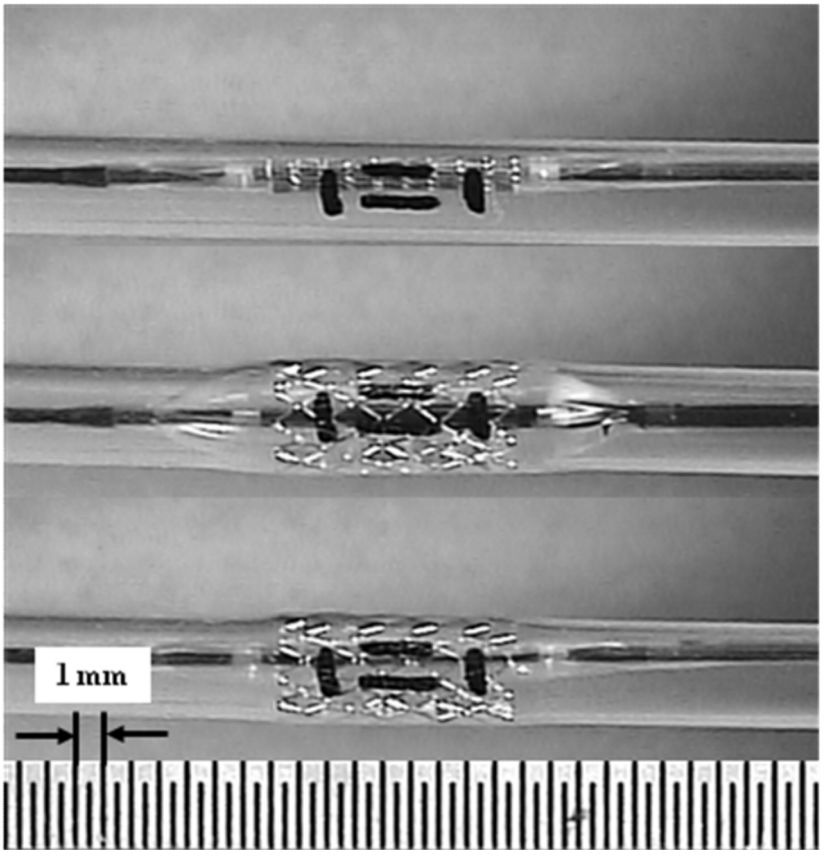

Figure 3.17(a): Stent in Sylgard® in unexpanded state

Figure 3.17(b): Stent in Sylgard® in fully loaded state

Figure 3.17(c): Stent in Sylgard® in fully unloaded state

The images were digitised using Engauge Digitizer software and the outer diameter of the stents at the proximal, central and distal locations were recorded for each stent such that an average could be calculated. The length of each stent was measured at each of the three stages such that the 4 stent parameters, as described in Table 3.1, could be calculated.

Further to this experimental investigation, the strains induced in the mock artery wall during stent expansion were also examined. To do so, four black marks were placed on the Sylgard® tube using a rubber stamp and indelible ink, as identified in Figure 3.17 above. The marks were placed such that they were in the top plane of view and were all visible throughout the stent expansion and deployment. The axial and transverse movement of these markers were captured using the video extensometer and these images were stored every tenth of a second during stent deployment, however, only every hundredth image was analysed for measurements as the movement of the markers was so small. Three separate stent expansions were investigated, and the mean axial and transverse strains recorded.

As the measurements recorded in the transverse direction are taken from a curved surface, the length of the arc, i.e. the actual distance between the transverse markers, was calculated and the subsequent strains recorded over time. The length of the arc was calculated using the following equation:

$$L = r\theta \qquad \text{[Eqn. 8]}$$

where L is the length of the arc, r is the radius of the Sylgard® tube and θ is the projected angle between the two transverse marks. This angle was found using the following equation:

$$\text{Cos}\,\theta = \frac{b^2 + c^2 - a^2}{2\,b\,c} \qquad \text{[Eqn. 9]}$$

where length a is the distance between the two transverse marks as measured from the image, and lengths b and c are both the radius of the Sylgard® tube.

For the numerical model, further post processing was carried out whereby the nodes placed at the same locations as the markers on the Sylgard® tubes were identified and the movement of these nodes tracked throughout stent deployment. The strains were then measured in the axial and transverse directions again at unloading of the stent and the values compared to the experimental results.

3.7 Material Properties

The Driver stent is composed of MP35N cobalt chromium alloy, which is stronger than stainless steel, making it possible to create a stent with thinner struts without compromising the radial strength, see Figure 3.18 below which illustrates the higher tensile strength of cobalt alloy in comparison to 316L stainless steel. The cobalt chromium alloy MP35N material behaviour was described using an elasto-plastic material model whereby the linear elasticity was defined using values for MP35N cobalt chromium alloy which has a young's modulus of 232 GPa and Poisson's ratio of 0.32 [60]. A piecewise linear function was used to represent the non-linear plasticity of the material through a von Mises plasticity model with isotropic hardening.

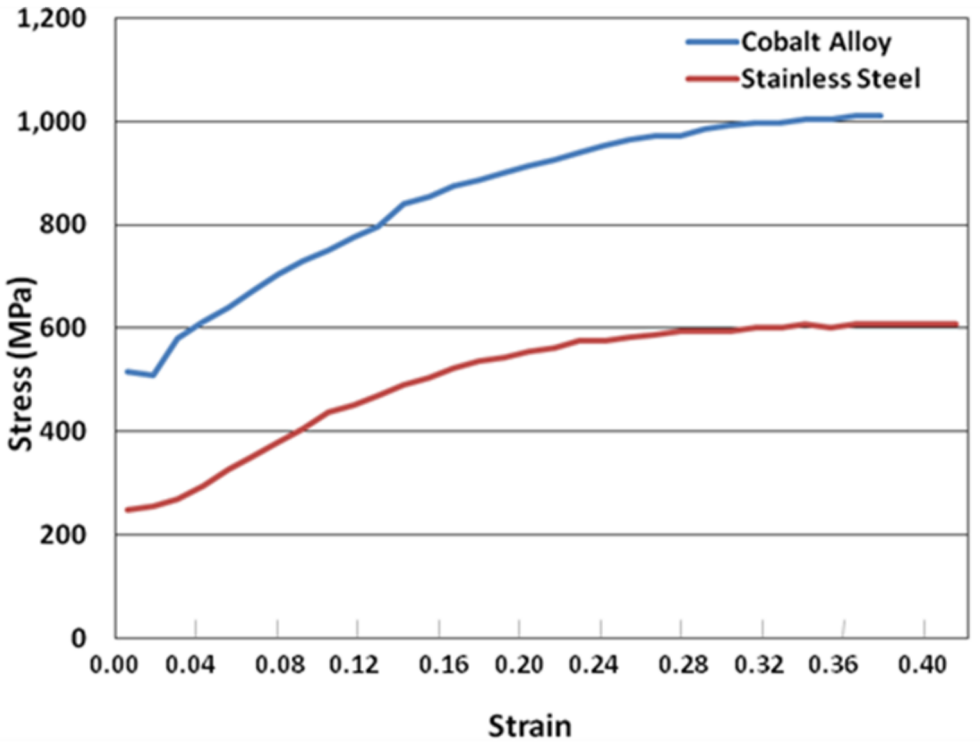

Figure 3.18: Plot of stress-strain curves for the Driver stent cobalt alloy and 316L stainless steel [adapted from Medtronic literature, 2004].

As the Sylgard® mock artery material is isotropic in nature, an isotropic constitutive model was used which included the main characteristics of both

arterial and Sylgard® material such as its non-linear stress stiffening behavior and its incompressibility. In such a way, the results obtained from the numerical models, in terms of stent behavior, could be directly compared to the experimental results. The Sylgard® mock artery material was defined by a second order Mooney-Rivlin hyperelastic constitutive equation. This was found to adequately represent the non-linear stress-strain relationship of the 10:1 Sylgard® mock arteries. Hyperelastic materials can undergo large recoverable (elastic) deformations. The YEOH hyperelastic constitutive model was used to model the 10:1 ratio of Sylgard® material is given by the following equation:

$$W = 248.306\,(I_1 - 3) - 50.3066\,(I_2 - 3) + 13.5744\,(I_1 - 3)^2 \quad \text{(kPa)} \quad \text{[Eqn. 10]}$$

where W is the strain energy density function and I_1 and I_2 are the first and second strain invariants of the elastic strain. This second order hyperelastic model is suitable for modelling an incompressible, isotropic, elastic material such as Sylgard®. The hyperelastic constitutive equation was determined by fitting to the stress-strain data available from the uniaxial tension tests carried out on the 10:1 ratio of Sylgard® material (as described in section 3.2.1.6).

The Marc/Mentat non-linear regression routine was used to obtain the hyperelastic constitutive model that best fit the uniaxial stress-strain data for the chosen Sylgard® material. The most applicable model, according to the least error given by all test models, was chosen and was based on absolute error defined as follows:

$$\text{Absolute error} = \sum_i [\text{data measured(i)} - \text{data calculated(i)}]^2 \quad \text{[Eqn. 11]}$$

The data fit was subsequently checked for positive definiteness. The YEOH 2nd order constitutive model was found to best fit the Sylgard® data as can be seen by the overlapping stress-strain curves in Figure 3.19. This was found to be the best fit in comparison to all other models, yielding the lowest associated error of 0.083453. As a result of this low error, the YEOH data set is almost an exact fit to

that of the experimental data set describing the uniaxial stress strain behaviour of the Sylgard® material.

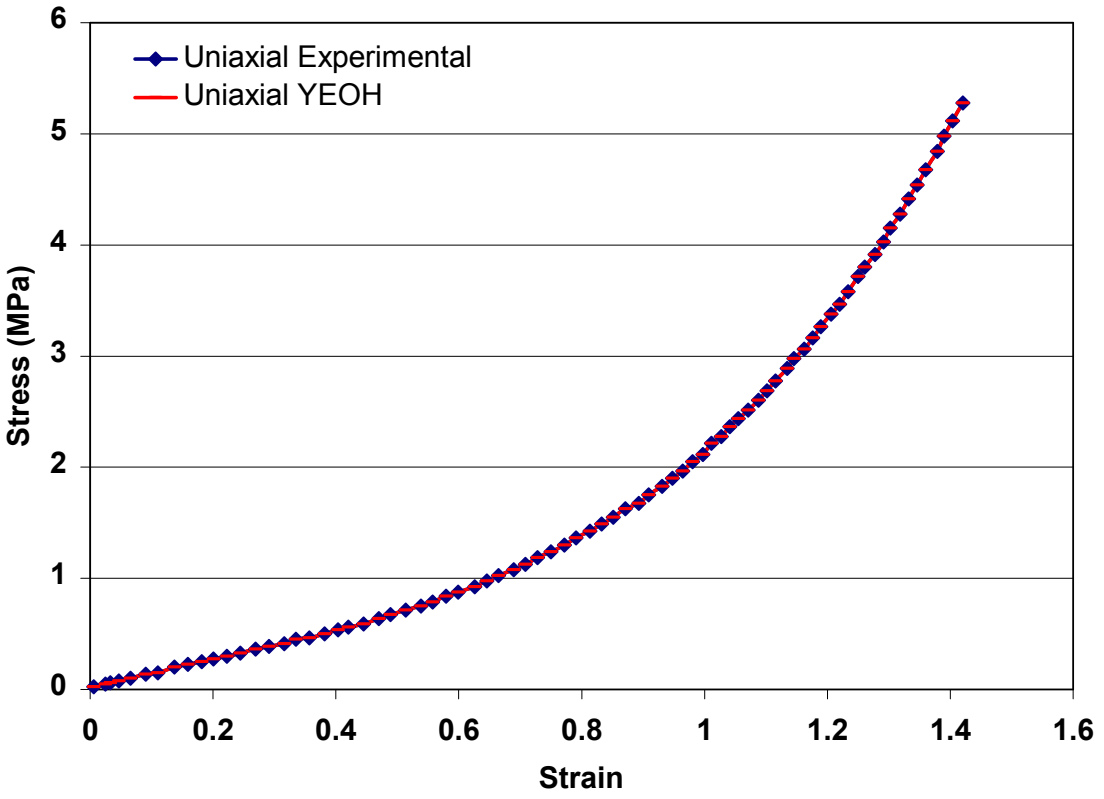

Figure 3.19: Plot of stress-strain uniaxial data for 10:1 Sylgard® material

CHAPTER 4

RESULTS

4.1 Introduction

The following chapter outlines firstly the results obtained for the uniaxial tensile testing of both porcine coronary tissue and various ratios of Sylgard® Elastomer 184, such that a suitable match in porcine coronary mechanical properties was found for the Sylgard®. Following this, a suitable Mooney-Rivlin hyperelastic model was found to represent the elastic behaviour of the chosen Sylgard® material in subsequent numerical models.

Having found a suitable material model to represent the elastic behaviour for porcine coronary tissue, the Driver stent was expanded freely and inside a Sylgard® vessel. Stent expansion was carried out both experimentally and numerically, such that the numerical methods used could be validated. A further case study was carried out to investigate the influence of expanding the stent inside a stiffer vessel on stresses induced in the vessel wall.

4.2 Experimental uniaxial tensile testing

Extensive uniaxial tensile testing was carried out on porcine coronary tissue and various ratios of Sylgard® Elastomer 184 such that a suitable match in mechanical properties was found for Sylgard®. Test samples were taken from the porcine left coronary artery (LAD) and right coronary artery (RCA), the two main arteries in the heart. Due to the inherent anisotropic nature of coronary vessels, the porcine tissue was tested in both the circumferential and longitudinal directions

using dog-bone shaped samples for the longitudinal test samples and both ring and dog-bone shaped samples for the circumferential test samples.

Tensile testing was carried out on four different ratios of Sylgard® material, namely, 16:1, 14:1, 11:1, and 10:1. As Sylgard® is an isotropic material, testing was carried out in only the longitudinal direction using dog-bone shaped samples.

4.2.1 Investigating preload

For the circumferential ring-shaped samples, three different preloads were investigated to ensure the correct preload was being used such that the tissue was always in slight tension at the beginning of each test. As the gauge length for the ring-shaped samples could not be controlled it was important to find a suitable preload to be used for all samples such that the tissue was in slight tension prior to testing, otherwise the strain recorded at the beginning of the test would be representative of the straightening of the material rather than the deformation whereby a strain is applied to the material. The preloads were 0.01 N, 0.05 N, and 0.1 N respectively, see Figure 4.1. A preload of 0.01 N was found to be too low. When comparing the calculated gauge length (see Chapter 3, Section 3.2.1.2 for calculation) to the actual gauge length at this particular preload, it was found that the actual gauge length was lower than that of the calculated gauge length. The high strains associated with this preload are therefore attributable to the straightening out of the tissue between the grips, rather than the deformation. An increase in preload resulted in a general increase in stiffness of the material. A preload of 0.05 N was found to represent most accurately the deformation of the tissue. For this reason, a preload of 0.05 N was used for all subsequent testing.

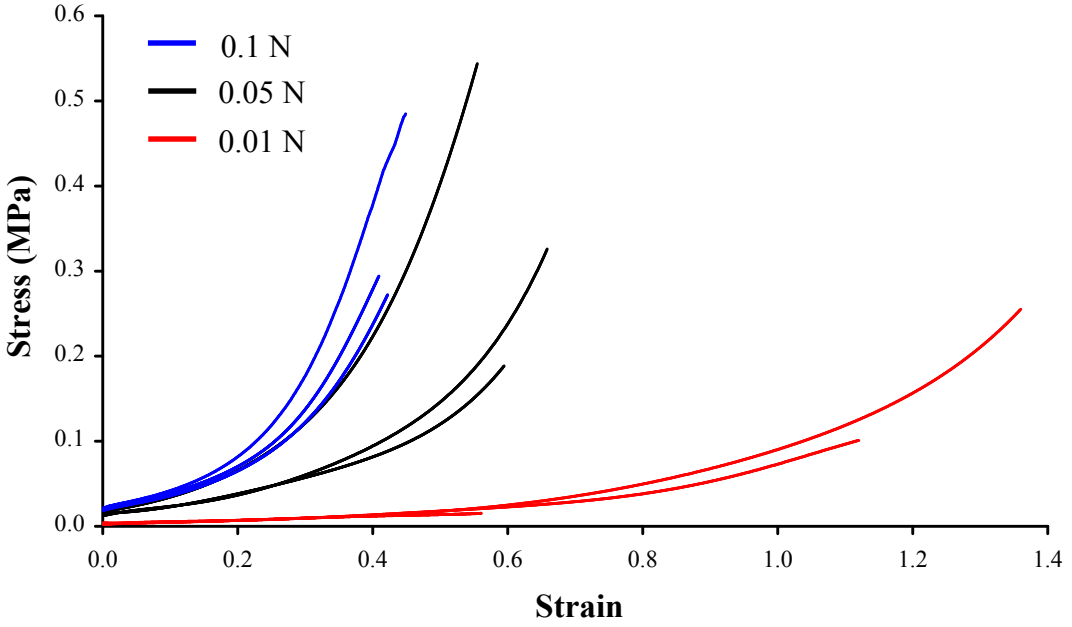

Figure 4.1: Uniaxial stress-strain curves for porcine coronary tissue using preloads of 0.1 N, 0.05 N, and 0.01 N.

4.2.2 Investigating RCA versus LCA

The stress-strain behaviour of the porcine coronary tissue was found to be highly non-linear. It is clear to see from the resulting stress-strain curves in Figure 4.2 that significant variation occurs across both longitudinal and circumferential stress-strain curves. When comparing the RCA to the LCA, it can be seen that there is no significant difference between the stress-strain behaviour and the variation found in both vessels.

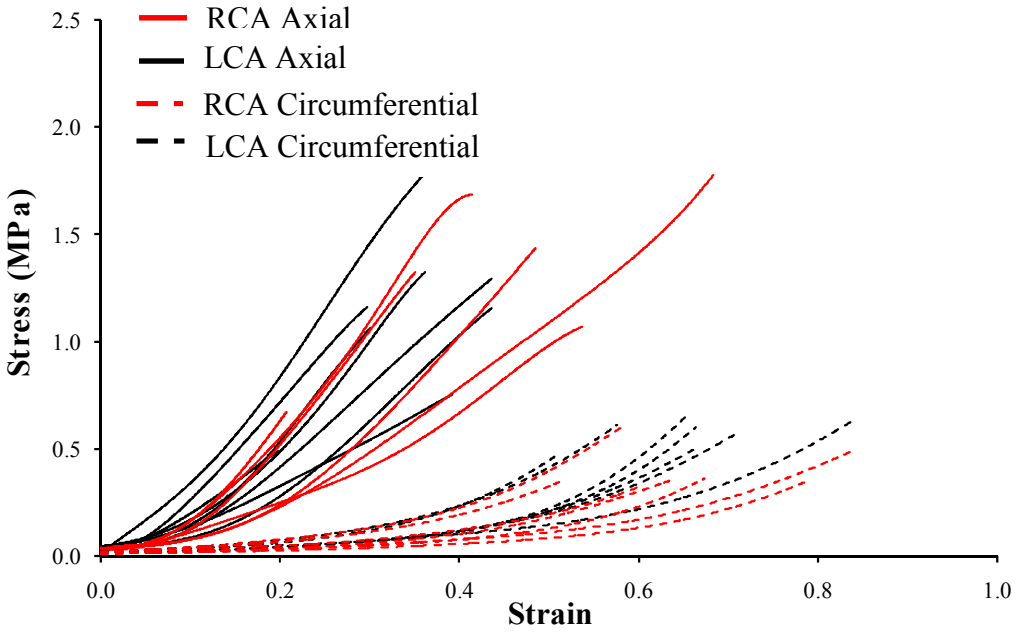

Figure 4.2: Uniaxial stress-strain curves for porcine coronary tissue, comparing the right coronary artery (RCA) to the left coronary artery (LCA).

4.2.3 Investigating Anisotropy

It was noted that the tissue displayed much stiffer behaviour when tested in the longitudinal direction using conventional dogbone-shaped samples than in the circumferential direction. When comparing the response of the tissue when tested in the circumferential direction using conventional ring shaped samples, and longitudinal direction using dog-bone shaped samples, it is clear to see that the tissue displays anisotropic behaviour, see Figure 4.3.

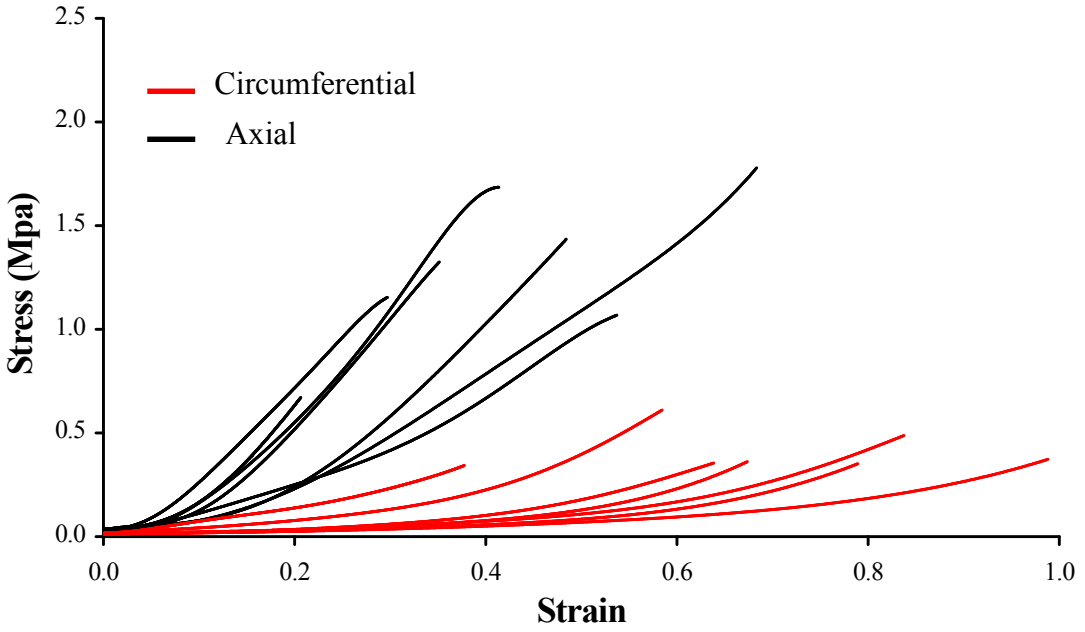

Figure 4.3: Uniaxial stress-strain curves for porcine coronary tissue tested in the circumferential direction using ring shaped samples, and in the axial direction using dog-bone shaped samples.

However, when testing the porcine coronary tissue in the circumferential and longitudinal directions, using dog-bone shaped samples for both, it was found that the tissue exhibited almost isotropic elastic behaviour, as can be seen in Figure 4.4 below. It is common to test ring-shaped samples of arteries in the circumferential direction, whereby the inherent residual stresses are maintained. This stress is defined as the stress that is left in the artery when all external loads are removed. It was thus interesting to see that when these residual stresses were removed, i.e. by cutting open the coronary artery along the length of the artery, the resulting circumferential stress-strain behaviour resembled that of axial stress-strain behaviour.

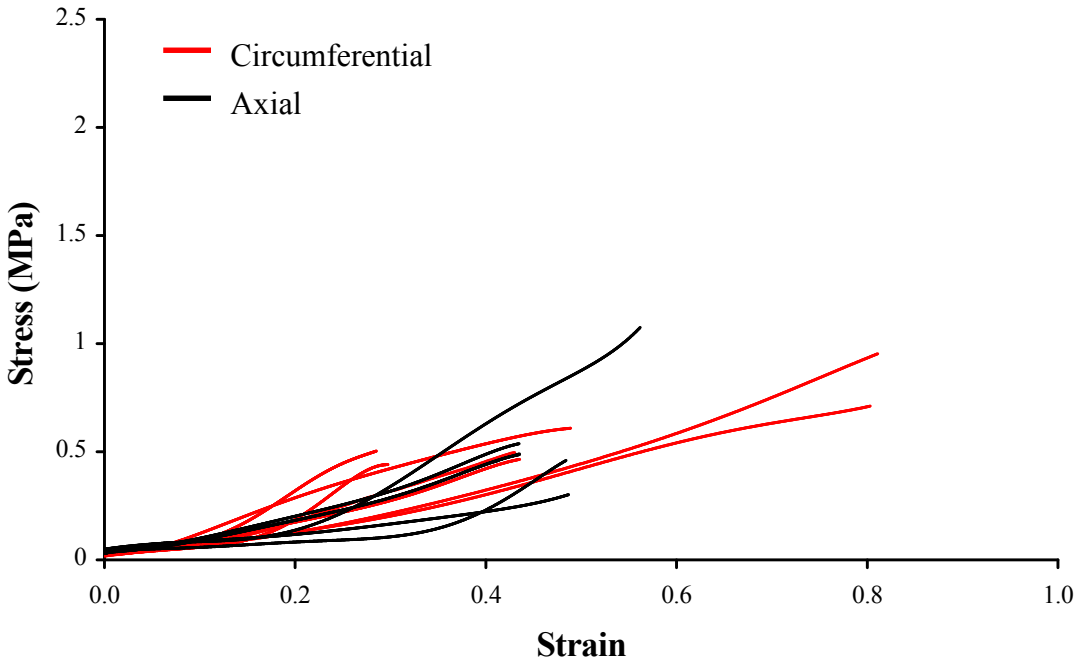

Figure 4.4: Uniaxial stress-strain curves for porcine coronary tissue tested in the circumferential and axial directions using dog-bone shaped samples for both.

4.2.4 Porcine Coronary Arterial Tissue versus Sylgard®

It can clearly be seen from Figure 4.5 below that the Sylgard® material contains variable elastic properties. As the ratio of base to curing agent is increased from a ratio of 10:1 to a ratio of 16:1, the material becomes more compliant and therefore less stiff. When comparing the elastic behaviour of the porcine coronary tissue to that of the four different ratios of Sylgard® material, it is clear to see that both the 10:1 and the 11:1 ratios exhibit mechanical properties within the mid-range of data for both the circumferential and longitudinal porcine stress-strain curves. For this reason the 10:1 ratio of Sylgard® base to curing agent was used to construct the elastomeric mock arteries which were subsequently used to carry out the *in-vitro* stent expansion simulations. An isotropic hyperelastic model based on the Mooney-Rivlin constitutive equation was derived from the test data and used in subsequent numerical models. See Chapter 3 Materials & Methods, Section 3.7 for further details.

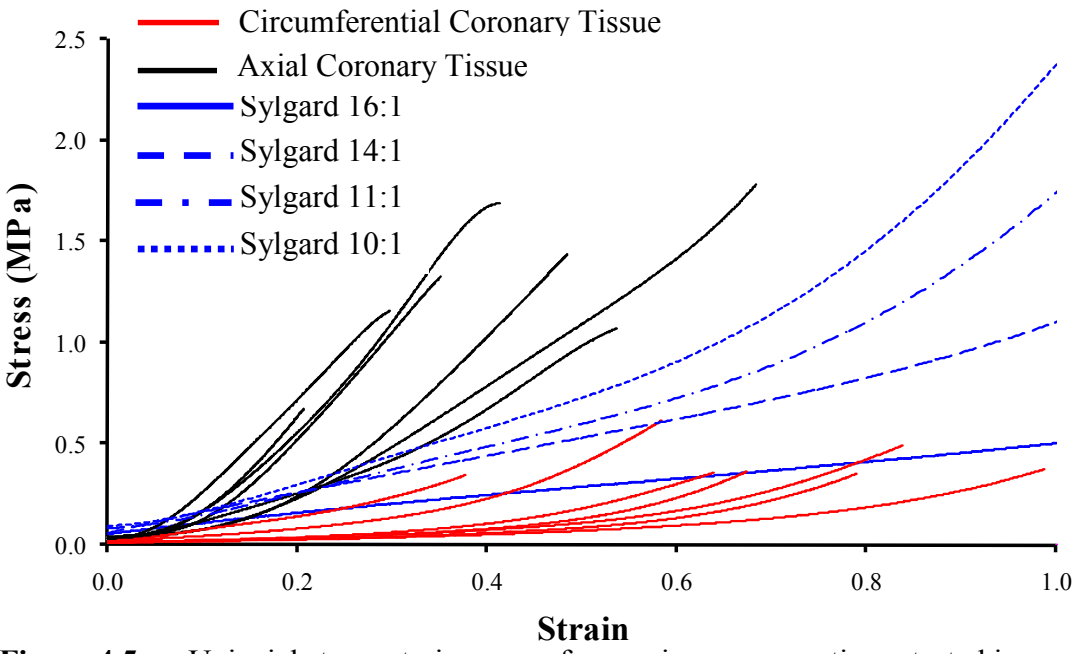

Figure 4.5: Uniaxial stress-strain curves for porcine coronary tissue tested in the circumferential direction using ring shaped samples, and in the axial direction using dog-bone shaped samples, and four ratios of Sylgard®.

It can also be seen from Figure 4.5 that quite a large range of stiffness exists for coronary arteries tested in both the circumferential and axial directions. For this reason a further analysis was carried out to investigate the influence of using a stiffer material to represent the mock artery on stresses induced in the artery wall. The stress strain curve representing the stiffer material can be seen in Figure 4.6 below.

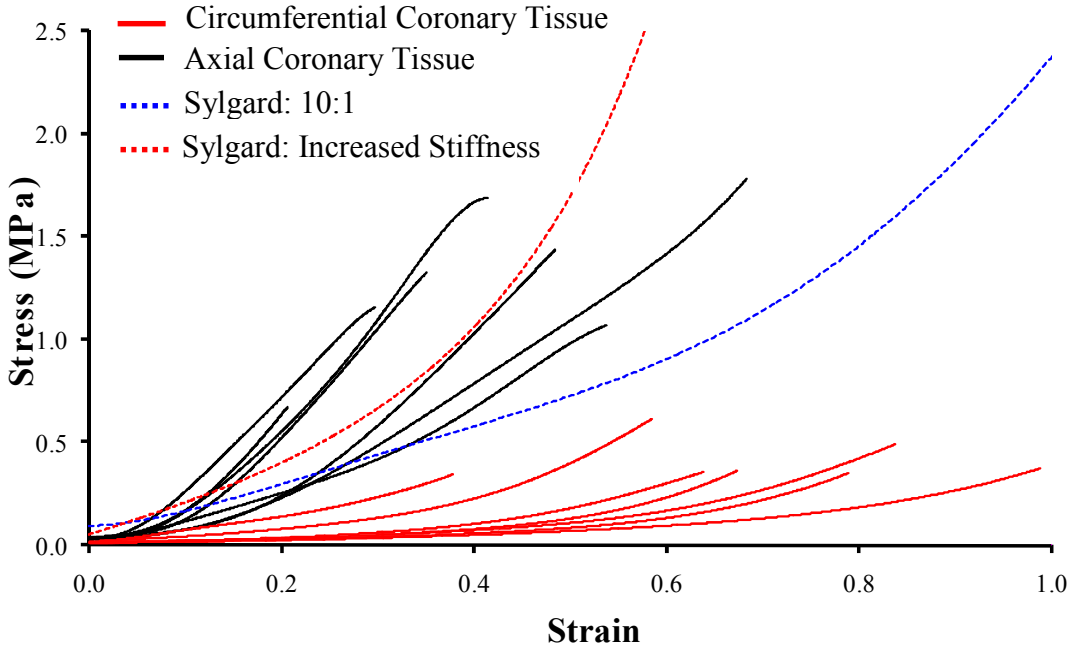

Figure 4.6: Uniaxial stress-strain curves for porcine coronary tissue and two ratios of Sylgard® Elastomer 184.

4.3 Case Study 1:

Assessment of Free Expansion of the Driver Stent

The Driver stent was freely expanded both numerically and experimentally such that it achieved an inner diameter of approximately 3.5 mm. The numerical free expansion of the Driver stent was expanded simulating a balloon expansion by applying a uniform pressure to the inner surface of the stent. In the first analysis, two separate simulations were carried out to identify the most realistic loading conditions to simulate a balloon expansion by applying a uniform pressure to the inner surface of the stent. In the second analysis, the effect of constraining the weld points on the stent was investigated. Having found the most suitable numerical methods to accurately expand the stent, these methods were then validated through experimental testing.

4.3.1 Numerical Free Expansion

4.3.1.1 Free Expansion of $Driver_{spf}$ and $Driver_{lpf}$

In this analysis, the effect of applying pressure to two different areas along the inner surface of the stent was investigated. A uniform pressure of 1925 kPa was applied to the two inner element faces along the length of the stent, representing the stent with the smaller amount of selected pressure faces, i.e. $Driver_{spf}$ see Figure 4.7 (a). A uniform pressure of 1095 kPa was applied to the four inner element faces along the length of the stent, representing $Driver_{lpf}$ as a larger number of faces have been selected, see Figure 4.7 (b). In both cases the stent was loaded such that it achieved an inner diameter of 3.5 mm on loading. All design aspects of the two stents used in this analysis are the same, the only difference between the two models being the area onto which the pressure is applied.

(a) Small Pressure Faces ($Driver_{spf}$)

Pressure = 1925 kPa

(b)Large Pressure Faces ($Driver_{lpf}$)

Pressure = 1095 kPa

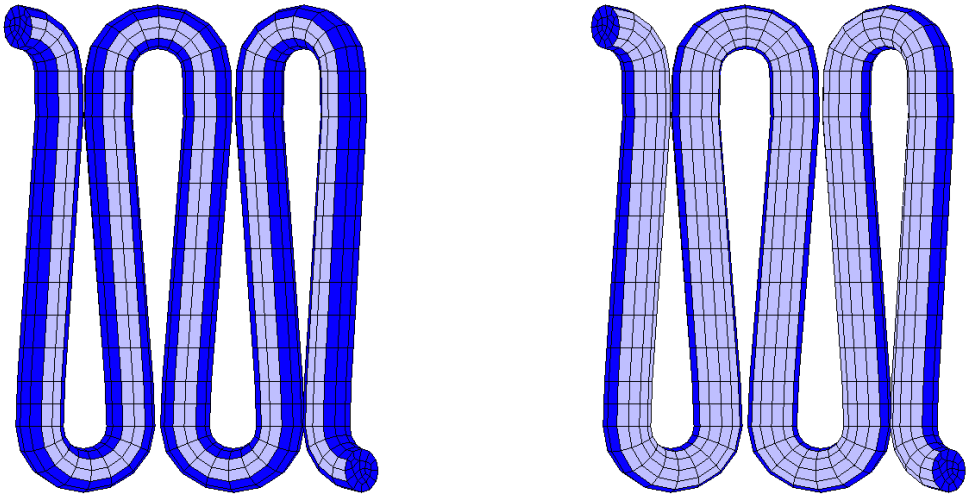

Figure 4.7: Simulation of balloon expansion on (a) small pressure faces versus (b) large pressure faces.

The radial expansion distribution was found to be similar for both $Driver_{spf}$ and $Driver_{lpf}$ in that both models exhibited highly uniform radial expansions with the highest radial displacement concentrated at the arcs of the struts, see Figure 4.8. The areas of peak radial displacement, however, were more concentrated for the stent expanded with a smaller number of pressure faces and subsequently a higher pressure. It was found that applying a lower pressure of 1095 kPa to a larger surface area results in a more uniform and even radial distribution. For this reason, and also due to the fact that this model, i.e. $Driver_{lpf}$, represents a more realistic pressure of 1095 kPa to load the stent, this model was considered to best simulate a balloon expansion and was therefore used for all subsequent simulations.

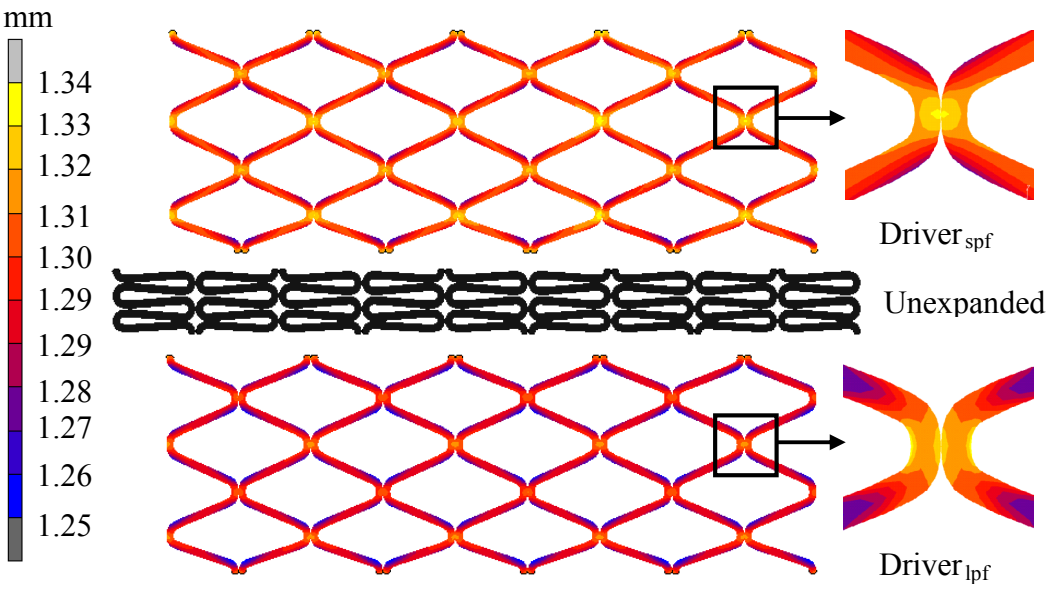

Figure 4.8: Resulting radial displacement distribution throughout stent structure of $Driver_{spf}$ and $Driver_{lpf}$ subjected to free expansion, achieving an inner diameter of 3.5 mm.

On examination of the von Mises stress contours on loading of the stent, it can be seen that the highest stresses are concentrated in the arcs of the struts, see Figure 4.9. Both $Driver_{spf}$ and $Driver_{lpf}$ exhibit similar degrees of stress concentration and variation throughout the stent structure. The variation in loading between $Driver_{spf}$ and $Driver_{lpf}$ had no impact on the magnitude or distribution of von Mises stresses in the stent with both resulting in maximum stresses of 975 MPa.

On examination of the Total Equivalent Plastic Strain contours on loading of the stent, it can be seen that the highest strains are also concentrated in the arcs of the struts, see Figure 4.10. Both $Driver_{spf}$ and $Driver_{lpf}$ exhibit similar magnitudes of strain concentration and also strain distribution throughout the stent structure with both stents resulting in maximum plastic strains of 0.28.

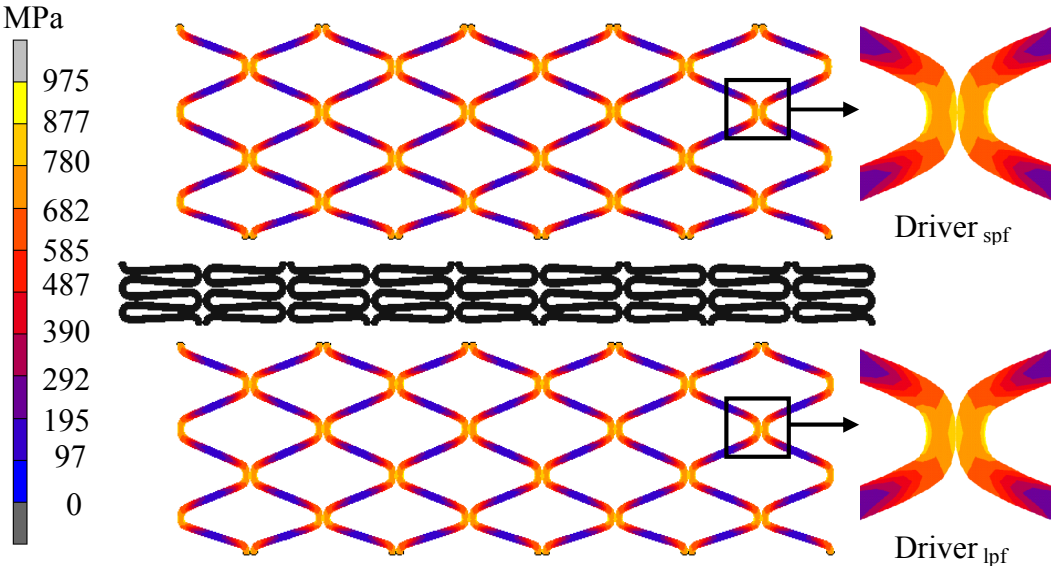

Figure 4.9: Resulting von Mises stress contours throughout stent structure of $Driver_{spf}$ and $Driver_{lpf}$ subjected to free expansion, achieving an inner diameter of 3.5 mm.

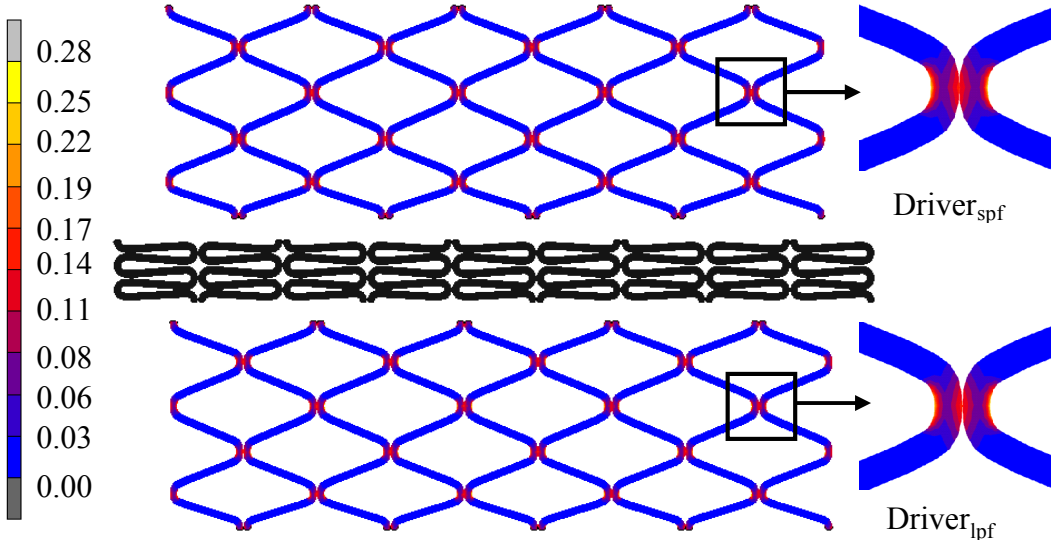

Figure 4.10: Resulting Total Equivalent Plastic strain contours throughout stent structure of $Driver_{spf}$ and $Driver_{lpf}$ subjected to free expansion, achieving an inner diameter of 3.5 mm.

4.3.1.2 Free Expansion of $Driver_{unfixed}$ and $Driver_{fixed}$

In this analysis, the effect of constraining the nodes at the weld points was investigated. In the first simulation, only the central weld point on the stent was constrained in the axial direction of the stent, thus representing $Driver_{unfixed.}$ In the second simulation, all weld points on the stent were constrained in the axial direction of the stent, thus representing $Driver_{fixed.}$ See Figure 4.11 below for indication of weld point locations (red arrows), and constrained nodes for both simulations. Both stents were freely expanded by applying a uniform pressure of 1095 kPa to the inner surface of the stent such that they achieved an inner diameter of approximately 3.5 mm each.

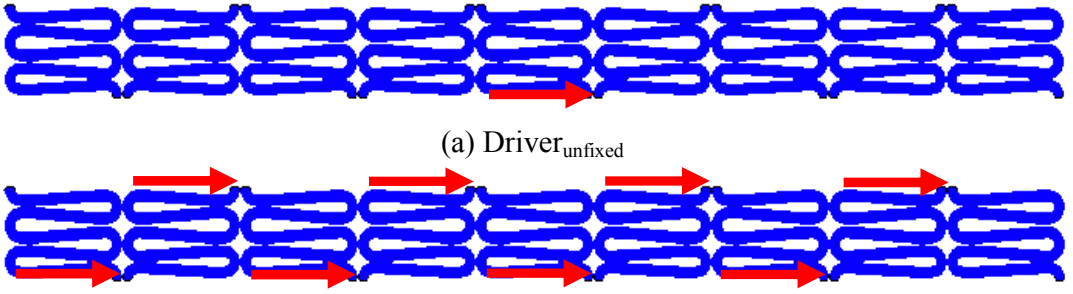

(a) $Driver_{unfixed}$

(b) $Driver_{fixed}$

Figure 4.11: Red arrows indicate weld points where stent was constrained to move in its axial direction for (a) $Driver_{unfixed}$ and (b) $Driver_{fixed}$.

The radial expansion distribution differed between $Driver_{unfixed}$ and $Driver_{fixed}$, however, both models maintained uniformity along their length, see Figure 4.12. It is quite clear from Figure 4.12 that the unfixed model shortened in length to a much greater extent in comparison to the fixed model, which actually spread outwards, leaving gaps between the repeating units of the stent. Once again, the areas of highest radial expansion were concentrated in the arcs. These areas of peak radial expansion were however slightly higher and more evident in the model which had all weld points fixed, i.e. $Driver_{fixed}$, which achieved a slightly higher internal expansion diameter of 3.57 mm as opposed to 3.53 mm for $Driver_{unfixed}$.

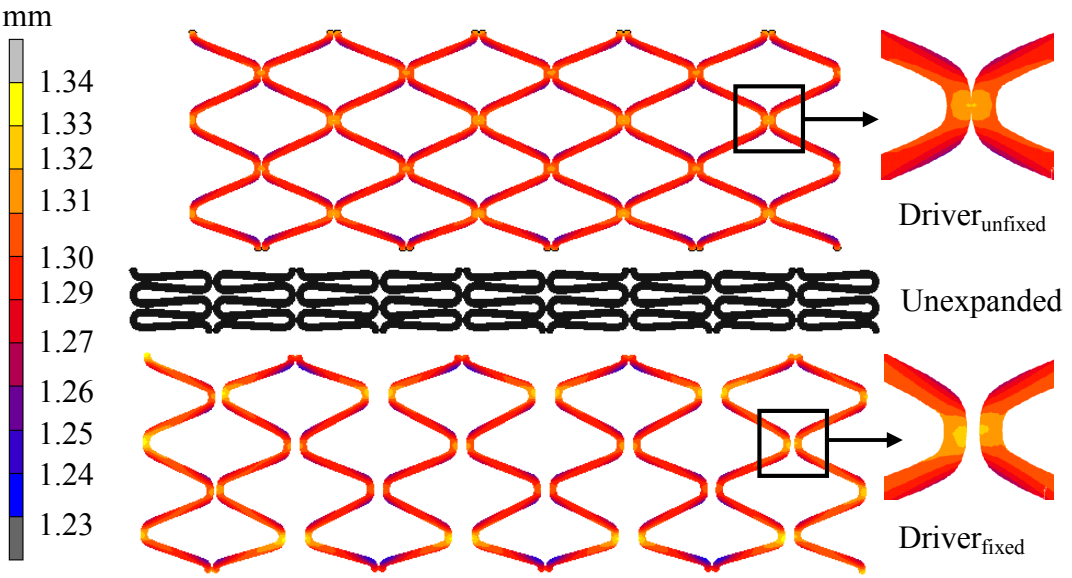

Figure 4.12: Resulting radial displacement distribution throughout stent structure of $Driver_{unfixed}$ and $Driver_{fixed}$ subjected to free expansion, achieving an inner diameter of 3.5 mm.

On examination of the von Mises stress contours on loading of the stent, it can be seen that the highest stresses are concentrated in the arcs of the struts, as was found previously, see Figure 4.13. Both $Driver_{unfixed}$ and $Driver_{fixed}$ exhibit similar degrees of stress concentration and variation throughout the stent structure, achieving a maximum von Mises stress of 972 MPa. The effect of fixing the weld points on the stent had no impact on the von Mises stress values.

Similarly, on examination of the Total Equivalent Plastic Strain contours on loading of the stent, it can be seen that the highest strains are also concentrated in the arcs of the struts, see Figure 4.14. Both $Driver_{unfixed}$ and $Driver_{fixed}$ exhibit similar levels of strain concentration and distribution throughout the stent structure, resulting in maximum Total Equivalent Plastic Strain of 0.27. The effect of fixing the weld points on the stent had no impact on the Total Equivalent Plastic Strain values.

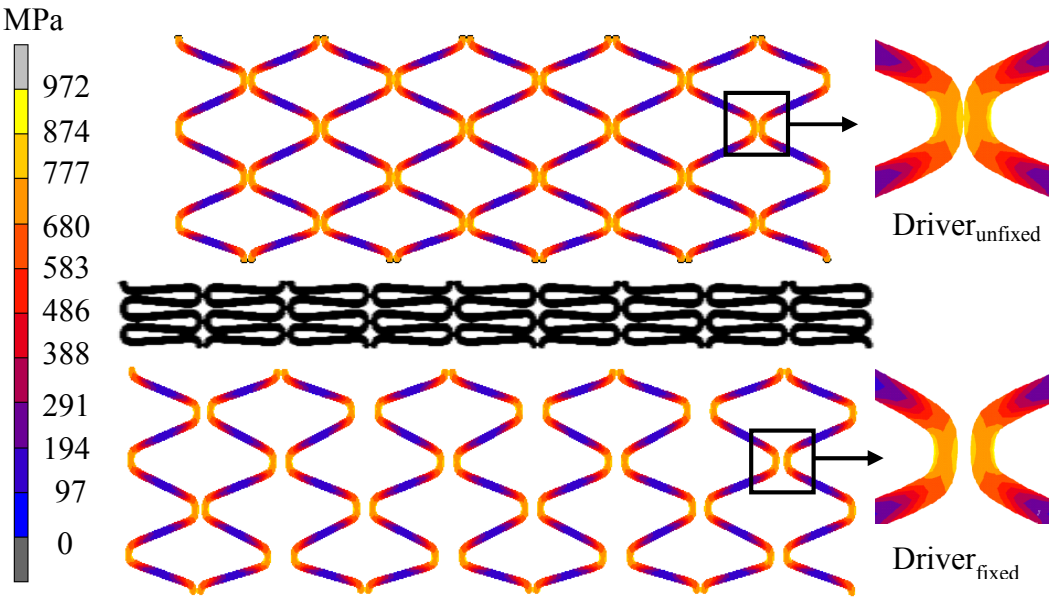

Figure 4.13: Resulting von Mises stress contours throughout stent structure of $Driver_{unfixed}$ and $Driver_{fixed}$ subjected to free expansion, achieving an inner diameter of 3.5 mm.

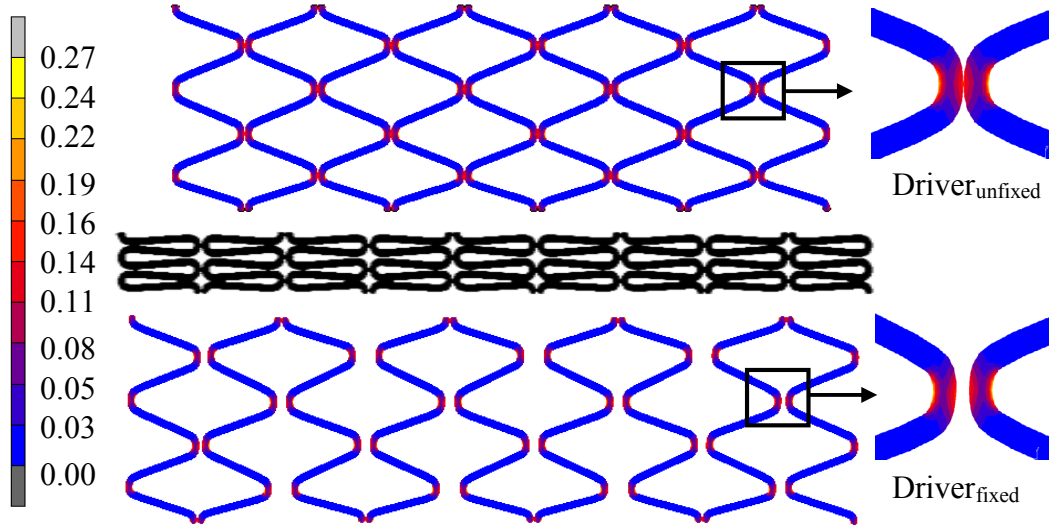

Figure 4.14: Resulting Total Equivalent Plastic strain contours throughout stent structure of $Driver_{unfixed}$ and $Driver_{fixed}$ subjected to free expansion, achieving an inner diameter of 3.5 mm.

Upon loading of the Driver stent in free expansion, both models were seen to shorten in length. $Driver_{unfixed}$ resulted in a much greater degree of foreshortening in comparison to $Driver_{fixed}$ which achieved results of 10.56% and 3.22%, respectively. This foreshortening can be seen both qualitatively and quantitatively, see Figure 4.12 and Table 4.1. Radial and longitudinal recoil, which is the

relative reduction in radius and length of the stent following balloon deflation, was seen to occur for both $Driver_{unfixed}$ and $Driver_{fixed}$. Both models achieved similar amounts of radial recoil and resulted in negative longitudinal recoil upon unloading, see Table 4.1. This negative longitudinal recoil resulted in the lengthening of the stent upon unloading, by 0.87% for $Driver_{unfixed}$ and 0.34% for $Driver_{fixed}$. Dogboning, which occurs when the ends of the stent radially expand to a greater extent compared with the central portion, was not observed in either the $Driver_{unfixed}$ or the $Driver_{fixed}$ models. Both models maintained uniform radial expansion throughout the length of the stent.

	Driver $_{unfixed}$	***Driver*** $_{fixed}$
Pressure (kPa)	1095	1095
Stent before expansion	(mm)	(mm)
R_{orig}	0.54	0.54
L_{orig}	9.00	9.00
Stent ID after loading (mm)	3.53	3.57
$R_{load\ proximal}$	1.77	1.79
$R_{load\ central}$	1.77	1.79
$R_{load\ distal}$	1.77	1.79
L_{load}	8.05	8.71
Stent ID after unloading (mm)	3.41	3.43
$R_{unload\ proximal}$	1.71	1.72
$R_{unload\ central}$	1.71	1.72
$R_{unload\ distal}$	1.71	1.72
L_{unload}	8.12	8.74
Calculated parameters	(%)	(%)
Radial recoil	3.39	3.91
Longitudinal recoil	-0.87	-0.34
Foreshortening	10.56	3.22
Dogboning	0.00	0.00

Table 4.1: Geometric data of $Driver_{unfixed}$ and $Driver_{fixed}$ through loading and unloading, subject to free expansion, achieving an inner diameter of 3.5 mm.

4.3.2 Experimental Free Expansion

In order to investigate the validation of the numerical free expansion of the Driver stent, $Driver_{exp}$, six actual Driver stents were freely expanded with the deformation of each stent being captured using a video extensometer. Images were captured every tenth of a second and these images were used to record and measure the four stent parameters: foreshortening, radial recoil, longitudinal recoil and dogboning, see Table 4.2. In such a way the results can be compared to those of the numerical expansion such that the most accurate and realistic numerical methods can be validated. All six stents were expanded using a balloon which was pressurised to a maximum value of 10 atm. A value of 10 atm, which corresponds to 1013.25 kPa, was chosen as it is the average pressure required to expand the Driver stent to an inner diameter of 3.5 mm following deployment, as indicated in the instructions for use. This compares well to the value of 1095 kPa which was used to expand the numerical models such that they achieved an inner diameter of 3.5 mm.

	Driver # 1	***Driver # 2***	***Driver # 3***	***Driver # 4***	***Driver # 5***	***Driver # 6***
Stent before expansion	*(mm)*	*(mm)*	*(mm)*	*(mm)*	*(mm)*	*(mm)*
R_{orig}	0.79	0.78	0.78	0.76	0.78	0.79
L_{orig}	9.10	9.13	8.98	8.93	9.06	8.99
Stent after loading	*(mm)*	*(mm)*	*(mm)*	*(mm)*	*(mm)*	*(mm)*
$R_{load\ proximal}$	1.80	1.79	1.83	1.84	1.85	1.84
$R_{load\ central}$	1.80	1.80	1.83	1.85	1.85	1.85
$R_{load\ distal}$	1.79	1.79	1.82	1.84	1.84	1.84
L_{load}	8.88	8.71	8.70	8.68	8.83	8.63
Stent after unloading	*(mm)*	*(mm)*	*(mm)*	*(mm)*	*(mm)*	*(mm)*
$R_{unload\ proximal}$	1.74	1.72	1.75	1.79	1.78	1.76
$R_{unload\ central}$	1.74	1.73	1.77	1.78	1.78	1.77
$R_{unload\ distal}$	1.74	1.73	1.76	1.78	1.78	1.77
L_{unload}	8.90	8.73	8.73	8.71	8.85	8.66
Calculated parameters	(%)	(%)	(%)	(%)	(%)	(%)
Radial recoil	3.33	3.89	3.28	3.78	3.78	4.32
Longitudinal recoil	-0.23	-0.23	-0.34	-0.35	-0.23	-0.35
Foreshortening	2.42	4.60	3.12	2.80	2.54	4.00
Dogboning	-0.56	-0.56	-0.55	-0.54	-0.54	-0.54

Table 4.2: Experimentally measured data for Driver stents through loading and unloading, subject to free expansion, achieving an inner diameter of 3.5 mm. All expanded with a pressure of 10 atm (1013.25 kPa).

The mean values for all four measured parameters were recorded and tabulated, see Table 4.3.

Measured Parameters (%)	Radial Recoil	Longitudinal recoil	Foreshortening	Dogboning
Mean ± Standard Deviation	3.73 ± 0.385	-0.29 ± 0.064	3.25 ± 0.871	-0.55 ± 0.009

Table 4.3: Mean and Standard Deviation for measured parameters resulting from the experimental free expansion of the Driver stent.

On close examination and comparison of both the numerical and experimental results, see Figure 4.15 below, it is clear to see that the numerical stent expansion, whereby all weld points were fixed, matches up most closely with the experimental results. This is most likely more representative of the real conditions whereby the friction between the balloon and the stent upon balloon and stent expansion would in some way constrain the stent from moving along the balloon.

The mean experimental Driver expansion, $Driver_{exp}$, and the fully constrained numerical Driver expansion, $Driver_{fixed}$, resulted in similar degrees of foreshortening, achieving values of 3.25% and 3.22% respectively. The numerical $Driver_{unfixed}$ model resulted in over three times greater foreshortening than the mean experimental. This higher degree in foreshortening experienced by the $Driver_{unfixed}$ model is due to the fact that the welds points were not constrained to move along the length of the stent and subsequently, the pressure upon loading caused the stent to shorten considerably in length.

Both numerical models, $Driver_{fixed}$ and $Driver_{unfixed}$, resulted in similar amounts of radial recoil, as mentioned previously, however, the $Driver_{fixed}$ model obtained the most similar result to that of the mean experimental value with only a small difference of 0.18% between them.

No significant difference in longitudinal recoil was noted between the mean experimental value and that of $Driver_{fixed}$, where both achieved negative values of -0.29% and -0.34%, respectively. Although the unfixed numerical model also achieved a negative value, it resulted in a higher measure of -0.87% foreshortening.

It was found that both numerical models resulted in no dogboning, whereas a very small degree of dogboning was recorded experimentally, resulting in a mean value of -0.55%.

Overall, the numerical model with the axially constrained welds, $Driver_{fixed}$, resulted in the closest and most realistic match to the mean experimental values for all four measured stent parameters. For this reason, the $Driver_{fixed}$ model can be said to be the most valid numerical model to represent the free expansion of the Driver stent.

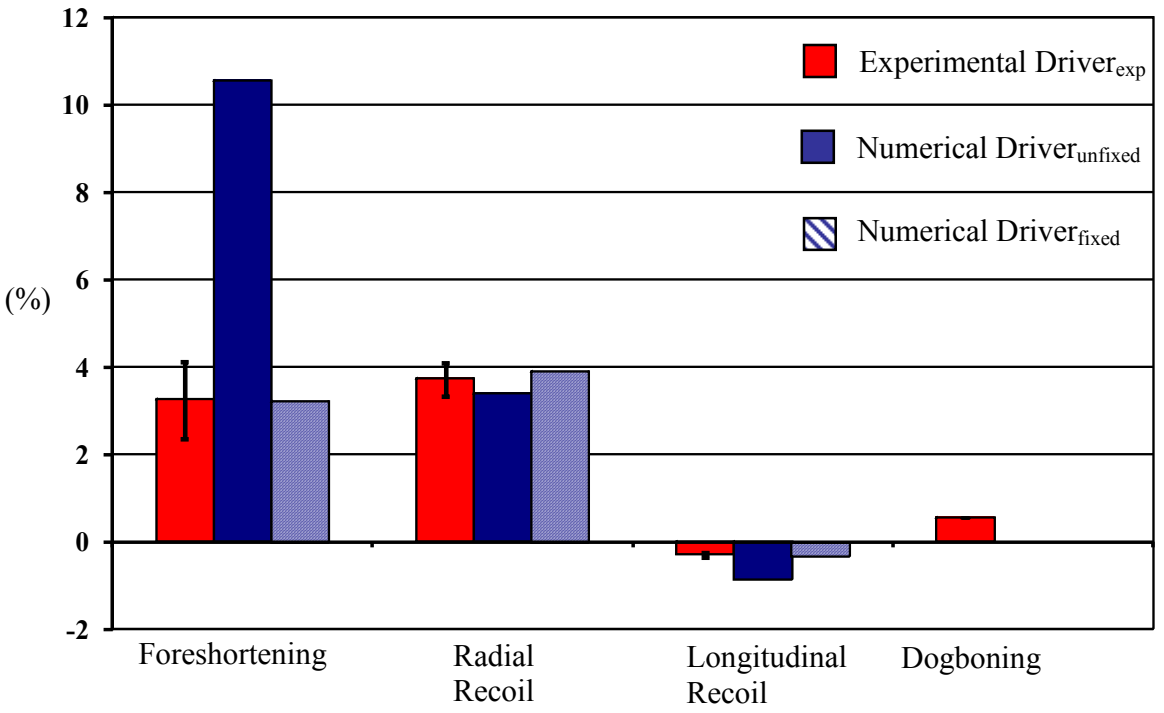

Figure 4.15: Graphical representation of results calculated for four measured parameters: (foreshortening, radial recoil, longitudinal recoil, and dogboning), for experimental mean values and both numerical simulations.

It can also be seen from a qualitative perspective, how closely the deformation of the numerical model, $Driver_{fixed}$, matches that of the experimental model, see Figures 4.16 and 4.17 below. Both experimental and numerical models exhibit uniform radial expansion along the length of the stent. Once again, it can be seen both experimentally, see Figure 4.16, and numerically, see Figure 4.17, how both stents undergo a small degree of foreshortening on loading of the stent. No significant longitudinal recoil can be seen from both the experimental and numerical images on unloading of the stent.

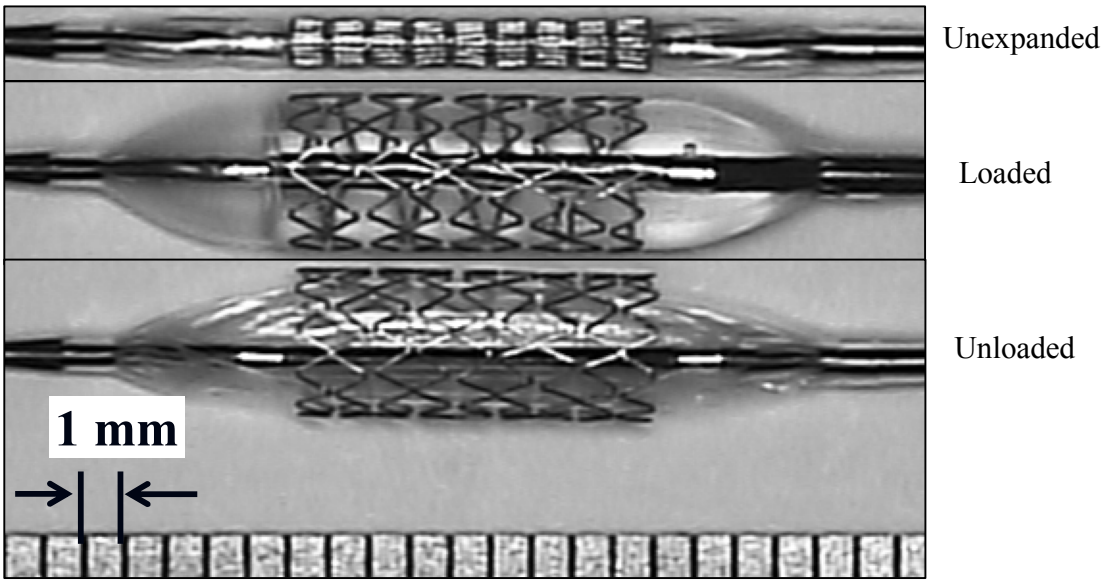

Figure 4.16: Experimental stent expansion images through unexpanded, loaded and unloaded configurations.

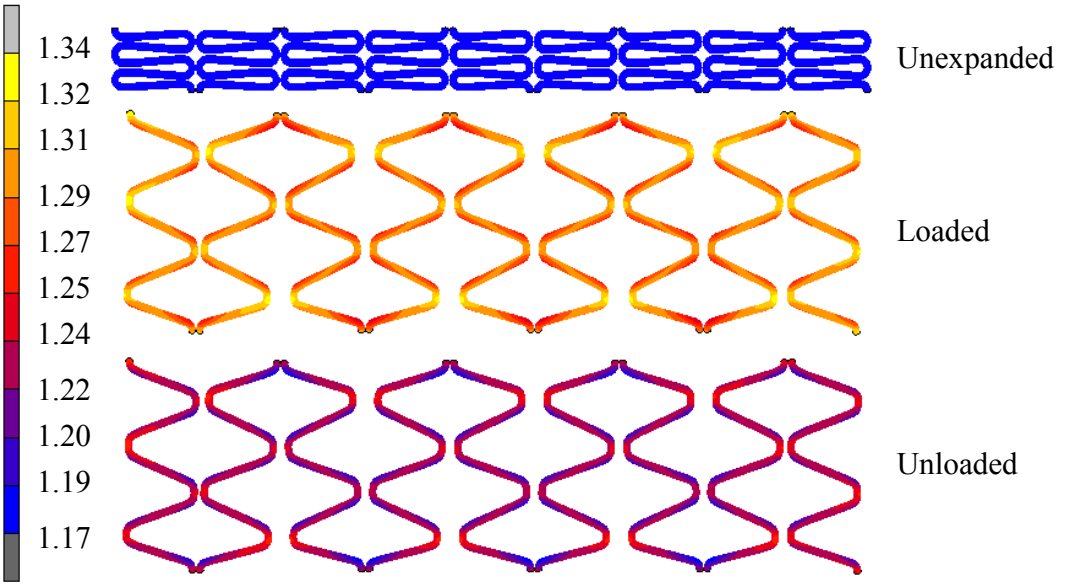

Figure 4.17: Numerical stent expansion images of $Driver_{fixed}$ through unexpanded, loaded and unloaded configurations.

4.4 Case Study 2:

Assessment of Driver Stent Expansion inside a Sylgard® Mock Artery

In this case study the Driver stent was expanded inside an idealised cylindrical vessel both numerically and experimentally, such that the most accurate numerical methods could be validated experimentally. The cylindrical vessel had a lumen diameter of 3 mm and a thickness of 0.5 mm. The actual vessel was composed of a ratio of 10 to 1 Sylgard® elastomer to curing agent, which was found previously to represent most accurately the mechanical behaviour of coronary vessels. Two separate analyses were carried out in this case study. In the first analysis, four numerical simulations were run whereby the mock artery was loaded by the Driver stent and the four stent parameters (foreshortening, radial and longitudinal recoil, and dogboning) were measured at unloading, when the pressure was fully removed. Two methods of numerical stent expansion were investigated:

1. ‘Original’ expansion, whereby the stent was expanded into the mock vessel and subsequently unloaded and
2. ‘Alternative’ expansion, which involved the initial free expansion of the stent and the subsequent unloading of an expanded vessel onto the expanded stent.

In both methods the stent was expanded such that it achieved an internal diameter of 3.5 mm. In both methods the effect of constraining the weld points to prevent axial movement was investigated. The pressures required to expand the stents using the original and alternative methods were 1600 kPa and 1095 kPa respectively. A lower pressure was required to expand the stent in the alternative expansion method as the stent was expanded independently of the artery. A separate uniform linearly increasing pressure was applied to the inner surface of the artery such that it was expanded beyond the stent. Once the pressure was removed from the inner surface of the artery, the artery subsequently unloaded onto the expanded stent. In the second analysis, to further validate the numerical methods used, the resulting strains induced in the mock artery for the most valid numerical simulation were compared to those of the actual strains recorded in the Sylgard® vessel.

Unlike the full numerical models used for the free expansion validation, only five repeating rings of the Driver stent were modelled for each simulation in this case study, in order to reduce computational time as the models also included a Sylgard® vessel. Measures for longitudinal recoil and foreshortening, assuming the full length of the stent, i.e. nine links were recorded.

4.4.1 Numerical Expansion

The radial expansion distribution was found to differ between the original and alternative expansion methods at unloading. The original method of expansion led to a non-uniform radial expansion in comparison to the alternative method which expanded to an almost fully uniform diameter along its entire length. The lowest values of radial displacement were observed at the end of the stent structure for the original expansion, see Figure 4.18. The application of axially constrained nodes at the weld points however, did not affect the radial distribution of the stent structure as

both $Driver_{unfixed}$ and $Driver_{fixed}$ resulted in similar radial displacement distributions for the original expansion method. The use of axially constrained nodes at the weld points was seen to have less of an effect on the overall expansion of the stent when it was expanded inside a vessel. For free expansion, it was found that the use of constrained weld points led to a more realistic expansion of the stent, however, in this loadcase it was noted that the use of these constrained nodes had little or no effect on the expansion of the stent when it was expanded inside a vessel. The vessel wall itself may have acted as a boundary, constraining the stent from moving along its axial length as it applied a radial load along the length of the stent. However, as with the free expansion, the alternative expansion of $Driver_{unfixed}$ inside a vessel resulted in the shortening of the stent upon loading, which is unrealistic of the actual behaviour of the Driver stent, as noted previously.

The resulting von Mises stress contours show similar stress distribution patterns between $Driver_{unfixed}$ and $Driver_{fixed}$ for both the originally expanded and the alternatively expanded stents, see Figure 4.19, on unloading of the stent. As with the free expansion of the stents the areas of highest stresses are located along the arcs of the stent structure.

The resulting Total Equivalent Plastic Strain contours again show similar patterns of strain distribution between $Driver_{unfixed}$ and $Driver_{fixed}$ for both the originally expanded and the alternatively expanded stents, see Figure 4.20, on unloading of the stent.

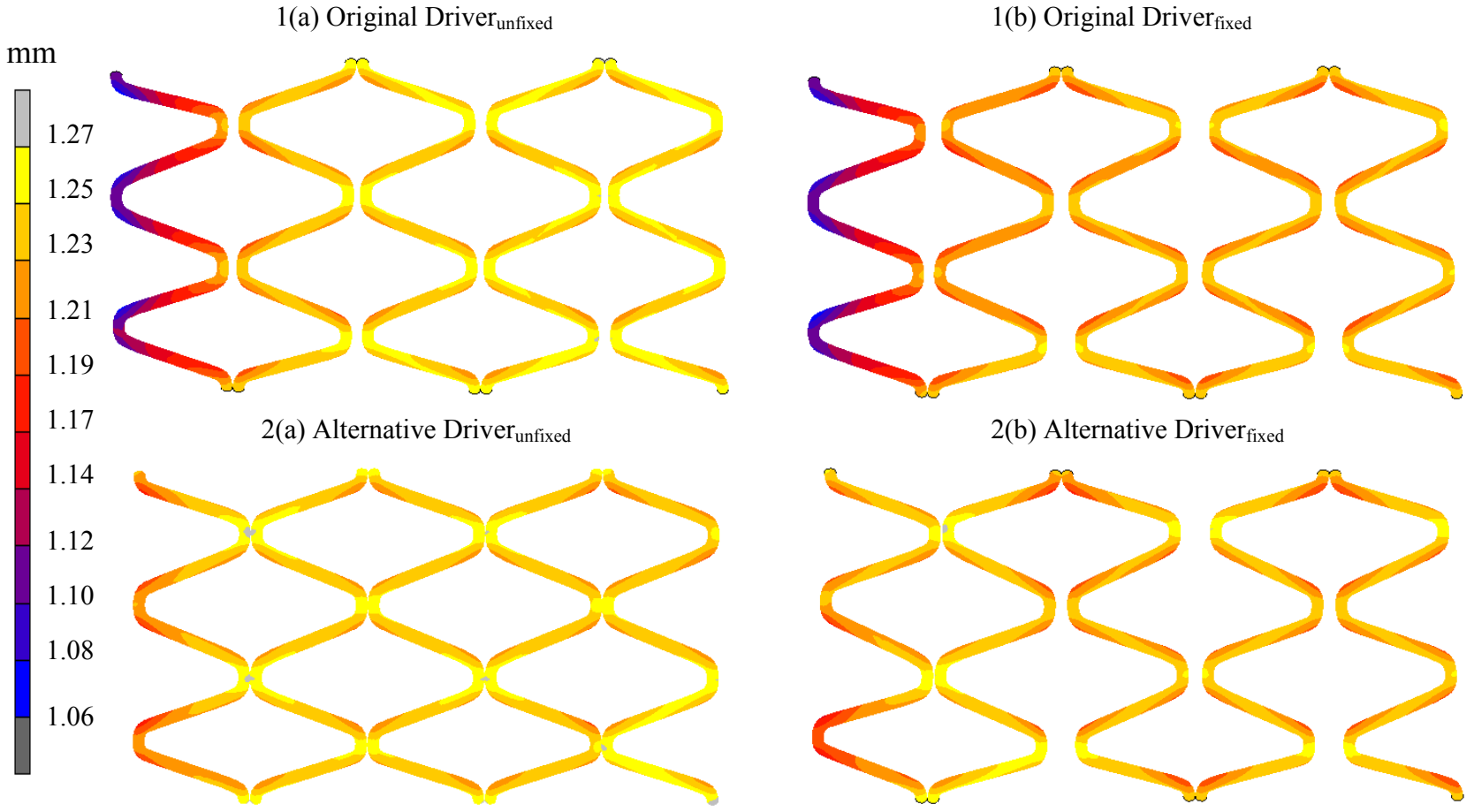

Figure 4.18: Resulting radial displacement distribution throughout the stents for the originally and alternatively expanded (a) Driver$_{unfixed}$ and (b) Driver$_{fixed}$ stents, under the influence of a mock Sylgard® artery, at unloading of the stent.

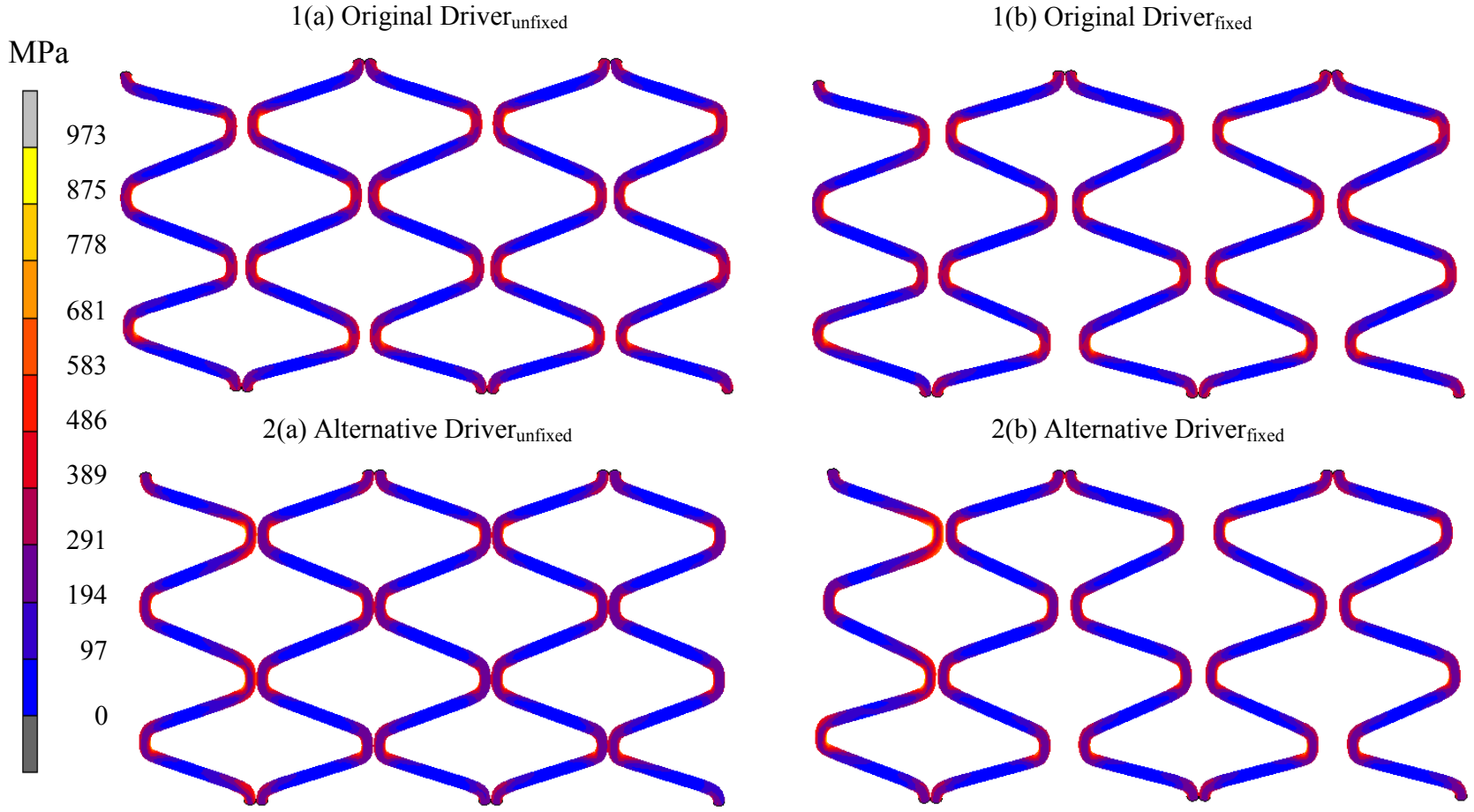

Figure 4.19: Resulting von Mises Stress contours throughout the stents for the originally and alternatively expanded (a) Driver$_{unfixed}$ and (b) Driver$_{fixed}$ stents, under the influence of a mock Sylgard® artery, at unloading of the stent.

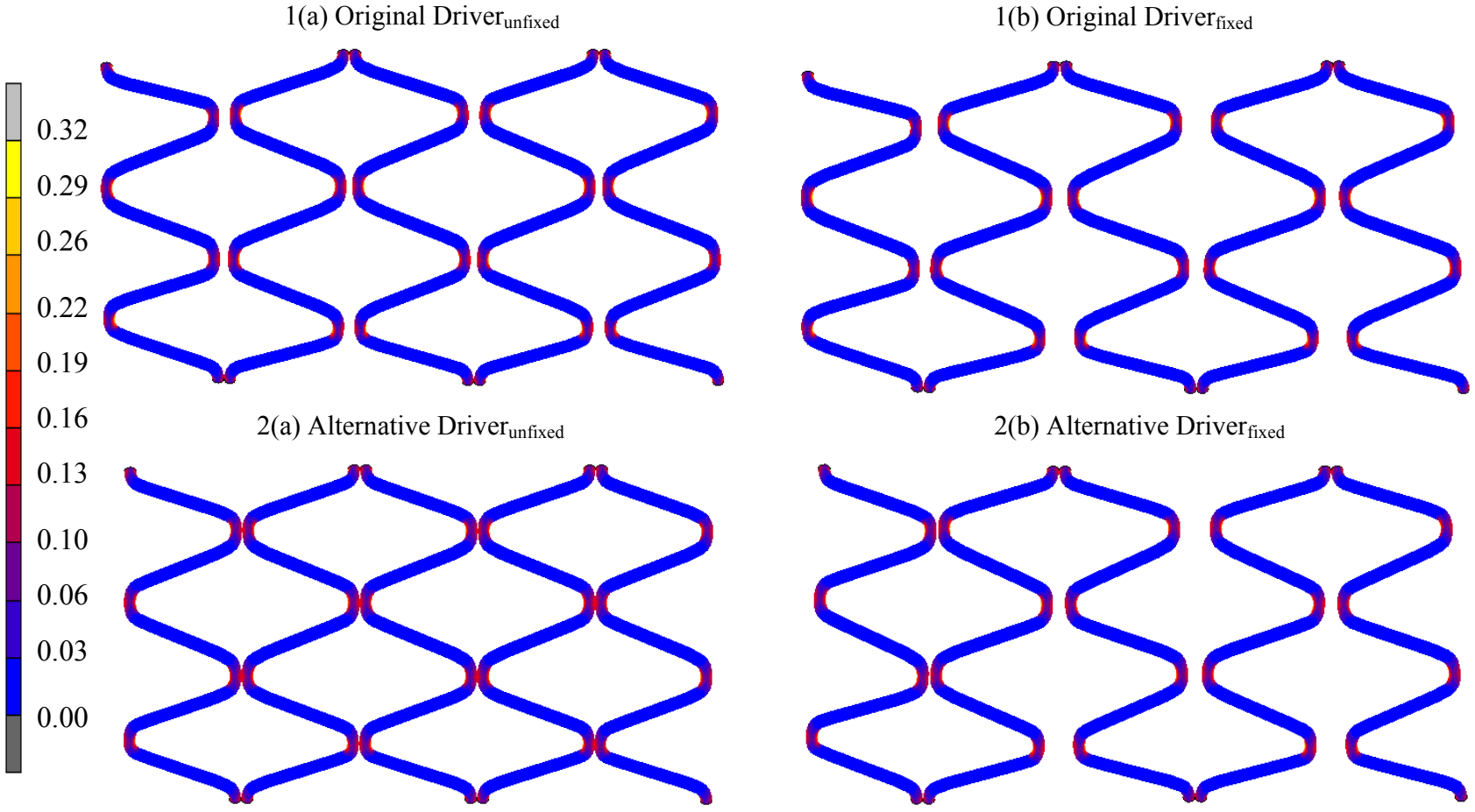

Figure 4.20: Resulting Total Equivalent Plastic Strain contours throughout the stents for the originally and alternatively expanded (a) Driver$_{unfixed}$ and (b) Driver$_{fixed}$ stents, under the influence of a mock Sylgard® artery, at unloading of the stent.

	***Driver*$_{unfixed}$**	***Driver*$_{fixed}$**
Pressure (kPa)	1600	1600
Stent before expansion	(mm)	(mm)
R_{orig}	0.54	0.54
L_{orig}	5.00	5.00
L_{orig} – Assuming 9 links	9.00	9.00
Stent ID after loading (mm)	3.61	3.59
$R_{load\ proximal}$	1.64	1.63
$R_{load\ central}$	1.81	1.80
L_{load}	4.69	4.90
L_{load} – Assuming 9 links	8.38	8.80
Stent ID after unloading (mm)	3.41	3.39
$R_{unload\ proximal}$	1.55	1.54
$R_{unload\ central}$	1.71	1.70
L_{unload}	4.63	4.91
L_{unload} – Assuming 9 links	8.26	8.82
Calculated parameters	(%)	(%)
Radial recoil	5.52	5.56
Longitudinal recoil (5 links)	1.28	-0.20
Longitudinal recoil (9 links*)	1.43	-0.23
Foreshortening (5 links)	6.20	2.00
Foreshortening (9 links*)	6.89	2.22
Dogboning	-10.37	-10.43

Table 4.4: Geometric data of $Driver_{unfixed}$ and $Driver_{fixed}$ through original expansion, under the influence of a Sylgard® vessel, achieving an inner diameter of 3.5 mm. *Assuming 9 links in length.

	***Driver*$_{unfixed}$**	***Driver*$_{fixed}$**
Pressure (kPa)	1095	1095
Stent before expansion	(mm)	(mm)
R_{orig}	0.54	0.54
L_{orig}	5.00	5.00
L_{orig} – Assuming 9 links	9.00	9.00
Stent ID after loading (mm)	3.55	3.57
$R_{load\ proximal}$	1.72	1.71
$R_{load\ central}$	1.78	1.79
L_{load}	4.41	4.87
L_{load} – Assuming 9 links	7.82	8.74
Stent ID after unloading (mm)	3.45	3.43
$R_{unload\ proximal}$	1.64	1.62
$R_{unload\ central}$	1.73	1.72
L_{unload}	4.43	4.79
L_{unload} – Assuming 9 links	7.87	8.58
Calculated parameters	(%)	(%)
Radial recoil	2.81	3.91
Longitudinal recoil (5 links)	-0.45	1.64
Longitudinal recoil (9 links*)	-0.64	1.83
Foreshortening (5 links)	11.80	2.60
Foreshortening (9 links*)	13.11	2.89
Dogboning	-3.49	-4.68

Table 4.5: Geometric data of $Driver_{unfixed}$ and $Driver_{fixed}$ through alternative expansion, under the influence of a Sylgard® vessel, achieving an inner diameter of 3.5 mm. *Assuming 9 links in length.

As with the free expansion of the Driver stent, foreshortening was also evident when the stents were expanded inside the vessel. Once again the unconstrained model, $Driver_{unfixed}$ was found to foreshorten to a greater amount in comparison to the $Driver_{fixed}$ model, for both the original and alternative expansion methods, see Tables 4.4 and 4.5. It was noted, however, that this difference in the degree of foreshortening was greater for the alternative expansion method, which resulted 11.80% foreshortening for the $Driver_{unfixed}$ model. This is due to the fact that the alternative expansion technique acts as a free expansion up until unloading of both the stent and the vessel, whereby the vessel is unloaded onto the fully expanded stent. In such a way, the vessel has no impact on the foreshortening of the stent which occurs prior to unloading. For the original expansion method the $Driver_{unfixed}$ model was found to foreshorten by 6.20%, which is three times greater than the $Driver_{fixed}$ model.

Upon unloading, the longitudinal recoil was found to vary between $Driver_{unfixed}$ and $Driver_{fixed}$ and again between the original and alternative expansion methods. For the original method, at unloading, the $Driver_{unfixed}$ model was found to undergo six times greater recoil in comparison to $Driver_{fixed}$, see Table 4.4. In fact, while the $Driver_{unfixed}$ model undergoes significant longitudinal recoil, the $Driver_{fixed}$ model undergoes only -0.20% recoil. The negative value indicates that the stent actually elongates upon unloading. A similar trend was found for free expansion where both $Driver_{unfixed}$ and $Driver_{fixed}$ resulted in -0.87% and -0.29% longitudinal recoil respectively. Quite the opposite was found for the alternative expansion, whereby the $Driver_{unfixed}$ model was found to undergo almost four times less longitudinal recoil than $Driver_{fixed}$, which resulted in 1.64% recoil, see Table 4.5. The $Driver_{unfixed}$ model was found to elongate by 0.45% upon unloading of the stent.

Both the $Driver_{unfixed}$ and the $Driver_{fixed}$ models achieved similar amounts of radial recoil for the original expansion of 5.52% and 5.56% respectively, see Table 4.4. For the alternative expansion however, the $Driver_{fixed}$ model was found to radially recoil to a greater amount of 3.91%, than that of $Driver_{unfixed}$ which resulted in 2.81%, see Table 4.5.

Dogboning was found to occur for both the original and the alternative expansion methods. The $Driver_{unfixed}$ and $Driver_{fixed}$ models both resulted in a greater degree of dogboning for the original expansion method in comparison to the alternative expansion method. The alternative expansions resulted in 3.5-4.7% dogboning, as can be seen in Table 4.5.

4.4.2 Experimental Expansion

In order to validate the numerical expansion of the Driver stent inside a mock artery, to imitate a typical stenting procedure, six actual Driver stents were expanded inside compliant Sylgard® elastomeric cylinders. The deformation of each stent was captured using a video extensometer as was used for the free expansion validation. Images were captured every tenth of a second and these images were used to record and measure the four stent parameters, foreshortening, radial recoil, longitudinal recoil and dogboning, see Table 4.6. In such a way the results can be compared to those of the numerical expansion such that the most accurate and realistic numerical methods can be validated. All six stents were expanded using a balloon which was pressurised to a maximum value of 10 atm. A value of 10 atm, corresponding to 1013.25 kPa, was chosen as it was the average pressure required to expand the Driver stent to an inner diameter of 3.5 mm following deployment, as indicated in the instructions for use.

	Driver # 1	***Driver # 2***	***Driver # 3***	***Driver # 4***	***Driver # 5***	***Driver # 6***
Stent before expansion	*(mm)*	*(mm)*	*(mm)*	*(mm)*	*(mm)*	*(mm)*
R_{orig}	0.76	0.75	0.78	0.78	0.72	0.76
L_{orig}	8.90	8.95	8.96	8.90	8.97	8.81
Stent after loading	*(mm)*	*(mm)*	*(mm)*	*(mm)*	*(mm)*	*(mm)*
$R_{load\ proximal}$	1.94	1.99	1.91	1.91	1.98	1.92
$R_{load\ central}$	1.97	2.01	1.92	1.93	2.00	1.95
L_{load}	8.62	8.67	8.72	8.60	8.70	8.54
Stent after unloading	*(mm)*	*(mm)*	*(mm)*	*(mm)*	*(mm)*	*(mm)*
$R_{unload\ proximal}$	1.80	1.83	1.86	1.88	1.89	1.88
$R_{unload\ central}$	1.88	1.91	1.87	1.88	1.90	1.89
L_{unload}	8.51	8.48	8.59	8.43	8.57	8.37
Calculated parameters	(%)	(%)	(%)	(%)	(%)	(%)
Radial recoil	4.57	4.98	2.60	2.60	5.00	3.10
Longitudinal recoil	1.28	2.20	1.49	1.98	1.49	1.99
Foreshortening	3.15	3.13	2.68	3.37	3.01	3.06
Dogboning	-1.55	-1.01	-0.52	-1.05	-1.01	-1.56

Table 4.6: Experimental measured data of Driver stent through loading and unloading, under the influence of a Sylgard® vessel, achieving an inner diameter of 3.5 mm. All expanded with a pressure of 10 atm (1013.25 kPa).

The mean values for all four measured parameters were recorded and tabulated, see Table 4.7 below.

Measured Parameters (%)	Radial Recoil	Longitudinal recoil	Foreshortening	Dogboning
Mean ± Standard Deviation	3.80 ± 1.166	1.74 ± 0.365	3.07 ± 0.226	-1.12 ± 0.392

Table 4.7: Mean and Standard Deviation for measured parameters resulting from the experimental free expansion of the Driver stent.

Experimental results showed a general increase in the four measured parameters, as recorded in Table 4.7, when compared to those recorded for the free expansion, see Table 4.3. Radial recoil increased from an average of 3.73% for free expansion to 3.80% for expansion inside a vessel. The longitudinal recoil increased significantly from a negative value of -0.29% for free expansion to 1.74% for expansion inside a Sylgard® vessel. Twice as much dogboning was observed for expansion inside the Sylgard® vessel when compared to free expansion. This general increase in results is due to the impact of the Sylgard® vessel on both loading and unloading of the stent and vessel. A slight decrease in foreshortening, from 3.25% for free expansion, to 3.07% for expansion inside a vessel, was noted. This decrease in foreshortening is again due to the Sylgard® tube which constrains the stent to some degree from movement along its axial length.

On close examination of the results for both the experimental and numerical expansions, see Figure 4.21, it is clear to see that the alternative numerical stent expansion, whereby all weld points are axially constrained, matches up most closely with the experimental results. The mean experimental Driver expansion, $Driver_{exp}$, and the fully constrained alternative numerical Driver expansion, $Driver_{fixed}$, resulted in similar degrees of foreshortening, achieving values of 3.07% and 2.60% respectively. The aforementioned models resulted in even closer values for radial recoil, with $Driver_{exp}$ recoiling radially by an average of 3.80% as compared to 3.91%

for the alternatively expanded $Driver_{fixed}$. Both $Driver_{exp}$ and the alternatively expanded $Driver_{fixed}$ model resulted in the shortening of the stent upon unloading of 1.74% and 1.64% respectively. Quite a significant difference however was observed for dogboning, whereby experimentally minimal dogboning of -1.12% was observed at the last repeating ring of the stent. Four times greater dogboning was recorded for the alternatively expanded $Driver_{fixed}$ model, however the dogboning was also observed to occur in the final repeating ring of the stent. This discrepancy in the results for dogboning and indeed for the other measured parameters can be said to be due to the non existence of a balloon model in the numerical simulation. However, the results for foreshortening, and both radial and longitudinal recoil were seen to match up very closely.

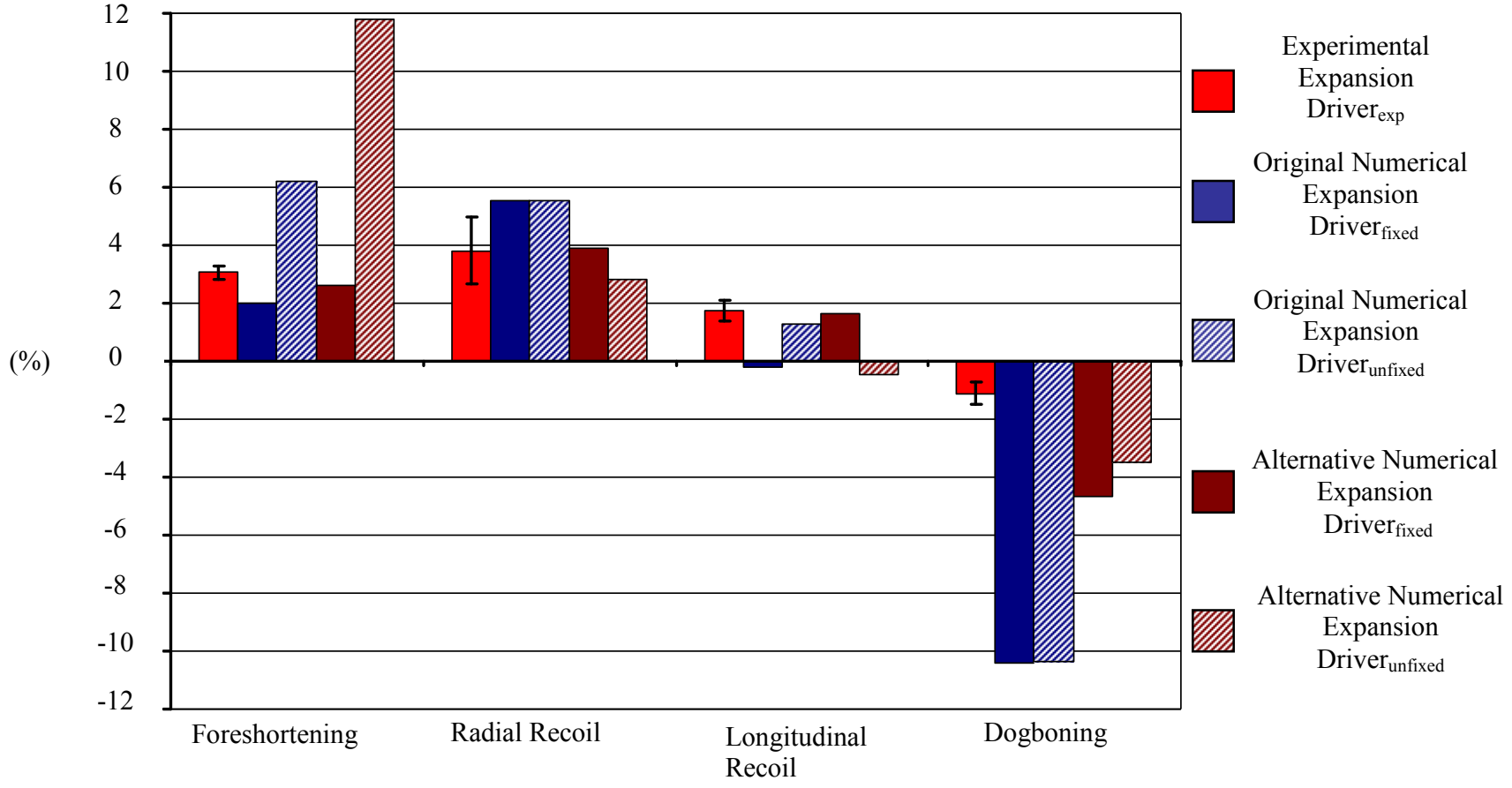

Figure 4.21: Graphical representation of results calculated for four measured parameters: (foreshortening, radial recoil, longitudinal recoil, and dogboning), for experimental mean values and all four numerical simulations.

4.4.3 Further Assessment of Numerical Methods using Strain Analysis

In this analysis the strains induced in the Sylgard® wall when the vessel was fully loaded were examined both experimentally and numerically. The strains resulting in the alternatively expanded numerical model, $Driver_{fixed}$, were compared to those of the experimental model as this was previously determined to be the most valid model in terms of uniform radial expansion, foreshortening, and both radial and longitudinal recoil.

For the experimental models, markers were placed on the Sylgard® tubes prior to stent expansion, such that the axial and transverse movement of these markers could be traced and used to record both the axial and transverse strains at unloading of the stent. Images were stored every tenth of a second during stent expansion, however, only every hundredth image was analysed for measurements as the movement of the markers was so small. Three separate stent expansions were investigated, and the mean axial and transverse strains recorded.

For the numerical model, the strains were measured in the axial and transverse directions again at unloading, by tracking nodes placed at the same locations as the markers placed on the experimental models.

Figure 4.22 below illustrates the transverse strains measured over time for one of the experimental stent expansions. It also identifies marked occurrences during stent expansion which influenced the strain induced in the vessel over the time of the balloon and subsequent stent expansion, and the balloon deflation, and subsequent unloading of the stent. Zero strain is recorded initially as the stent is in its unexpanded state and hence not impacting the vessel. As the ends of the stent begin to expand before the entire body of the stent, known as end flaring, this causes transverse strains of -11.34% resulting in a deflection in the curve as shown. As the entire body of the stent expands the strain begins to increase quite rapidly to a

maximum transverse strain of 14.29%. Then, as the pressure is removed from the balloon and the stent is unloaded, the strain begins to decrease to a final unloaded transverse strain of 7.14%, half of its maximum strain.

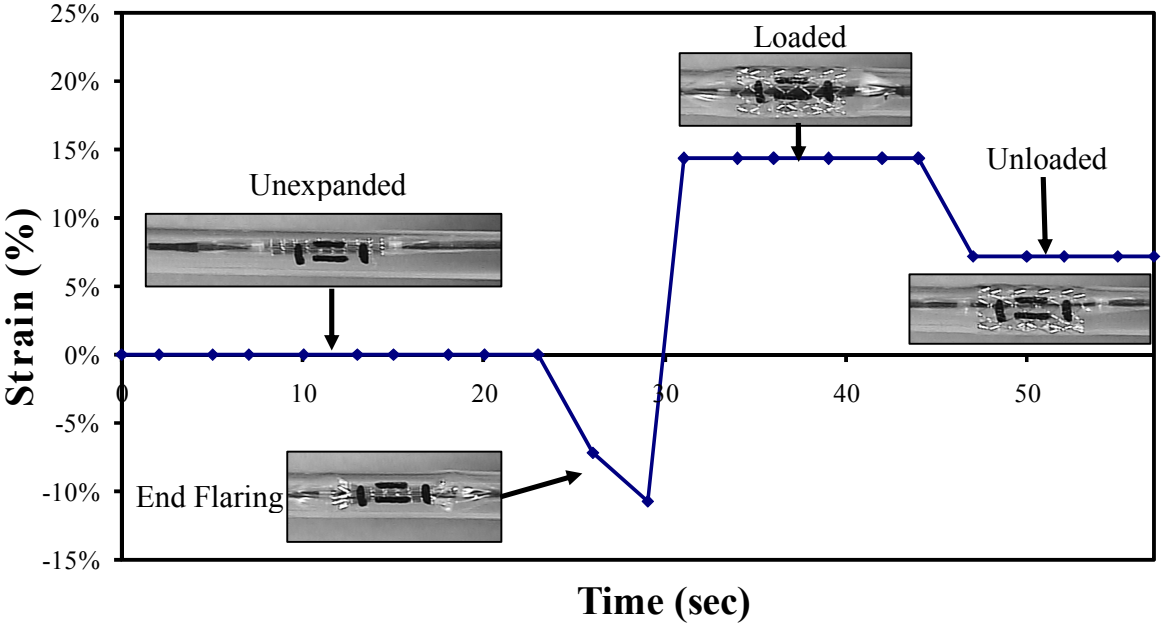

Figure 4.22: Graphical representation of experimental transverse strains measured over time of stent expansion and unloading including identified locations influencing strain.

As measurements recorded in the transverse direction are taken from a curved surface, the length of the arc, i.e. the actual distance between the transverse markers, was calculated and the subsequent strains recorded over time, see Figure 4.23 below. (See Chapter 3 Materials and Methods, Section 3.6.2 for further details on calculation.) This had little significance on the results previously recorded. The maximum strain at loading, taking into consideration the curved surface of the vessel, was increased by only 1.2%, whereas the maximum strain at unloading was increased by 1.1%.

The following graphs, Figure 4.23 and Figure 4.24, represent the resulting transverse and axial strains recorded over time of stent deployment and unloading for one of the experimental models.

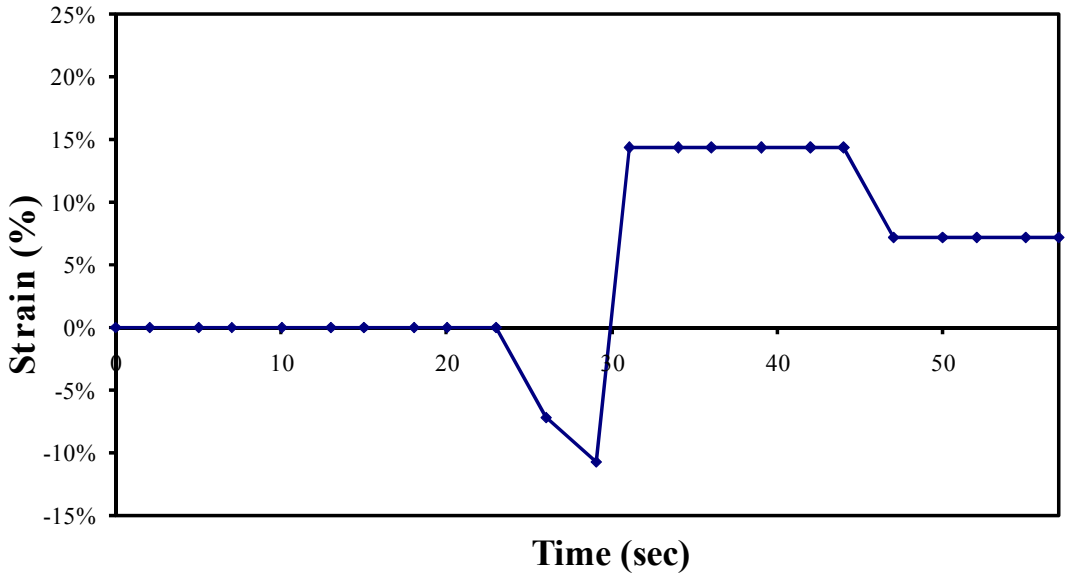

Figure 4.23: Graphical representation of experimental transverse strains measured over time of stent expansion and unloading taking into consideration the cylindrical shape of the vessel.

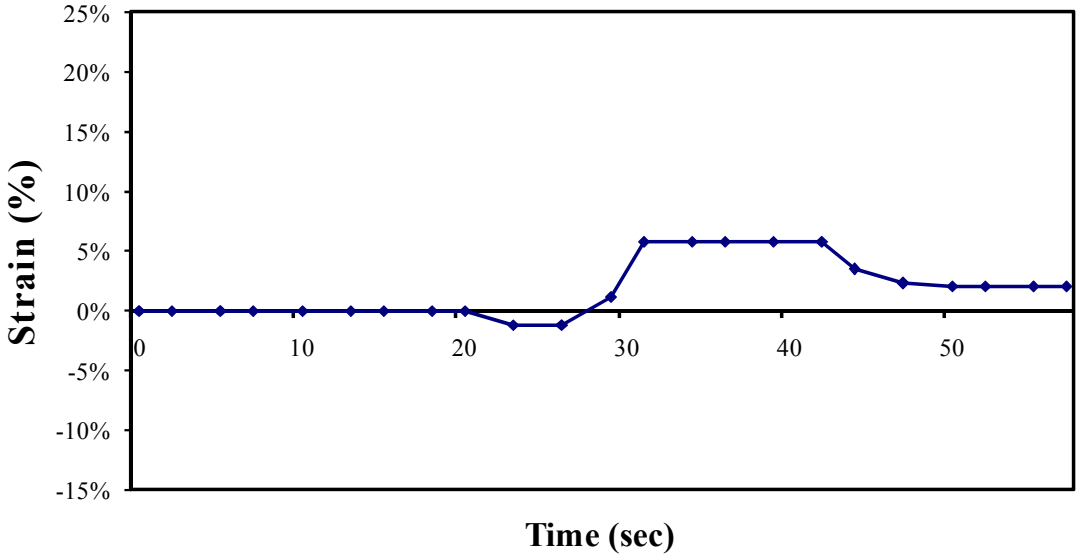

Figure 4.24: Graphical representation of experimental axial strains measured over time of stent expansion and unloading.

Both axial and transverse strains were only measured at unloading of the stent and vessel for the numerical model, $Driver_{fixed}$, as the vessel was not in contact with the stent upon loading for the alternative expansion method.

	Transverse Strain at Unloading (%)	Axial Strain at Unloading (%)
Average Experimental	8.71 ± 0.884	1.23 ± 0.713
Alternative Numerical Driver$_{fixed}$	8.57	0.43

Table 4.8: Table of results indicating maximum strains at unloading for the average experimental results and the alternatively expanded Driver$_{fixed}$ model.

Both experimental and numerical strain analyses resulted in considerably higher transverse strains in comparison to the axial strains measured. It is clear to see from Table 4.8 that the alternatively expanded numerical model provides a good indication of the strains induced in the unloaded vessel, particularly for the transverse strains measured, whereby the experimental and numerical models resulted in strains of 8.71% and 8.57% respectively. The experimental result obtained for axial strain was almost three times greater than that of the numerical model but both are very low values.

4.5 Case Study 3:

Numerical Investigation into the Effect of Varying the Elastic Properties of Mock Arteries on Stress Analysis

In this final case study, the effect of increasing the stiffness of the Sylgard® vessel on the stresses induced was investigated. A further simulation was carried out whereby the $Driver_{fixed}$ model was alternatively expanded inside a Sylgard® vessel almost three times stiffer than the vessel being used in the simulations up to this point. The stress strain curve representing this stiffer material model, see Figure 4.6, lies within the range of data for the tissue tested in the axial direction, whereas the previous Sylgard® stress strain curve lay between the extremes of both the axial and circumferential stress strain curves. This stiffer model will be referred to as S2, whereas, the previously modelled vessel will be referred to as S1. Both Driver stents in this case study were expanded with the same pressure of 1095 kPa as the alternative expansion method consists of a the initial free expansion of the stent and subsequent unloading of a vessel onto the expanded stent. Both S1 and S2 achieved final lumen diameters of 3.56 mm and 3.54 mm respectively.

The stresses induced in the vessels were examined at unloading, when the pressure was fully removed from the stents, in the circumferential, radial and longitudinal directions. Tensile stresses recorded in the radial direction, and both tensile and compressive stresses were recorded in the longitudinal direction, see Figures 4.25, 4.26, and 4.27 respectively.

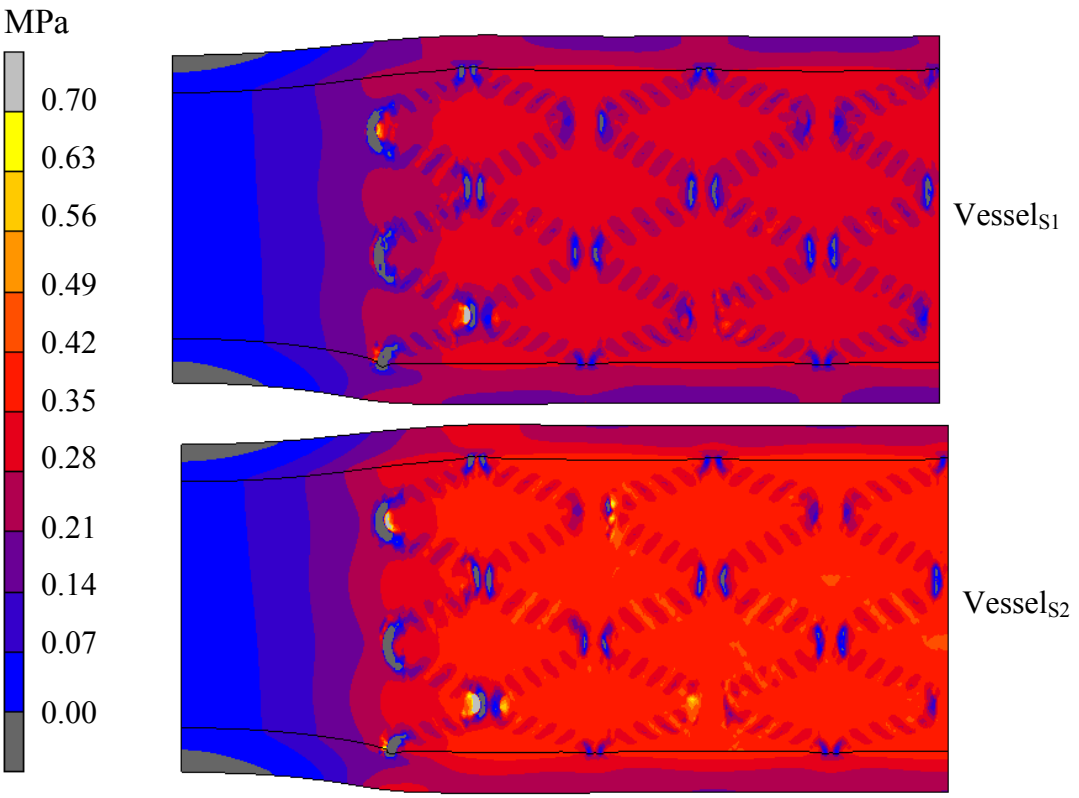

Figure 4.25: Tensile circumferential stresses induced in Vessel$_{S1}$ and Vessel$_{S2}$ stented by Driver$_{fixed}$ using the alternative expansion method, at unloading, achieving final vessel lumen diameters of 3.56 mm and 3.54 mm respectively.

It is clear to see from Figure 4.25 above that the stiffer vessel, Vessel$_{S2}$ results in higher tensile circumferential stresses with some tissue stressed above 0.60 MPa in comparison to Vessel$_{S1}$ which results in maximum tensile stresses of 0.56 MPa. Not only does Vessel$_{S2}$ result in higher stresses but it also contains higher volumes of tissue stressed at these high levels.

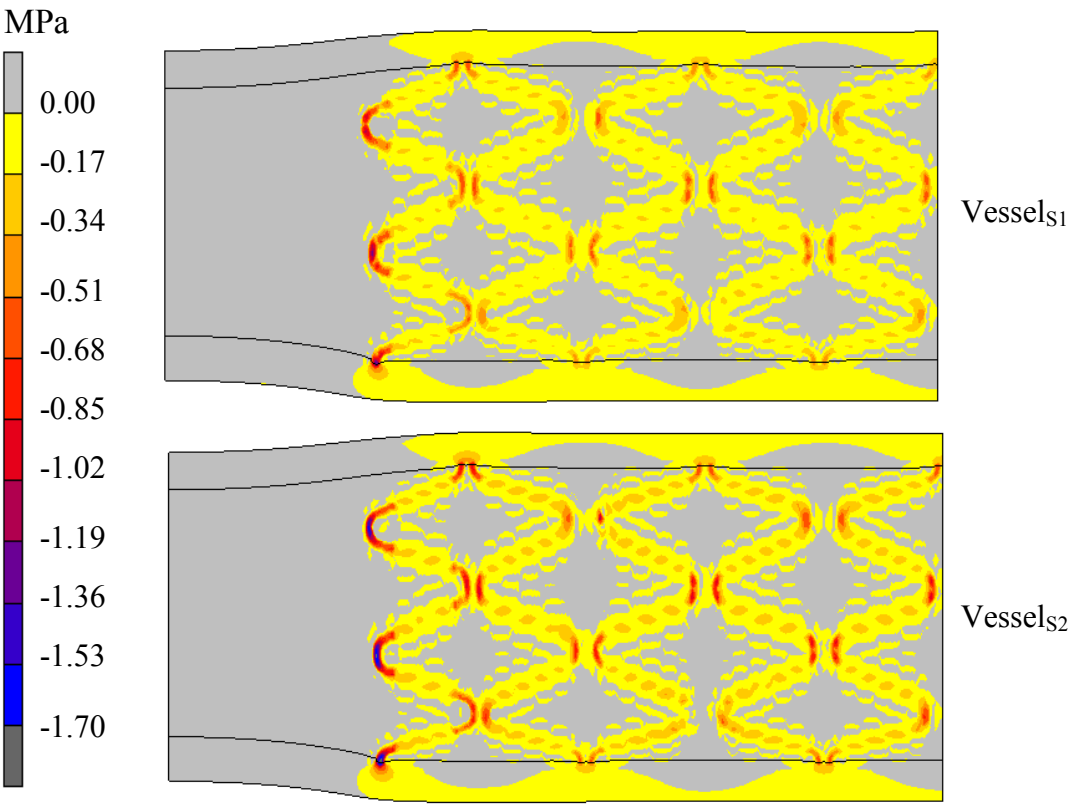

Figure 4.26: Compressive radial stresses induced in Vessel$_{S1}$ and Vessel$_{S2}$ stented by Driver$_{fixed}$ using the alternative expansion method, at unloading, achieving final vessel lumen diameters of 3.56 mm and 3.54 mm respectively.

It is clear to see from Figure 4.26 above that the stiffer vessel, Vessel$_{S2}$ results also in higher compressive radial stresses of -1.70 MPa compared to a maximum of -1.19 MPa experienced by Vessel$_{S1}$. Again, Vessel$_{S2}$ results higher volumes of tissue stressed at these higher levels in comparison to Vessel$_{S1}$. The pockets of stresses seen in between the stent struts are numerical artefacts due to the effect of the adaptive meshing. As some of the elements on the inner surface of the artery subdivide upon contact with the stent an improvement in the resolution of the stress gradients in these areas occurs.

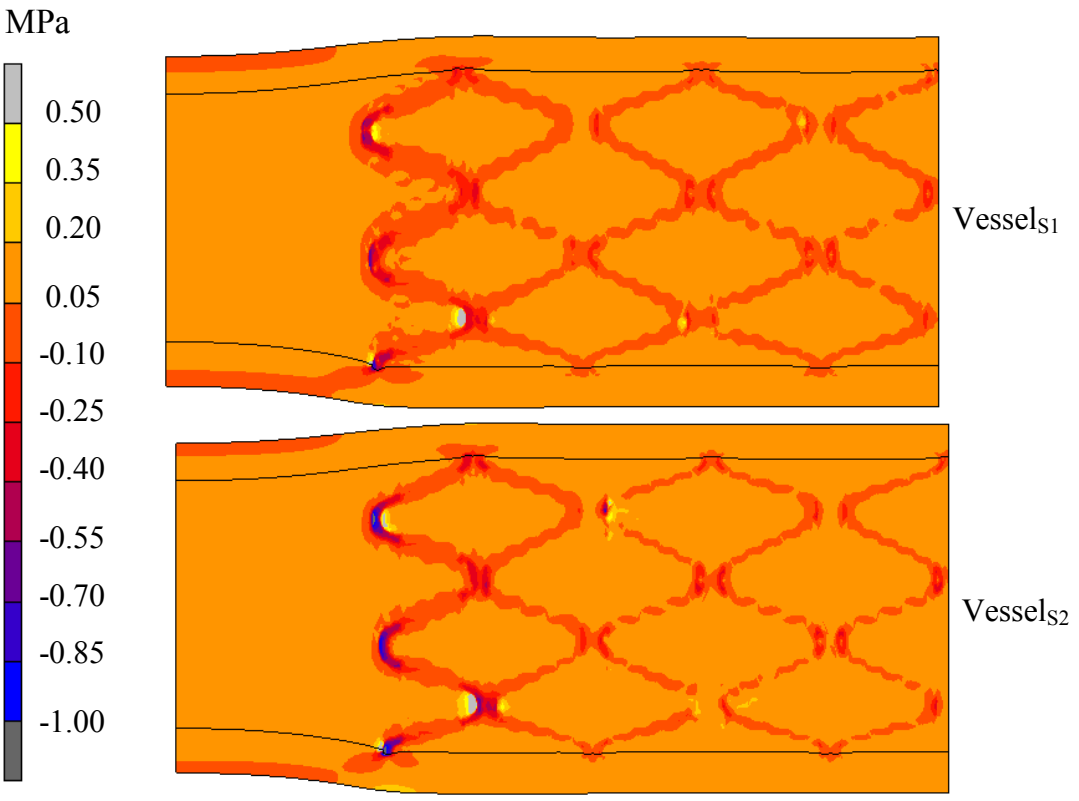

Figure 4.27: Tensile and compressive longitudinal stresses induced in Vessel$_{S1}$ and Vessel$_{S2}$ stented by Driver$_{fixed}$ using the alternative expansion method, at unloading, achieving final vessel lumen diameters of 3.56 mm and 3.54 mm respectively.

The stiffer vessel, Vessel$_{S2}$, also results in higher volumes of tissue containing higher tensile and compressive longitudinal stresses in comparison to Vessel$_{S1}$.

Overall, the stented vessel representing a stiffer coronary artery results in considerably more tissue stressed at high levels in comparison to a less stiff artery. This is important to take into consideration when carrying out numerical analyses where the stresses resulting in the artery from stent expansion are critical. Clearly, the stiffer the artery is, the higher the degree of stresses experienced in all directions.

CHAPTER 5

DISCUSSION

5.1 Introduction

The main objective of this study was to investigate the validity of the numerical methods used to simulate a Driver stent expansion using a compliant mock artery. To achieve this goal, a simple and useful *in-vitro* experimental rig was developed which can now be used to ensure the validity of numerical stent simulations. The medical device industry depends on fast, effective and reliable results to maintain a competitive edge in the stent market today. For this reason two different numerical stent expansion and deployment techniques were investigated. The results of these numerical simulations were compared to an actual stent deployment inside a Sylgard® mock artery such that the most accurate technique could be identified in terms radial recoil, longitudinal recoil, foreshortening and dogboning.

The limitations and assumptions of the numerical methods used will be discussed in this chapter prior to discussing the results obtained. The results obtained from the uniaxial tensile testing and the suitability of Sylgard® material to represent porcine coronary arteries will then be discussed. Finally, the numerical free expansion of the Driver stent together with the two numerical expansion methods inside the mock coronary vessel will be discussed in detail.

5.2 Limitations of this Study

The ability to achieve accurate and reliable results from finite element analyses relies heavily on the inputs, such as geometry and material properties of the components and the boundary conditions applied to represent the realistic situation. The limitations of the numerical and experimental models are as follows:

In this study the numerical stent deployment did not include a balloon which in actuality applies the expansion pressure to the inner surface of the stent. Instead, the pressure was applied as a linearly increasing uniform pressure to the inside of the stent. The inclusion of a folded balloon in a finite element analysis is necessary to accurately model the expansion characteristics of a stent [61]. In the experimental expansion of the Driver stent, the balloon actually caused the ends of the stent to flare out initially, with a further increase in pressure, the middle section of the stent expanded, and with further applied pressure, the stent expanded uniformly. A study carried out by Rogers *et al.* [61] found that small alterations in balloon inflation pressure, balloon material, or stent design can have large effects on the area of balloon-artery contact and therefore the stress applied by the balloon to the arterial wall. They concluded that acute contact of the balloon with the artery wall may have direct impact on vascular injury and explain the greater degree of neointimal thickening seen after stent implantation [40, 41]. This neointimal thickening is a vascular response to stenting which causes intimal cells to proliferate and simultaneously result in the migration of inflammatory cells from the vessel surface to the neointima. This growth response to the arterial injury leads to the thickening of the intima. Although the current study is not investigating the impact of balloon expansion on the vessel stresses, the exclusion of the balloon in this study may impact on the recorded values for stent foreshortening and dogboning. Future work could include a balloon to determine its influence on the expansion characteristics of the stent.

The Sylgard® elastomeric material used to represent the porcine coronary tissue is isotropic in nature whereas coronary arterial tissue is anisotropic. This Sylgard® material was chosen primarily based on its inherent variable elastic properties, and also its transparency which enabled visualisation of the stent throughout deployment. A Mooney-Rivlin isotropic hyperelastic model was used to define the material properties in the numerical simulations. This is an accurate representation of the Sylgard® material and therefore poses no major limitation to the numerical simulation. In addition to this, the material properties for the Sylgard were obtained by carrying out uniaxial tensile tests on flat dogbone-shaped samples. It may have been preferable to carry out these tests using ring-shaped samples.

A further limitation in this study was the modelling of only five of the nine repeating rings to represent the Driver stent in the simulations which involved the stent being expanded inside an artery. This was performed to reduce computational time as the models also included a Sylgard® vessel which consisted of 80,000 elements and 105,191 nodes for the half model alone. Measures for longitudinal recoil and foreshortening, assuming the full length of the stent, i.e. nine links were recorded.

The aforementioned limitations were considered to be acceptable as the primary objective of the current study was to compare the results of a simple stent expansion inside a blood vessel analogue to that of its numerical representation. In doing so, a repeatable *in-vitro* stent expansion rig was developed and an alternative solution to a typical numerical stent expansion was determined. Future numerical and experimental models could include a stenosis in the artery wall and therefore represent a more realistic tortuous coronary artery geometry.

5.3 Suitability of Sylgard® 184 Elastomer

As previously mentioned, the Sylgard® elastomeric material was chosen to represent porcine coronary tissue, primarily due to its variable elastic properties. A 10:1 ratio of the base to curing agent resulted in a stress-strain curve which lay mid-way between the axial and circumferential stress-strain curves for the porcine coronary tissue.

Although this material is isotropic in nature, additional tensile testing of dogbone-shaped samples of the porcine coronary tissue in the circumferential direction revealed the possible isotropic nature of this tissue also. It is common to test ring-shaped samples of arteries in the circumferential direction, whereby the inherent residual stresses are maintained. This stress is defined as the stress that is left in the artery when all external loads are removed. It was thus interesting to see that when these residual stresses were removed, i.e. by cutting open the coronary artery along the length of the artery, the resulting circumferential stress-strain behaviour resembled that of axial stress-strain behaviour. A study carried out by van Andel *et al.* [25] showed no significant difference between the circumferential and longitudinal stiffness of coronary arteries when tested under simulated physiological loading conditions. The influence of residual stresses on the mechanical behaviour of the arterial wall has been reported by Holzapfel *et al.* [62] and Delfino *et al.* [63]. The study carried out by Holzapfel *et al.* [62] incorporated this residual stress, or pre-stretch, by assuming that the natural (unstressed and unconstrained) configuration of the material corresponds to an open sector of an artery. The artery is then closed by an initial bending to form a load-free, but stressed, cylindrical configuration prior to the application of extension or inflation.

Sylgard® was also chosen due to its transparent nature, ensuring the stent was visible as it was being deployed in the mock arteries. In such a way, the appropriate measurements could be acquired at different stages of the stent deployment.

Due to both the variable elastic properties and the transparent nature of this material model, this experimental work has since been successfully used in other research whereby cells have been seeded on the inside of the mock artery wall and analysed in a bioreactor [64].

5.4 Free Expansion of the Driver Stent

5.4.1 Comparison of Numerical Methods for Free Expansion

The analyses found that applying a smaller pressure to a larger surface area along the inner surface of the stent, resulted in a more realistic balloon expansion in terms of expansion pressure. The instructions for use for the Medtronic Driver stent directs the operator to use a pressure of between 9 and 11 atm, which converts to 912 kPa and 1115 kPa, to achieve an internal diameter of 3.5 mm. The numerical free expansion pressure of 1095 kPa, which lies within this range, resulted in an expanded diameter of 3.5 mm. This analysis also demonstrated that the application of 1095 kPa to a larger surface area resulted in a more even radial distribution, which is also representative of a balloon expansion.

As mentioned in Section 3.4 of Chapter 3 Materials & Methods, the Driver stent has a modular design which consists of a number of modular elements which are laser-fused together at two locations on the circumference, positioned 180 degrees apart. A separate analysis of the free expansion of the Driver stent found that constraining all of the weld points in the axial direction rather than at just one location, resulted in a much more realistic and uniform expansion.
The effect of altering the pressure and surface area, and also the constraints in the axial direction did not impact on the von Mises stresses and plastic strains noted in the stent.

5.4.2 Comparison of Numerical & Experimental Free Expansion

When comparing the numerical results to the experimental free expansion, it was found that the numerical model, whereby all weld points were constrained from

moving in the axial direction, represented most accurately the stent expansion behaviour. This behaviour was reported in terms of radial recoil, longitudinal recoil, foreshortening and dogboning. Radial recoil is a common characteristic of metallic stents and is used widely by researchers and stent manufacturers in the verification of a stent design. This adverse effect occurs during the recovery of elastic deformation after balloon deflation and results in lumen loss. Both the experimental and the numerical models achieved similar amounts of radial recoil of 3.73% and 3.91% respectively. Longitudinal recoil is another common characteristic whereby stents can shorten in length upon deflation and removal of the balloon. Again, both the experimental and numerical expansions resulted in similar degrees of longitudinal recoil of -0.29% and -0.34%. The negative value indicates negative recoil whereby the stent actually lengthened upon deployment. Foreshortening, which is the contraction of a stent in the axial direction during deployment, was also seen to match up very closely for the experimental and numerical models, resulting in 3.29% and 3.22% respectively. Dogboning, another characteristic that can be observed during deployment, causes the ends of the stent to flare out. This is also an undesirable effect which can cause damage to the arterial wall upon stent deployment. Although a small amount (0.54%) of dogboning was noted in the experimental free expansion of the Driver stent, no dogboning was observed in any of the numerical analyses of free expansion. This may have been due to the absence of a balloon in the finite element models.

Overall, the numerical model with the axially constrained welds exhibited very similar expansion characteristics to that of the experimental Driver stent expansion, in terms of radial and longitudinal recoil, and foreshortening.
This indicates that the balloon expansion and the associated friction between the balloon and the stent may be represented in numerical models of stent expansion by simply applying the appropriate constraints. This should enable comparison of stent designs in a more computationally efficient manner without the need for the complex balloon unfolding mechanism and contact in the numerical models.

5.5 Expansion of the Driver Stent inside a Sylgard® Mock Artery

5.5.1 Comparison of Numerical Methods for Expansion inside Sylgard® Mock Artery

Two methods of numerical stent expansion inside a Sylgard® vessel were investigated such that an accurate and time-effective method of numerical stent expansion could be determined. The two methods are referred to as (i) the 'original' expansion and (ii) the 'alternative' expansion. As the inclusion of a vessel in the numerical simulation increased the solution time considerably, only 5 repeating links of the Driver stent were represented in these analyses.

As with the free expansion, the effect of constraining the weld points was also investigated in both the 'original' and 'alternative' expansion methods. It is interesting to note that the use of constrained nodes at the weld points had little or no effect on the expansion of the stent when it was expanded inside a vessel as the vessel wall acted as a constraining mechanism itself. However, as the alternative expansion technique consisted of the initial free expansion of the stent, the axially constrained model represents the most realistic in terms of expansion uniformity and foreshortening.

The alternative expansion method enabled the use of a realistic expansion pressure of 1095 kPa, which is within the guidelines of the instructions for use. Expanding the stent as normal, i.e. applying surface pressure to the stent only, requires a much higher pressure of 1600 kPa to expand the Sylgard® mock artery to the same internal diameter of 3.5 mm.

As with the free expansion, the effect of constraining the weld points in the axial direction had little impact on the von Mises stresses and plastic strains for both the original and alternative expansion methods.

5.5.2 Comparison of Numerical & Experimental Expansion inside Sylgard® Mock Artery

When comparing the numerical results to the experimental results, it was interesting to note that the alternative expansion method whereby the welds were axially constrained resulted in the most accurate expansion method in terms of radial recoil, longitudinal recoil, foreshortening, and dogboning.

As with the free expansion, the only major discrepancy between the numerical and experimental results was for dogboning, whereby results of -4.68% and -1.12% were noted. This occurrence of dogboning was observed in both cases at the last repeating ring on the stent. This discrepancy again can be said to be due to the absence of a balloon model in the numerical simulation. However, the numerical results for recoil (both radial and longitudinal) and foreshortening were found to match up very closely with the experimental results.

It is interesting to note that the axially constrained numerical models for the free and alternative expansion methods resulted in the same degree of radial recoil, i.e. 3.91%. This indicates that the unloading of the vessel onto the stent does not impact on the radial recoil characteristic. The results for longitudinal recoil and dogboning on the other hand are significantly different when comparing the numerical free expansion to the numerical expansion inside a Sylgard® vessel. It was noted that the unloading of a vessel onto the stent resulted in the shortening of the stent whereas in free expansion the stent actually lengthened slightly. It was also noted that this unloading of the Sylgard® vessel onto the stent resulted in considerable negative dogboning which was not observed for free expansion.

A further validation of the numerical alternative stent expansion, whereby the welds were constrained, was carried out using strain analysis. It was interesting to note from this analysis that the transverse strains upon unloading of the stent matched up very well for the experimental and numerical models which resulted in strains of 8.71% and 8.57% respectively. This further validates the numerical methods used in this stent deployment. The experimental result however for the axial strain was almost three times greater than that of the numerical model. The

experimental and numerical models resulted in axial strains of 1.23% and 0.43% respectively, which are very low, thus it is difficult to deduce anything from this.

5.6 Achievements of this Study

The main achievement of this study is the development of an *in-vitro* compliant artery model which can be used to investigate the validity of numerical methods used to simulate stent expansion. This *in-vitro* rig has enabled the assessment of the numerical methods used to expand a Driver stent inside a Sylgard® mock artery, whereby the stent characteristics for radial recoil, longitudinal recoil and foreshortening were seen to match up extremely well.

A more time-effective and accurate alternative method of stent deployment has been developed and investigated which has shown promising results in terms of recoil and foreshortening. This expansion technique could be used by stent manufacturers as a quick and simple method for determining the different stent expansion characteristics as the stent design evolves.

CHAPTER 6

CONCLUSIONS

6.1 Main Findings

The main objective of this study was to investigate the validity of the numerical methods used to simulate a Driver stent expansion using a suitable in-vitro experimental model of a compliant mock artery. This study identified a suitable material to be used as a blood vessel substitute such that experimental stent expansions could be carried out within the mock artery and the subsequent results used to evaluate the accuracy of the numerical methods. Finite element analyses were carried out to examine two separate methods for stent expansion such that the most accurate and effective method could be determined. Finally, the effect of increasing the stiffness of the Sylgard® vessel on the stresses induced in the vessel was investigated. The main conclusions of this study are as follows:-

1. Sylgard® 184 elastomeric material can be used as a suitable porcine coronary blood vessel analogue within which stent expansion performance can be evaluated.
2. The numerical free expansion of the Driver stent can be represented accurately in terms of radial recoil, longitudinal recoil, foreshortening and to a certain extent, dogboning without the need for a balloon.
3. The numerical expansion of the Driver stent inside a Sylgard® mock artery can be represented accurately and efficiently in terms of radial recoil, longitudinal recoil, foreshortening and to a certain extent,

dogboning. The alternative expansion method proved to be the most accurate and time-effective method of stent expansion inside a vessel.

4. The transverse strains induced in the vessel wall are accurately represented through the alternative expansion method whereby the vessel is unloaded onto the already expanded stent.
5. A stented vessel representing a stiffer coronary artery results in considerably more tissue stressed at high levels when compared to a lower stiffness vessel.

6.2 Future Work

The main findings of this thesis have proven that numerical stent simulations can be carried out both accurately and efficiently, even without the presence of a balloon. An *in-vitro* compliant artery model has been determined which can be used in future work to evaluate different stent designs. The following recommendations are proposed:

1. The *in-vitro* rig developed as part of this study could be altered and used to create mock vessels of various sizes.
2. Future work should also consider the curing process used for the Sylgard® mock coronary arteries. Recent work has shown a significant increase in the stiffness of the Sylgard® material when cured for 16 hours as compared to just 1 hour as was carried out in this work.
3. Smooth muscle cells could be seeded inside the Sylgard® mock artery and a subsequent stent expansion performed and cell activity in response to the presence of the stent monitored. So far the material has been shown to enable good cell adherence. The effect of stent expansion could thus be analysed at a cellular level.
4. A balloon model could be incorporated into the numerical models to evaluate the influence of the balloon on the four measured stent

parameters: radial recoil, longitudinal recoil, foreshortening, and dogboning.

5. The alternative stent expansion method could be used as a fast and accurate preclinical testing tool to evaluate and determine the optimum stent design.

REFERENCES

[1] Haase, T.T., *et al*., (2008), "Heart disease and stroke statistics--2008 update: a report from the American Heart Association Statistics Committee and Stroke Statistics Subcommittee", Circulation, Vol. 117(4), pp. 25-146.

[2] World Health Organisation, [online], http://www.who.int/cardiovascular_diseases/en/ (Accessed 15th November 2008).

[3] Leal, J., Luengo-Fernandez, R., Gray, A., (2006), "Economic burden of cardiovascular diseases in the enlarged European Union", European Heart Journal, Vol. 27(13), pp. 1610-9.

[4] Irish Heart Foundation, Facts on Heart Disease and Stroke, [online], http://www.irishheart.ie/iopen24/defaultarticle.php?cArticlePath=7_18 (Accessed 15th November 2008).

[5] Tortora, G.J., Grabowski, S.R., "Chap. 20/ The cardiovascular system: The Heart", Principles of Anatomy and Physiology, 10th Edition, pg. 605.

[6] American Heart Association, [online], http://www.americanheart.org/presenter.jhtml?identifier=4478 (Accessed 15th November 2008).

[7] [online] www.mountsinai.org (Accessed 15th November 2008).

[8] WebMD, Heart Disease and Coronary Artery Bypass Surgery, [online], http://www.webmd.com/heart-disease/treating-coronary-artery-bypass (Accessed 15th November 2008).

[9] Cardiovascular Interventions, [online], http://www.orlandocvi.com/procedures_catheter.html (Accessed 15th November 2008).

[10] Dick, A., *et al*., (1999), "Quantification of Horseradish Peroxidase Delivery into the Arterial Wall In Vivo as a Model of Local Drug Treatment: Comparison Between a Porous and a Gel-Coated Balloon Catheter", Cardio Vascular and Interventional Radiology, Vol. 22, pp. 389-393.

[11] Lemos, P.A., Serruys, P.W., Sousa, J.E., (2003), "Drug-Eluting Stents: Cost Versus Clinical Benefit", Circulation, Vol. 107 (24), pp. 3003-3007.

[12] Morice, M.C., Serruys, P.W., Sousa, J.E., et al, (2002), "A randomized comparison of a sirolimus-eluting stent with a standard stent for coronary revascularization", New England Journal of Medicine, Vol. 346, pp. 1773–1780.

[13] Völzke, H., Henzler, J., Menzel, D., Robinson, D.M., Hoffmann, W., Vogelgesang, D., John, U., Motz, W., Rettig, R., (2007), "Outcome after coronary artery bypass graft surgery, coronary angioplasty and stenting", International Journal of Cardiology, Vol. 116, pp. 46-52.

[14] Aurrichio, F., Di Loreto, M., Sacco, E., (2000), "Finite-element Analysis of a Stenotic Artery Revascularization through a Stent Insertion", Computer Methods in Biomechanics and Biomedical Engineering, Vol. 00, pp. 1-15.

[15] Fung, Y. C., Biomechanics, (Second Edition), Springer, pg. 251.

[16] Raghavan, M.L., Lecture Notes: Cardiovascular Biomechanics Section. University of Iowa Dept. of Biomedical Engineering. [online], http://www.engineering.uiowa.edu/~bme050/cvb-solids.pdf (Accessed 20th September 2006).

[17] Anatomy Review: Blood Vessel Structure and Function. Benjamin Cummings Publishing Co. [online], http://education.adam.com/products/ipie/iguide/Anatomy_Rev_Blood_Vessel.pdf (Accessed 20th September 2006).

[18] Cardiovascular Pulsation, [online], http://herkules.oulu.fi/isbn951426973X/html/x840.html (Accessed 15th November 2008).

[19] Dunn, A.C. et al., (2007), "Macroscopic friction coefficient measurements on living endothelial cells", Tribology Letters, Vol. 27 (2), pp. 233-238.

[20] Rogers, C., Tseng, D.Y., Squire, J.C., Edelman, E.R., (1999), "Balloon-Artery Interactions During Stent Placement: A Finite Element Analysis Approach to Pressure, Compliance, and Stent Design as Contributors to Vascular Injury", Circulation, Vol. 84, pp. 378-383.

[21] Humphrey, J.D., (2002), "Mechanical properties of soft tissues and arterial walls, Biomechanics of soft tissue in cardiovascular systems", Wien, Springer.

[22] Hayashi *et al.,*(1981), "Mechanical properties of aortas and pulmonary arteries of calves implanted with cardiac prostheses", Journal of Biomechanics, Vol. 14, pp. 173-182.

[23] Dobrin *et al*., (1969), "Influence of vascular smooth muscle on contractile mechanics and elasticity of arteries", American Journal of Physiology, Vol. 217 (6), pp. 1644-1651.

[24] Saikrishna, C., Talwar, S., Gulati, G., Kumar, S.A., (2006), "Normal coronary artery dimensions in Indians", Cardiothoracic Sciences Centre, All India Institute of Medical Sciences, New Delhi.

[25] van Andel, C.J., Pistecky, P.V. and Borst, C., (2003), "Mechanical properties of porcine and human arteries: implications for coronary anastomotic connectors, Annals of Thoracic Surgery, Vol. 76, pp. 58-65.

[26] Burton AC., (1962), "Physical principles of circulatory phenomena: the physical equilibria of the heart and blood vessels". In: Handbook of Physiology, Section 2, Circulation 1, American Physiological Society, Washington, D.C., 94.

[27] Dobrin *et al*., (1978), "Mechanical properties of arteries", Physiological Reviews , Vol. 58, pp. 397-460.

[28] Manak J.J., (1980), "The two-dimensional *in vitro* passive stress-strain elasticity relationships for the steer thoracic aorta blood vessel tissue", Journal of Biomechanics, Vol. 13. pp. 637-646.

[29] Carew T.E., Vaishnav R.N., Patel, D.J., (1968), "Compressibility of the arterial wall", Circulation, Vol. 23 (1), pp. 61-68.

[30] Dow Corning. Sylgard® 184 Silicone Elastomer Product Information.

[31] Peattie, R.A., Riehle, T.J., Bluth, E.I., (2004), "Pulsatile Flow in Fusiform Models of Abdominal Aortic Aneurysms: Flow Fields, Velocity Patterns and Flow-Induced Wall Stresses", Journal of Biomechanical Engineering, Vol. 126, pp. 438-446.

[32] Yip, R., Mongrain, R., Ranga, A., Brunette, J., Cartier, R., "Development of anatomically correct mock-ups of the aorta for PIV investigations". Department of Mechanical Engineering, McGill University. Montreal Heart Institute. [online] http://deseng.ryerson.ca/CDEN2004/data/10126.pdf (Accessed 20th November 2008).

[33] Olbrich, T., and Murray, A., (2004), "Assessment of a technique to determine the mechanical properties of coronary arteries using mock arteries", Journal of Physiological Measurement, Vol. 25, pp. 997-1011.

[34] Salzar, R.S., Thubrikar, M.J., Eppink, R.T., (1995), "Pressure-induced mechanical stress in the carotid artery bifurcation: a possible correlation to atherosclerosis", Journal of Biomechanics, Vol. 28 (11), pp. 1333-1340.

[35] Prendergast, P., Lally, C., Daly, S., Reid, A.J., Lee, T.C., Quinn, D., Dolan, F., (2003), " Analysis of prolapsed in cardiovascular stents: A constitutive equation for vascular tissue and finite-element modelling", Journal of Biomechanical Engineering, Vol. 125 (5), pp. 692-699.

[36] Menzel, A., (2005), "Modelling of anisotropic growth in biological tissues: a new approach and computational aspects", Biomechanical Model Mechanobiology, Vol. 3, pp. 147-171.

[37] Vito, R.P. and Dixon, S.A., (2003), "Blood vessel constitutive models – 1995-2002", Annual Review of Biomedical Engineering, Vol. 5, pp. 413-439.

[38] Fung, Y.C., (1993), "Biomechanics: Mechanical Properties of Living Tissues", Springer, New York.

[39] Lally, C., Dolan, F., Prendergast, P.J., (2005), "Cardiovascular stent design and vessel stresses: a finite element analysis", Journal of Biomechanics, Vol. 38, pp. 1574-1581.

[40] Fischman, D.L., Leon, M.B., Baim, D.S. *et al.* (1994), "A randomized comparison of coronary stent placement and balloon angioplasty in the treatment of coronary artery disease". New England Journal of Medicine, Vol. 331, pp. 496-501.

[41] Surruys, P.W., de Jaegere, P., Kiemeneij *et al*. (1994), "A comparison of balloon expandable stent implantation with balloon angioplasty in patients with coronary artery disease: the BENESTENT study group". New England Journal of Medicine, Vol. 331, pp. 489-495.

[42] Pratsos, A., Fischman, D.L. and Savage, M.P., (2001), "Restenosis in SaphenousVein Grafts", Current Interventional Cardiology Reports, Vol. 3, pp. 287-295.

[43] Sousa, J.E., Costa, M.A., Sousa, A.G., (2003), "Two year angiographic and intravascular ultrasound follow-up after implantation of sirolimus-eluting stents in human coronary arteries". Circulation, Vol. 3, pp. 381-383.

[44] Laroche, D., Delorme, S., Anderson, T., DiRaddo, R., (2006), "Computer Prediction of Friction in Balloon Angioplasty and Stent Implantation", International Symposium on Biomedical Simulation (ISBMS), LNCS 4072, pp. 1-8.

[45] Migliavacca, F., Petrini, L., Montanari, V., Quagliana, I., Auricchio, F., Dubini, G., (2005), "A predictive study of the mechanical behaviour of coronary stents by computer modelling", Medical Engineering & Physics, Vol. 27, pp. 13-18.

[46] Walke, W., Paszenda, Z., Filipiak, J., (2005), "Experimental and numerical biomechanical analysis of vascular stent", Journal of Materials Processing Technology, Vol. 164-165, pp. 1263-1268.

[47] Etave, F., Finet, G., Boivin, M., Boyer, J-C., Rioufol, G., Thollet, G., (2001), "Mechanical properties of coronary stents determined by using finite element analysis", Journal of Biomechanics, Vol. 34, pp. 1065-1075.

[48] Liang, D.K., Yang, D.Z., Qi, M., Wang, W.Q., (2005), "Finite element analysis of the implantation of a balloon-expandable stent in a stenosed artery", International Journal of Cardiology, Vol. 104, pp. 314-318.

[49] Holzapfel, G.A., Stadler, M. and Gasser, T.C., (2005), "Changes in the mechanical environment of stenotic arteries during interaction with stents: computational assessment of parametric stent designs", AMSE, Vol. 127, pp. 166-180.

[50] Whitcher, F.D., (1997), "Simulation of in vivo loading conditions of nitinol vascular stent structures", Computers & Structures, Vol. 64, pp. 1005-1011.

[51] Thériault, P., Terriault, P., Brailovski, V., Gallo, R., "Finite element modelling of a progressively expanding shape memory stent", Journal of Biomechanics, Vol. 39, pp. 2837-2844.

[52] Wu, W., Qi, M., Liu, X-P., Yang, D-Z., Wang, W-Q., (2007), "Delivery and release of nitinol stent in carotid artery and their interactions: A finite element analysis", Journal of Biomechanics, doi:10.1016/j.jbiomech.2007.02.024 (article in press).

[53] Dumoulin, C., Cochelin, B., (2000), "Mechanical behavior modelling of balloon-expandable stents", Journal of Biomechanics, Vol. 33, pp. 1461-1470.

[54] Chua, S. N. D, Mac Donald, B. J. and Hashmi, M. S. J., (2002), "Finite element simulation of stent expansion", Journal of Materials Processing Technology, Vol. 120, pp. 335-340.

[55] Chua, S. N. D., MacDonald, B.J. and Hashmi, M.S.J., (2003), "Finite element simulation of stent and balloon interaction", Journal of Materials Processing Technology, Vol. 143-144, pp. 591-597.

[56] Chua, S. N. D., MacDonald, B.J. and Hashmi, M.S.J., (2004), "Finite element simulation of slotted tube (stent) with the presence of plaque and artery by balloon expansion", Journal of Materials Processing Technology, pp. 1772-1779.

[57] Migliavacca, F., Petrini, L., Auricchio, F., Dubini, G., (2003), "Deployment of an intravascular stent in coronary stenotic arteries: a computational study", abstract from the 2003 Summer Bioengineering Conference, June 25-29, Florida.

[58] Barragan, P., Rieu, R., Garitey, V., Roquebert, P.O., Sainsous, J., Silvestri, M., Bayet, G., (2000), "Elastic Recoil of Coronary Stents", Catheterisation and Cardiovascular Interventions, Vol. 50, pp. 112-119.

[59] Swindle, M., (1992), "Swine as Models in Biomedical Research", Iowa State University Press, Ames, Iowa, 165.

[60] Galloza, A., Torres, J.J., Torres, J., Vargas, V.M., Vega, O.., (2004), Biomechanics of implants and dental materials, Review article prepared for course on Mechanics of Materials – 1. Course Instructor: Dr Megh R. Goyal, Profesor in Biomedical Engineering, General Engineering Department, PO Box 5984,Mayaguez, Puerto Rico.

[61] De Beule, M., Mortier, P., Carlier, S.G., Verhegghe, B., Van Impe, R., Verdonck, P., (2008), "Realistic finite element-based stent design: The impact of balloon folding", Journal of Biomechanics, Vol. 41, pp. 383-389.

[62] Holzapfel, G.A., Gasser, T.C., Ogden, R.W., (2000), "A new constitutive framework for arterial wall mechanics and a comparative study of material models", Journal of Elasticity, Vol. 61, pp. 1-48.

[63] Delfino, A., Stergiopulos, N., Moore, J.E., Meister, J.J., (1997), "Residual strain effects on the stress field in a thick wall finite element model of the human carotid bifurcation", Journal of Biomechanics, Vol. 30, pp. 777-786.

[64] Colombo, A., Cahill, P.A., Lally, C., (2008), "The amplitude rather than mean strain determines the proliferative and apoptotic capacity of vascular smooth muscle cells in *vitro*", to be presented at the Vascular & Smooth Muscle Physiology Themed Meeting at King's College, London, 15th-17th December 2008.

Appendix A

Mesh Convergence for Stent Model

Three mesh densities were analysed for the Driver stent and the maximum von Mises stress was determined in each case. It was found from the mesh density study that 21 elements through the thickness of the stent was the most suitable. A mere 3% difference was found between mesh type 2 and mesh type 3 even though the mesh density had more than doubled

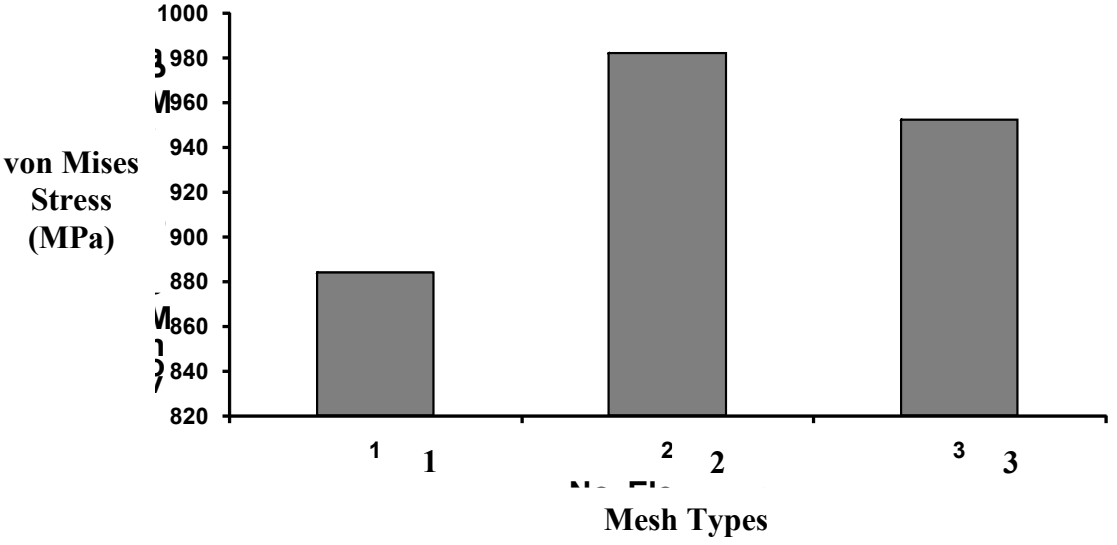

Mesh Type 1: 12 elements through stent thickness.

Mesh Type 2: 21 elements through stent thickness.

Mesh Type 3: 48 elements through stent thickness.